UNIVERSITY OF CALIFORNIA, SAN DIEGO

Application of Broadband Marine Magnetotelluric Exploration to a 3D Salt Structure and a Fast-Spreading Ridge

A dissertation submitted in partial satisfaction of the
requirements for the degree Doctor of Philosophy
in Earth Sciences

by

Kerry W. Key

Committee in charge:

Steven Constable, Chairperson
Charles Cox
Yuri Fialko
Graham Kent
Larry Milstein

2003

The dissertation of Kerry W. Key is approved, and it is acceptable in quality and form for publication on microfilm:

Chair

University of California, San Diego

2003

For my parents Clare and Bill, and my brother Kevin

Table of Contents

List of Figures

List of Tables

Acknowledgements

I wish to thank my advisor, Steven Constable, who invited me to participate (i.e. provide free labor) in the 1997 Gemini Prospect MT cruise when I was a mere undergraduate student. At that time I was still bobbing around freely in an ocean of undecided possibilities for a future career; Steve's subsequent encouragement to join the SIO graduate program and his gusto for geophysical research have since guided me along a rewarding path. Steve and Cathy Constable are thanked for the many parties at the "Constabulary," which promoted familiarity between faculty, old students, and new students and made IGPP a friendly place to be. I wish to also thank the other members of my committee: Chip Cox, Yuri Fialko, Graham Kent, and Larry Milstein. Their comments and interest in my work have added greatly to this dissertation.

My wife Carolyn and stepson Alexander have made the past three years a joy. Their love fuels my every day. My parents are thanked for their dedication to my education. Their unending support, encouragement, and wisdom have been invaluable. I thank my older brother Kevin for showing me early on that its okay to take your toys apart, and that computers and electronics are wonders to be explored.

I thank my friends and colleagues at Scripps Institution of Oceanography, in particular James Behrens and Adrian Borsa for many fun adventures. Chester Weiss of Sandia National Laboratories spent the fall of 2002 at IGPP and is thanked for his friendship and collaboration.

Arnold Orange and AOA Geophysics are thanked for their ongoing collaboration with the SIO Marine EM Laboratory, in particular for providing personnel for the seagoing experiments presented in this dissertation. Lisl Lewis of AOA Geophysics is a friend and colleague; her dedication and attention to detail has been pivotal to the success of many of our research cruises.

Funding for the research presented in this dissertation was provided in

part or in full from the Seafloor Electromagnetic Methods Consortium at Scripps Institution of Oceanography. Current and past members include: Anadarko, Shell, Texaco, Chevron, AGIP, BP, BHP, British Gas, ExxonMobil, GERD, AOA Geophysics, Norsk-Hydro, Statoil, OHM, and ISL.

The text of Chapter 3, in part or in full, is a reprint of the material as has been submitted for publication. The dissertation author was the primary researcher and author of the published work. The co-author listed in the publication directed and supervised the research which forms the basis for Chapter 3.

The text of Chapter 4, in part or in full, is a reprint of the material as it appears in *Geophysical Research Letters*. The dissertation author was the primary researcher and author of the published work. The co-authors listed in the publication directed and supervised the research which forms the basis for Chapter 4.

Vita

November 24, 1974	Born, Arlington Heights, Illinois
1998	B.Sc. University of California, San Diego
1998–2003	Research Assistant, University of California, San Diego
1998-1999	Teaching Assistant, Department of Earth Sciences University of California, San Diego
2003	Doctor of Philosophy University of California, San Diego

Publications

Heinson, G., A. White, S. Constable and K. Key, Marine self potential exploration, *Expl. Geophys., 30*, 1-4, 1999.

Evans, R. L., S. C. Webb, W. Crawford, C. Golden, K. Key, L. Lewis, H. Miyano, E. Roosen and D. Doherty, Crustal resistivity structure at 9°50′N on the East Pacific Rise; results of an electromagnetic survey, *Geophys. Res. Letts., 29*, 6-1 to 6-4, 2002.

Key, K. and S. Constable, Broadband marine MT exploration of the East Pacific Rise at 9°50′N, *Geophys. Res. Letts., 29*, 2054, doi: 10.1029/2002GL016035, 2002.

Abstracts

Key, K., S. Constable, B. Ildefonse, L. MacGregor, B. Valsardieu and P. Pezard, Electrical studies of the Oman Ophiolite, *Eos Trans. AGU, 80*(46), 1999.

Key, K. W., and S. C. Constable, Conductivity structure of a mid-ocean ridge: MT Results from the East Pacific Rise, *15th Workshop on Electromagnetic Induction in the Earth, Cabo Frio, Brazil*, 2000.

Key, K. W., S. C. Constable, Electrical conductivity structure of a mid-ocean Ridge: MT results from the EPR at 9°50′N, *Eos Trans. AGU, 81*(48), 2000.

Mikada, H., S. Constable, K. Key, M. Uyeshima, K. Sayanagi and G. Fujie, Marine magnetotellurics for the petrophysical identification of the seismogenic zone, off Sanriku, Japan, *Eos Trans. AGU, 81*(48), 2000.

Key, K., S. Constable and A. Orange, New results using the marine magnetotelluric method over a 3-D structure, *Eos Trans. AGU, 82*(47), 2001.

Key, K., S. Constable and C. Weiss, New results using marine MT over a 3D structure, *16th Workshop on Electromagnetic Induction in the Earth, Santa Fe, New Mexico*, 2002.

Key, K. and S. Constable, Measuring the electrical resistivity of the crust at the East Pacific Rise 9°50′N, *16th Workshop on Electromagnetic Induction in the Earth, Santa Fe, New Mexico*, 2002.

Key, K., G. Heinson, S. Constable and A. White, Preliminary marine MT results from the Anisotropy and Physics of the Pacific Lithosphere Experiment (APPLE), *16th Workshop on Electromagnetic Induction in the Earth, Santa Fe, New Mexico*, 2002.

Lewis, L., S. Constable, A. Orange and K. Key, Marine magnetotelluric mapping of sub-volcanic structure in the Faroe-Shetland basin,*16th Workshop on Electromagnetic Induction in the Earth, Santa Fe, New Mexico*, 2002.

Key, K. and S. Constable, Broadband marine MT exploration of the East Pacific Rise at 9°50′N, *Eos Trans. AGU, 83*(47), 2002.

Heinson, G., K. Key, S. Constable and A. White, Preliminary marine MT results from the Anisotropy and Physics of the Pacific Lithosphere Experiment (APPLE), *Eos Trans. AGU, 83*(47), 2002.

Weiss, C., K. Key and S. Constable, Salt, sediments and seawater: Marine magnetotellurics in the Gulf of Mexico, *Eos Trans. AGU, 83*(47), 2002.

Key, K., S. Constable and C. Weiss, Mapping 3D salt with 2D marine MT: Case study from Gemini Prospect, Gulf of Mexico, *3DEM-III Workshop, Adeliade, Australia*, 2003.

Abstract of the Dissertation

Application of Broadband Marine Magnetotelluric Exploration
to a 3D Salt Structure and a Fast-Spreading Ridge

by

Kerry W. Key
Doctor of Philosophy in Earth Sciences
University of California, San Diego, 2003
Professor Steven Constable, Chair

The recent development of broadband marine magnetotelluric (MT) instrumentation enables resolution of seafloor electrical conductivity structure at shallower depths than was previously available. This dissertation focuses on the application of broadband marine MT to imaging the conductivity structure of a salt intrusion on the continental shelf in the Gulf of Mexico (GOM) and also the magmatic system at the fast-spreading ridge at the East Pacific Rise (EPR).

Gemini Prospect has served as a test bed for the Scripps Institution of Oceanography broadband marine MT instrument. Over 42 sites of MT data have been collected in the period band of 1-3000 s in a two-dimensional (2D) grid over the Gemini salt structure, providing an excellent data set for developing and testing inversion techniques. Top and base-of-salt surfaces provided from a commercial 3D seismic survey allow for verification of the MT results. 2D inversions of the Gemini MT data can recover the salt body remarkably well despite its complex 3D shape, but the results are heavily dependent on which mode of data is inverted. The best agreement is found when inverting the mode with the electric field perpendicular to the dominant structural strike. An improved geological interpretation is found through the joint presentation of both seismic reflection profiles and electrical resistivity models. A thin and shallow resistive feature observed outside the seismic

salt volume may indicate a change in porosity or pore fluids associated with a natural trap in the sediments. An overhanging resistive feature correlates with a previously uninterpreted strong reflection and illustrates how MT can constrain structure in regions where the seismic method performs poorly.

At the EPR near 9°50′N, a pilot survey using the broadband instruments shows sensitivity to structure at shallower depths than previous ridge MT experiments. Two-dimensional inversion of data from 4 sites images a high conductivity zone located in the crust and shallow mantle that is associated with the ridge magmatic system and that agrees well with seismic tomography and seafloor compliance results. Resistivities beneath the ridge imply a crustal partial melt fraction of 1-20% and a total melt volume of about 0.75 km^3 per axial kilometer of ridge.

Chapter 1

Introduction

Electrical conductivity is one of the most widely varying physical properties of Earth. While the seismic velocity and density of rocks that comprise Earth's crust typically vary at most by about one order of magnitude and more typically by a factor of 2, the electrical conductivity (and its reciprocal resistivity) typically varies by many orders of magnitude. The large contrasts that result make electrical conductivity an attractive tool for geophysicists interested in exploring the structure and physical state of Earth's interior. The electrical conductivity of any rock depends on the its composition, temperature, porosity, permeability and pore fluid content, and so knowledge of the electrical conductivity distribution of subsurface structures can provide information on a wide range of other physical and geological properties.

One well established technique for imaging electrical conductivity structure is the magnetotelluric (MT) method. This technique utilizes the natural time variations of Earth's magnetic field in the period range of about 0.001 to 100,000 s as a source of excitation energy. The time variations of the magnetic field induce a corresponding electric field within Earth that is proportional to the conductivity structure. The physics of the method involves the diffusion equation and so the resolution is less than for methods based on the wave equation (seismology, ground penetrating radar), however, the wide period range that can be utilized makes the method sensitive to structures at crustal depths of a few meters to mantle depths

of 100's of kilometers. The development of the magnetotelluric (MT) method has taken considerable leaps in the 50 years since its was first proposed [*Tikhonov*, 1950; *Cagniard*, 1953]. Advancements in instrumentation, data processing and modeling have resulted in many significant land based problems being solved using the magnetotelluric method. While academics have been using the MT method on the seafloor to study the structure of the Earth for a few decades now, recent improvements in instrumentation, particularly the introduction of broadband sensors, have resulted in a surge of renewed interest in both academia and industry in using electromagnetic methods in the marine environment.

In Chapter 2 of this dissertation I review the basic physics of magnetotelluric exploration with an emphasis on using the method on the seafloor, and I also present some technical aspects of instrumentation and data processing used for marine MT.

In the context of petroleum exploration, the marine MT method is useful for characterizing the conductivity structure of salt intrusions and sediments found on the continental shelves and can be used in conjunction with the controlled-source electromagnetic (CSEM) method, which is effective at detecting thin resistive petroleum reservoirs. For joint marine MT/CSEM experiments, marine MT can be used to characterize and constrain the overall background conductivity structure, which is useful for CSEM numerical modeling and interpretation. In Chapter 3 of this dissertation I present a case study of using 2D marine MT to image a 3D salt structure at a petroleum prospect in the northern Gulf of Mexico.

In Chapter 4 I present the results of a pilot MT experiment at the fast-spreading East Pacific Rise near 9°50′N which show that marine MT can detect crustal regions of partial melt and help constrain the extent of the ridge hydrothermal system. Academic interest in marine MT has been renewed by this pilot experiment, and NSF funding has been obtained to conduct a full 60 site MT and CSEM experiment at the EPR 9°50′N in the spring of 2004.

References

Cagniard, L., Basic theory of the magneto-telluric method of geophysical prospecting, *Geophysics*, *18*, 605–635, 1953.

Tikhonov, A. N., On determining electrical characteristics of the deep layers of the earth's crust, *Dokl. Acad. Nauk SSSR.*, *73*, 275–297, 1950.

Chapter 2

Magnetotelluric Exploration on the Seafloor

In this chapter a review of magnetotelluric exploration on the seafloor is presented. The first two sections present the basic physics and theoretical aspects of using MT on the seafloor. The last three sections review the instrumentation and methodology developed and adapted at Scripps Institution of Oceanography to carry out marine MT surveys and process marine MT data. A general review of the MT method as used on land is given by *Vozoff* [1991].

2.1 The Magnetotelluric Method: Basic Physics

At the frequencies used in marine MT (about 0.0001-10 Hz), the source field arises in Earth's magnetosphere where the complex interaction of the solar wind and the geomagnetic field generates hydromagnetic (plasma) waves [*Vozoff*, 1991]. Below about 100 km the atmosphere is an electrical insulator, and so the fields generated above this level form plane electromagnetic (EM) waves that propagate vertically downward. At Earth's surface most of the plane-wave electromagnetic energy is reflected back into the atmosphere and a small amount penetrates vertically into the ground. This source field induces electrical (telluric) currents within Earth, which in turn can create secondary magnetic fields where electrical

conductivity contrasts occur. As will be shown below, the relative strength of the induced and secondary fields depends on the subsurface electrical conductivity structure. Thus, the relative strengths of the electric and magnetic fields measured on the surface of Earth contain information on the electrical conductivity structure beneath measurement sites.

2.1.1 Behavior of Electric and Magnetic Fields

Following the approach of *Ward and Hohmann* [1988], the governing equations of the MT method can be derived by starting from Maxwell's equations

$$\nabla \times \mathbf{E} = -\frac{\partial \mathbf{B}}{\partial t} \tag{2.1}$$

$$\nabla \times \mathbf{H} = \mathbf{J} + \frac{\partial \mathbf{D}}{\partial t}, \tag{2.2}$$

where

$$\begin{aligned}
\mathbf{E} &= \text{electric field intensity (V m}^{-1}\text{)} \\
\mathbf{J} &= \text{electric current density (A m}^{-2}\text{)} \\
\mathbf{H} &= \text{magnetic field intensity (A m}^{-1}\text{)} \\
\mathbf{B} &= \text{magnetic flux density (T)} \\
\mathbf{D} &= \text{electric displacement (C m}^{-2}\text{).}
\end{aligned}$$

In a homogeneous isotropic medium the following scalar constitutive relations apply

$$\begin{aligned}
\mathbf{D} &= \epsilon \mathbf{E} \\
\mathbf{B} &= \mu \mathbf{H} \\
\mathbf{J} &= \sigma \mathbf{E},
\end{aligned}$$

where ϵ is the electrical permittivity (F m^{-1}), μ is the magnetic permeability (H m^{-1}) and σ is the electrical conductivity (S m^{-1}). When substituted into Maxwell's equations, the constitutive relations account for the electromagnetic properties of matter (i.e. permittivity, permeability and conductivity). Taking the curl of equation 2.1 and substituting in the constitutive relation for the magnetic

flux density $\mathbf{B}$ yields

$$\nabla \times (\nabla \times \mathbf{E}) = -\mu \left(\nabla \times \frac{\partial \mathbf{H}}{\partial t} \right).$$

Using the vector identity $\nabla \times (\nabla \times \mathbf{A}) = \nabla (\nabla \cdot \mathbf{A}) - \nabla^2 \mathbf{A}$, noting the equation for the divergence of the electric field in a charge free region ($\nabla \cdot \mathbf{E} = 0$), and substituting for $\mathbf{J}$ and $\mathbf{D}$ yields the wave equation

$$\nabla^2 \mathbf{E} = \mu \left(\sigma \frac{\partial \mathbf{E}}{\partial t} + \epsilon \frac{\partial^2 \mathbf{E}}{\partial t^2} \right). \tag{2.3}$$

If ω is the angular frequency and $e^{i\omega t}$ is the time dependence for $\mathbf{E}$, Fourier transformation of (2.3) yields the Helmholtz equation

$$\left(\nabla^2 + k^2 \right) \mathbf{E} = 0, \tag{2.4}$$

where k is the propagation constant or complex wave number in the medium

$$k^2 = \mu\omega(\epsilon\omega - i\sigma).$$

The relatively low frequencies used for MT and Earth material conductivities result in $\sigma \gg \epsilon\omega$ (known as the quasi-static assumption) making

$$k \simeq (-i\sigma\mu\omega)^{\frac{1}{2}} = \left(\frac{\sigma\mu\omega}{2} \right)^{\frac{1}{2}} - i \left(\frac{\sigma\mu\omega}{2} \right)^{\frac{1}{2}} = (\sigma\mu\omega)^{\frac{1}{2}} e^{-i\frac{\pi}{4}}.$$

The low f assumption means the second term on the right in the wave equation (2.3) can be neglected, yielding a diffusion equation

$$\nabla^2 \mathbf{E} = \mu\sigma \frac{\partial \mathbf{E}}{\partial t}. \tag{2.5}$$

Following the same method as above, but for the magnetic field intensity yields a similar equation

$$\nabla^2 \mathbf{H} = \mu\sigma \frac{\partial \mathbf{H}}{\partial t}. \tag{2.6}$$

The diffusion equation describes the behavior of electric and magnetic fields in Earth at the frequencies used in MT. This points out an important point about the MT method. The inherent resolution of MT is dependent on the behavior of

the diffusion equation and lies between that of exploration methods governed by wave equations (seismic method, ground penetrating radar) and methods described with Laplace's equation (potential field methods using gravity, magnetics, and DC resistivity). In practice the resolving power of any of the above methods is heavily dependent on the physical properties of the structures surveyed, the wavelengths or frequencies of the measured field, and the depth attenuation of the measured field.

In a half-space the frequency domain equivalents of equations 2.5 and 2.6 are

$$\frac{\partial^2 \mathbf{E}}{\partial z^2} + k^2 \mathbf{E} = 0 \tag{2.7}$$

and

$$\frac{\partial^2 \mathbf{H}}{\partial z^2} + k^2 \mathbf{H} = 0, \tag{2.8}$$

with solutions

$$\mathbf{E} = \mathbf{E}_0 e^{-ikz} = \mathbf{E}_0 e^{-i\alpha z} e^{-\beta z} \tag{2.9}$$

and

$$\mathbf{H} = \mathbf{H}_0 e^{-ikz} = \mathbf{H}_0 e^{-i\alpha z} e^{-\beta z}, \tag{2.10}$$

where

$$\alpha = \beta = \sqrt{\frac{\sigma \mu \omega}{2}}, \tag{2.11}$$

and $\mathbf{E}_0$ and $\mathbf{H}_0$ are the values of the field at $z = 0$. Equations 2.9 and 2.10 show that the fields varying sinusoidally with depth due to the $e^{-i\alpha z}$ term and experience a depth dependent attenuation from the $e^{-\beta z}$ term. The distance at which the field amplitude is reduced in amplitude by a factor of $1/e$ or to about 37% is known as the skin depth δ

$$\delta = \frac{1}{\beta} = \sqrt{\frac{2}{\sigma \mu \omega}} \approx 500\sqrt{\rho\, T} \text{ meters}, \tag{2.12}$$

where $\rho = 1/\sigma$ is the resistivity (Ωm) and $T = 1/f$ is the period (s). Figure 2.1 shows the skin depth versus period for various half-space resistivities. Higher conductivity (lower resistivity) materials attenuate EM fields more rapidly and have smaller skin depths than lower conductivity materials. Similarly short period

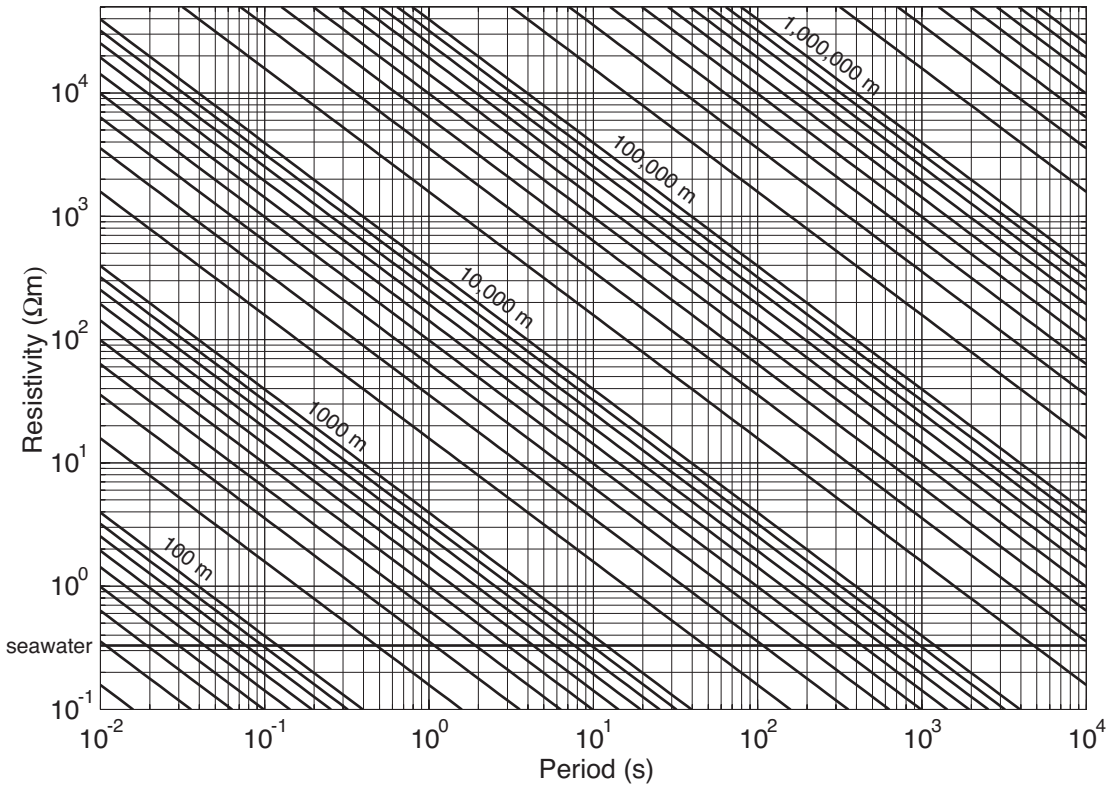

Figure 2.1: Skin depth versus period for different half-space resistivities.

(high frequency) electric and magnetic fields have smaller skin depths than longer periods. For the case of marine MT measurements on the seafloor, the overlying sea water has low resistivity (about 0.3 Ωm) and a small skin depth (e.g. 270 m at 1 Hz). At short periods in an ocean more than several skin depths deep the incident MT source field is almost completely attenuated at the seafloor depth. Thus, the shortest period MT fields observed on the seafloor are heavily dependent on the ocean depth.

2.1.2 Relationship Between Electric and Magnetic Fields

Faraday's law (Equation 2.1) in the frequency domain implies the following relationships between the **E** and **H**

$$\frac{\partial E_z}{\partial y} - \frac{\partial E_y}{\partial z} = -i\mu\omega H_x \tag{2.13}$$

$$\frac{\partial E_x}{\partial z} - \frac{\partial E_z}{\partial x} = -i\mu\omega H_y \tag{2.14}$$

$$\frac{\partial E_y}{\partial x} - \frac{\partial E_x}{\partial y} = -i\mu\omega H_z. \tag{2.15}$$

For a uniform plane wave **H** propagating in the z direction in a half-space the E_z term and its derivative are zero, as are as the x and y derivatives of E_y and E_x (since there is no H_z component). Substituting equations 2.9 and 2.10 equations 2.13 and 2.14 reduce to

$$\frac{E_y}{H_x} = -\frac{\mu\omega}{k} \tag{2.16}$$

and

$$\frac{E_x}{H_y} = \frac{\mu\omega}{k}. \tag{2.17}$$

The resistivity of the half-space is then

$$\rho = \frac{1}{\mu\omega}\left|\frac{E_x}{H_y}\right|^2 \tag{2.18}$$

and similarly the ratio of E_y/H_x can be used. In the frequency domain, both **E** and **H** are complex and so another useful quantity is the phase Φ of the electric field relative to the magnetic field

$$\Phi = \mathrm{Arg}\left(\frac{E_x}{H_y}\right) = \mathrm{Arg}\left(\frac{\mu\omega}{k}\right) = \mathrm{Arg}\left(\frac{\mu\omega}{\sqrt{\sigma\mu\omega}}\, e^{i\frac{\pi}{4}}\right) = \frac{\pi}{4} \tag{2.19}$$

Thus, for a half-space Φ will always equal 45°. The ratio of E/H has units of Ohms and is referred to as the electrical impedance Z.

2.1.3 Apparent Resistivity

For the case where the conductivity structure is layered in the z direction, the solutions to equations 2.7 and 2.8 must now include terms for both downward

and upward traveling waves in each layer. The electrical impedance at the surface of a one-dimensional (1D) model can be found by adding the effects of upward and downward traveling electromagnetic fields within each layer. Each layer has both upward and downward traveling fields that behave according to equations 2.9 and 2.10, except that the sign of the βz term is positive for the upward traveling wave (i.e., the field decays as it travels upwards). Following the notation used in *Ward and Hohmann* [1988], the impedance $\hat{Z}_i$ at the top of layer i in a layered 1D model with N layers can be calculated with the recursive equation

$$\hat{Z}_i = Z_i \frac{\hat{Z}_{i+1} + Z_i \tanh(ik_i h_i)}{Z_i + \hat{Z}_{i+1} \tanh(ik_i h_i)}, \tag{2.20}$$

where h_i is the layer thickness i and Z_i is the intrinsic impedance of layer i

$$Z_i = \frac{\omega\mu}{k_i}. \tag{2.21}$$

The recursion starts at layer N and is bound on the bottom by an infinite half-space. Thus, h_{N+1} is infinite and $\tanh(ik_{N+1}h_{N+1}) = 1$, so the impedance of the terminating half-space $\hat{Z}_{N+1}$ is equal to the intrinsic impedance Z_{N+1}. The impedance can thus be propagated upward to the top of the next layer, and so on to the surface. An important thing to note is that the surface impedance at the top of a given layer is independent of the layers above. Thus, a 1D model with an ocean layer will have a seafloor impedance that is independent of the ocean layer. The surface impedance $\hat{Z}_1$, which is equal the ratio of the surface electric and magnetic fields, now can be transformed into an *apparent* resistivity ρ_a

$$\rho_a = \frac{1}{\omega\mu} \left| \frac{E_x}{H_y} \right|^2. \tag{2.22}$$

While ρ gave the true resistivity of the half-space, ρ_a contains the superimposed effects of reflection and attenuation from each layer and varies smoothly between frequencies, with higher frequencies more sensitive to shallow layers and the lower frequencies (longer skin depths) sensitive to deeper structure. Phase values of $\hat{Z}_1$ are no longer constrained to be the half-space 45°, and like the apparent resistivity will vary smoothly with frequency.

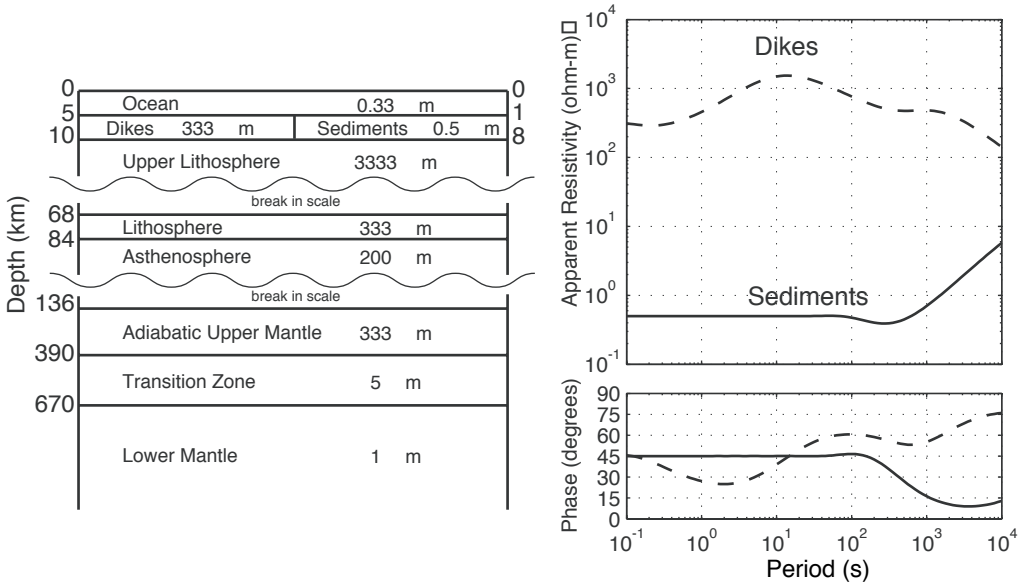

Figure 2.2: 1D Earth resistivity models (left) and MT responses (right) for the deep oceans and a sedimented margin.

As an example relevant to marine environment, Figure 2.2 shows the MT apparent resistivity and phase responses calculated by applying equation 2.20 to a reference deep ocean upper mantle resistivity profile [*Heinson et al.*, 1992] and a variation of that profile which includes 7 km of conductive (0.5 Ωm) sediments beneath the seafloor, representative of the continental shelf sediments in the Gulf of Mexico. The MT responses of the deep ocean and sediment models shown in Figure 2.2 provide an exemplary illustration of how dramatically the MT sensitivity depends on conductivity structure, mainly because electrical conductivity can have huge variations. While it is rare for seismic velocity structure to vary more than by a maximum factor of 5, electrical conductivity structure often has contrasts of 10-1000. The MT response of the deep oceanic model shows sensitivity to great depths as the result of the large skin depths of the fields in the resistive upper lithosphere and deeper layers. The peak in apparent resistivity at around 10-20 s period is from the high resistivity of the upper lithosphere. At periods of about 200-2000 s the response flattens and is mostly sensitive to the lower lithosphere, asthenosphere

and adiabatic upper mantle. At periods longer than about 2000 s, the apparent resistivity decreases in amplitude as the fields begin to sense the transition zone at depths of greater than about 400 km. While the deep ocean response is sensitive to structure deep in the mantle, the sediment model has relatively short skin depths over most of the frequency range and the apparent resistivity is that of the 7 km thick sediment layer until it starts becoming sensitive to the upper lithosphere at around 100 s period.

2.1.4 Electrical Impedance Tensor

In the presence of 2D and 3D structure, the apparent resistivity is dependent on the source field polarization and the measurement directions of the electric and magnetic fields. A more general approach is needed and one measures both horizontal components of the electric and magnetic fields to yield a tensor formulation for the electrical impedance [*Swift*, 1986]

$$\mathbf{E} = \mathbf{Z}\mathbf{H} \tag{2.23}$$

or

$$\begin{pmatrix} E_x \\ E_y \end{pmatrix} = \begin{pmatrix} Z_{xx} & Z_{xy} \\ Z_{yx} & Z_{yy} \end{pmatrix} \begin{pmatrix} H_x \\ H_y \end{pmatrix}. \tag{2.24}$$

$\mathbf{Z}$ is now independent of the source field polarization. In order to solve this underdetermined system of 2 equations and 4 unknowns for $\mathbf{Z}$, many samples of $\mathbf{E}$ and $\mathbf{H}$ can be used but there must be at least two different source field polarizations or the system will be singular. When the conductivity structure is 1D, for any rotation of $\mathbf{Z}$

$$Z_{xx} = Z_{yy} = 0 \tag{2.25}$$

and

$$Z_{yx} = -Z_{xy}. \tag{2.26}$$

For the 2D case, if the x or y axis is along strike then

$$Z_{xx} = Z_{yy} = 0 \tag{2.27}$$

and

$$Z_{xy} \neq -Z_{yx}. \tag{2.28}$$

For a 3D structure

$$Z_{xx} \text{ and } Z_{yy} \neq 0. \tag{2.29}$$

The source polarization independent apparent resistivity is then defined as

$$\rho_{xy} = \frac{1}{\omega\mu} |Z_{xy}|^2 \tag{2.30}$$

with phase

$$\Phi_{xy} = \arctan\left(\frac{\mathrm{Im}(Z_{xy})}{\mathrm{Re}(Z_{xy})}\right). \tag{2.31}$$

Similarly, Z_{yx} can be used. The MT phase contains no independent information in an ideal or mathematical case, but is useful because it is independent of the amplitudes of E and H.

The off-diagonal impedances in the 2D case form two independent modes. For the transverse electric (TE) mode, the electric field is oriented along the strike of conductivity structure (say, the x direction) and the magnetic field is oriented across strike. The Z_{xy} impedance is then referred to as the TE mode impedance. The other case is when the magnetic field is oriented along strike, known as the transverse magnetic (TM) mode. The electric current responds to conductivity structure differently in each mode and so the sensitivity of each mode differs.

2.2 Working in the Conductive Ocean

2.2.1 Filtering Effect of Seawater

As mentioned previously, the conductive seawater in the ocean has an attenuating effect on the incident MT source fields [e.g. *Chave et al.*, 1991; *Constable et al.*, 1998] and acts like a low-pass filter. Fields with skin depths much less than the ocean depth will experience severe attenuation, limiting the highest frequency MT fields observable on the seafloor. The attenuating effects of the ocean layer

can be easily derived for the 1D case. In a similar manner to [*Schmucker*, 1970, section 5], the ratio of the electric field E_{i+1} at the bottom of a layer i to the field at the top of the layer E_i is

$$\frac{E_{i+1}}{E_i} = \cosh(ik_ih_i) - \frac{Z_i}{\hat{Z}_i}\sinh(ik_ih_i) \tag{2.32}$$

and the magnetic field intensity ratio is

$$\frac{H_{i+1}}{H_i} = \frac{B_{i+1}}{B_i} = \frac{\hat{Z}_i}{\hat{Z}_{i+1}}\cosh(ik_ih_i) - \frac{Z_i}{\hat{Z}_{i+1}}\sinh(ik_ih_i), \tag{2.33}$$

where Z_i and $\hat{Z}_{i+1}$ are defined in section 2.1.3.

Figure 2.3 shows the attenuation of the electric and magnetic fields over a wide range of periods for various ocean thicknesses and seafloor resistivities. As the depth of the ocean becomes greater, both the short period E and B fields experience attenuation due to the relatively small skin depths at such periods. A marked difference is seen in the behavior of the electric and magnetic fields with seafloor resistivity. As the seafloor becomes more resistive, the magnetic field experiences an increasing amount of attenuation, which is seen even to very long periods. This results from $\hat{Z}_{i+1}$ in the denominator of equation 2.33, which increases with the seafloor resistivity. The seafloor electric field on the other hand experiences a slight increase in amplitude over simple half-space attenuation and is also greater at the surface since $E = ZH$. As the seafloor resistivity increases, so does Z (both at the seafloor and the sea surface), resulting in an increase of E. However, the impedance at the seafloor is larger because the sea surface impedance includes the effects of the conductive seawater. Some relative combination of E increasing and H decreasing is necessary to make the impedance larger at the seafloor larger.

It is also instructive to look at the effect of the ocean by plotting the field strengths versus depth, as shown in Figure 2.4. Both the electric and magnetic fields are normalized by the sea surface magnetic field. Near the sea surface H decays as a function of depth with a log-slope that is inversely proportional to the

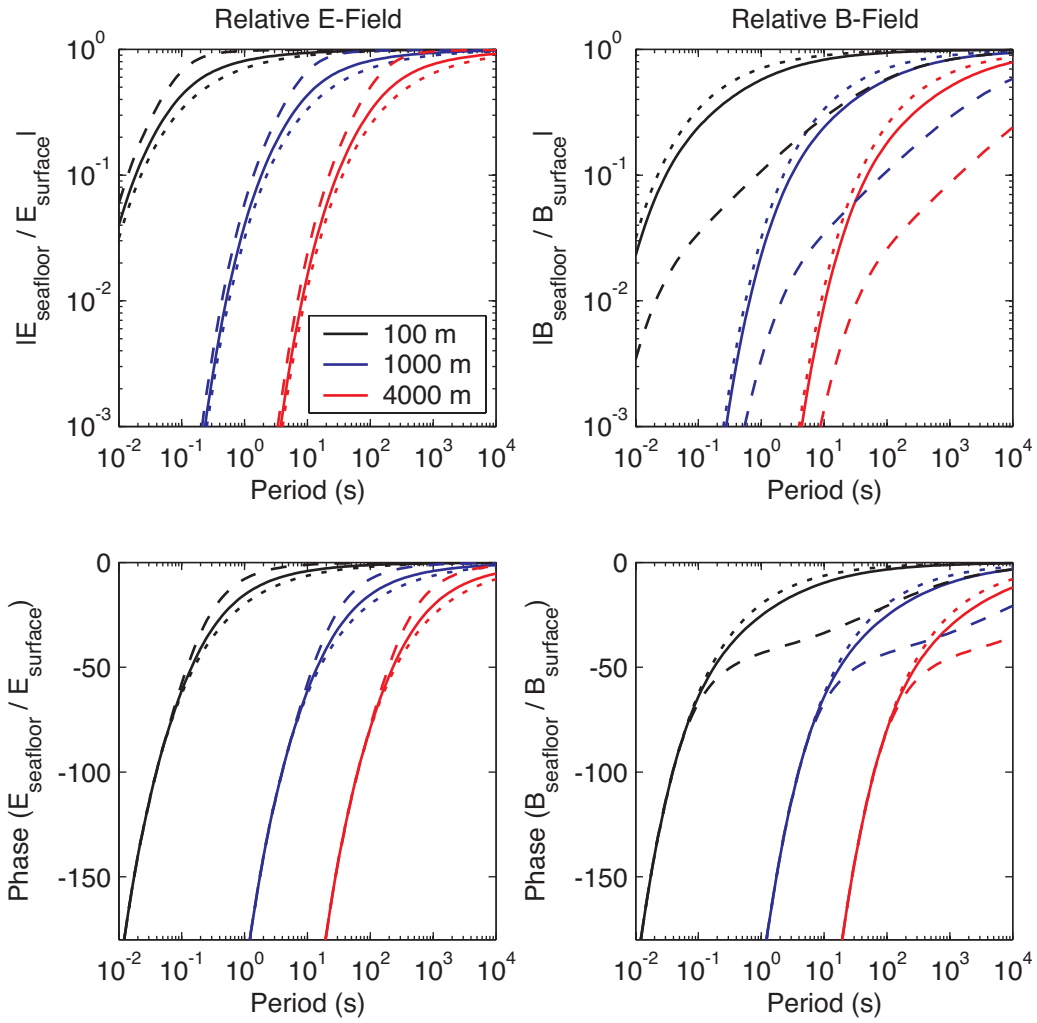

Figure 2.3: Attenuation of electric and magnetic fields by a seawater layer. The ratio of seafloor to sea surface fields is plotted as a function of period. Ocean thicknesses are 100 m (black), 1000 m (blue) and 4000 m (red). Seafloor resistivities are 1 Ωm (solid lines) and 100 Ωm (long dashed lines). Short dashed lines are for seawater half-space attenuation. Reproduced after *Constable et al.* [1998]

skin depth of the field. Above (but not below) the seafloor boundary, H calculated for the 1 and 100 Ωm seafloor models shows a deviation from the simple half-space attenuation. As the seafloor resistivity increases, the amount of attenuation occurring above the seafloor increases. As the period increases the range of depths over which the field shows more than half space attenuation increases. This can be thought of in terms of skin depth and reflections from the seafloor; longer period signals have a larger skin depth so the effect of the reflection is seen to greater distances. The reason for the abrupt change in the log-slope of H at the seafloor can be found from looking at the 1D equivalent of Ampere's law, equation 2.2

$$-\frac{\partial H_y}{\partial z} = i\omega\sigma E_x. \tag{2.34}$$

The boundary condition on the seafloor requires the continuity of the tangential component of the electric field (E_x) to be continuous. However, a jump in σ at the seafloor requires a change in the derivative of H_y at the seafloor. Since σ decreases at the seafloor, so does the derivative of H_y (note: the log scale x-axis in Figure 2.4 makes it look as though the derivative of H actually increases). Below the seafloor H decays with a log-slope inversely proportional to the skin depth of the half space and shows none of the curvature present above the seafloor. The electric field E shown in Figure 2.4 is normalized by the sea surface magnetic field, making the sea surface E equivalent to the sea surface impedance. The impedance is proportional to $\sqrt{\omega\rho}$ so shorter periods and more resistive seafloor values give a larger normalized E. As shown from Ohm's Law, $J = \sigma E$, the current density J is much higher in the ocean layer ($\sigma = 3.3$ S/m) than in the seafloor layer ($\sigma = 0.01$ and 1 S/m). What is also seen from Figure 2.4 is that on the seafloor both E and H will vary with the seafloor resistivity, in contrast to the 1D case on land where most of the variation is found in E.

2.2.2 Amplitudes of Seafloor Electric and Magnetic Fields

The average strength of the seafloor magnetic fields can be calculated by taking an average land magnetic field spectrum [*Constable and Constable*, sub-

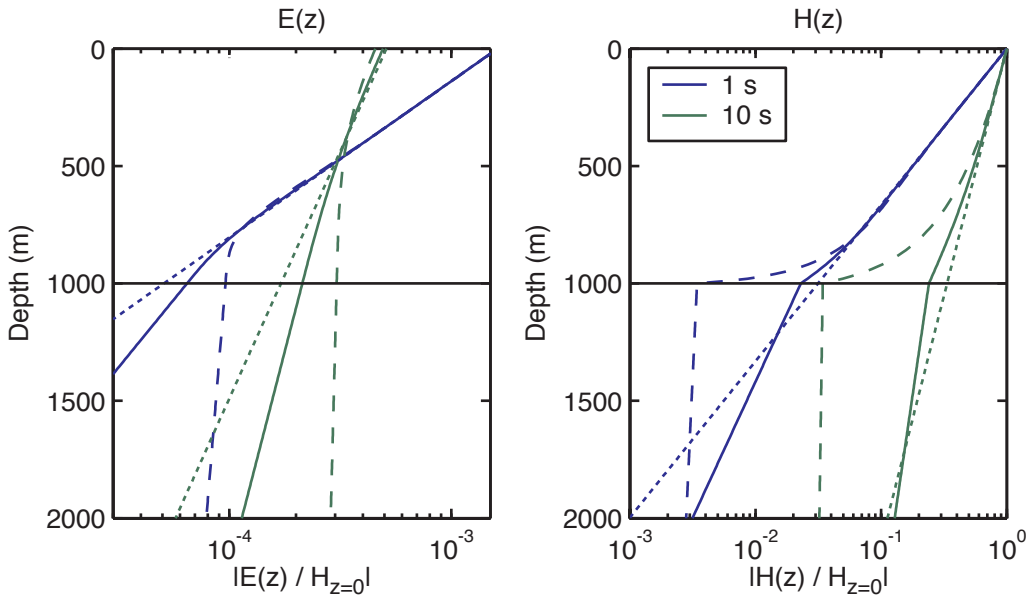

Figure 2.4: Electric and magnetic fields in the ocean as a function of depth for a 1000 m thick ocean. Seafloor resistivity is 1 Ωm (solid line) and 100 Ωm (long dashed line). The short dashed line is for seawater half-space attenuation. Both fields are normalized by the strength of the sea surface magnetic field.

mitted, 2003] and propagating the field down to the seafloor using equation 2.33 and an appropriate 1D resistivity profile. Although the magnetic source field is not stationary and can vary in strength by more than an order of magnitude, this exercise is useful because it provides a general estimate of expected field strengths around which surveys and sensors can be optimized to a particular environment. Complications from 2D and 3D structures beneath the seafloor are neglected. The seafloor electric field E_x is calculated from the downward propagated magnetic field H_y as

$$|E_x| = |Z||H_y| = \sqrt{\frac{\omega\rho_a}{\mu}}\,|B_y|\,. \tag{2.35}$$

Equation 2.35 shows that the seafloor electric field is proportional to the square root of the frequency and the apparent resistivity times the seafloor magnetic field. Since the magnetic field has a "red" spectrum, the square root of frequency dependence means the electric field has a whiter spectrum than the magnetic field.

This analysis was applied to the reference deep ocean upper mantle resis-

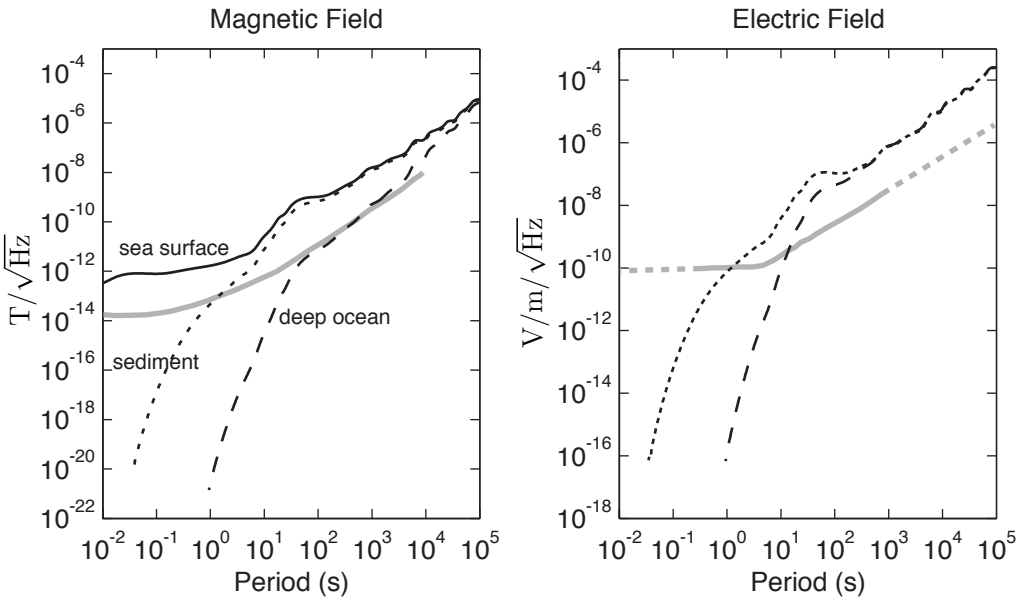

Figure 2.5: Expected seafloor magnetic and electric field amplitudes. The thick black line is the sea surface magnetic field, short dashed lines are the seafloor fields from the sediment model, and long black lines are seafloor fields from the deep ocean model. Gray lines are induction coil magnetometer and electrode noise levels (dashed where inferred).

tivity profile [*Heinson et al.*, 1992] and the variation of that profile which includes 7 km of conductive (0.5 Ωm) sediments, which were shown along with MT responses in Figure 2.2. The expected seafloor fields are shown in Figure 2.5. The deep ocean model shows more high frequency attenuation due to the thicker ocean layer attenuation of the fields. The deep ocean magnetic field also shows much more attenuation due to the highly resistive seafloor, as also shown in Figures 2.3 and 2.4. Included in the plots are estimated noise spectra for commercial BF4 induction coil magnetometers [*Nichols et al.*, 1988] and seafloor electric field sensors [*Constable et al.*, 1998]. In the sediment model both the seafloor magnetic and electric fields are above the noise spectra at periods greater than about 1 s. For the deep ocean model the electric field is above the noise spectra for periods greater than about 10 s, however, the severe attenuation of the magnetic field even to long periods results in the field being nearly equal with the magnetometer noise

level for periods greater than about 50 s and lower in strength the noise level for periods less than about 50 s. This example provides a guide to the feasibility of both continental shelf and deep ocean MT exploration and is consistent with what we have seen (see Chapters 3 and 4). To boost the signal-to-noise ratio where the signal is close to the instrument noise, one can leave the instrument on the seafloor for a longer recording time to get a $\sqrt{N}$ (where N is the number of samples) improvement in the field estimate and to detect occasional large events that are much stronger than the average field. High frequency measurements become hopeless because of the rapid fall off in field strength.

2.2.3 Vertical Current at the Seafloor

Hoversten et al. [1998] show that for 2D or 3D structures, the horizontal **E** and **H** components on the seafloor can still be related by a 2×2 impedance tensor, but that the seawater layer may have to be included to correctly handle the boundary condition on the seafloor. On land, the boundary condition is that no vertical current can exist at the air-earth interface due to the extremely small conductivity of air (about 10^{-17} S/m). On the seafloor, however, the conductive seawater allows vertical current to flow and this creates a subtle difference from conventional land-based 2D MT theory. The point is nicely illustrated by looking at the vertical current term from Ampere's Law (equation 2.2)

$$\frac{\partial H_y}{\partial x} - \frac{\partial H_x}{\partial y} = J_z. \tag{2.36}$$

On land the J_z term is zero from the boundary condition. Additionally, for the TM mode the source magnetic field is H_x and the magnetic field H_y is then by definition zero, and as equation 2.36 shows, the spatial variation of H_x in the y direction must be zero. In other words, the TM mode on land has a uniform H_x field at the air-earth interface. On the seafloor this situation no longer holds because the conductive seawater allows for a vertical current (J_z) term. If the conductivity structure forces current up into the sea water, J_z will be non-zero

and thus H_x will vary in the y direction. *Hoversten et al.* [1998] considered the case of a resistive anticline structure at a depth of 1 km beneath the seafloor and showed that the TM mode response changes by up to 18% when the seawater layer is included in the model. Even more dramatic structures, particularly ones with large 2D or 3D resistive features near the seafloor, would result in an even bigger effect on the TM response. So, while the 1D impedance theory discussed earlier showed that the seafloor impedance is not sensitive to the overlying sea water, in 2D and 3D cases it is essential to include the ocean in numerical models when conductivity variations near the seafloor are suspected.

2.2.4 Distortions from Bathymetry

The shape of the seafloor can have major distorting effects on the electric and magnetic MT fields observed on the seafloor, even when the topography local to the station is flat. For example, *Heinson et al.* [1993] show that MT fields observed on the Juan de Fuca Ridge are primarily due to non-uniform induction within the ocean as a result of changes in the ocean depth. Similarly, a long period marine MT study at the Society Islands hotspot [*Nolasco et al.*, 1998] found MT response functions were strongly influenced by bathymetric and island effects.

A simple model study of a smoothly varying bathymetric rise illustrates the magnitude and lateral extent that bathymetry can distort MT responses. The model consists of a 1 km increase in the seafloor depth which occurs smoothly over a 20 km horizontal distance with a maximum gradient of 5°, as shown in Figure 2.7. The bathymetry is approximated using a finite element mesh with piecewise smooth sloping triangular elements. Using a standard 2D MT finite element code [*Wannamaker et al.*, 1987], MT responses for sites located along the seafloor at lateral positions of -50 to 50 km were calculated at periods of 1-10,000 s for three models using seafloor resistivities of 1, 10 and 100 Ωm. The FE code calculates the model strike aligned field (E_x for the TE mode, H_x for the TM mode) for every node in the mesh. The code was modified so that the auxiliary (y directed or

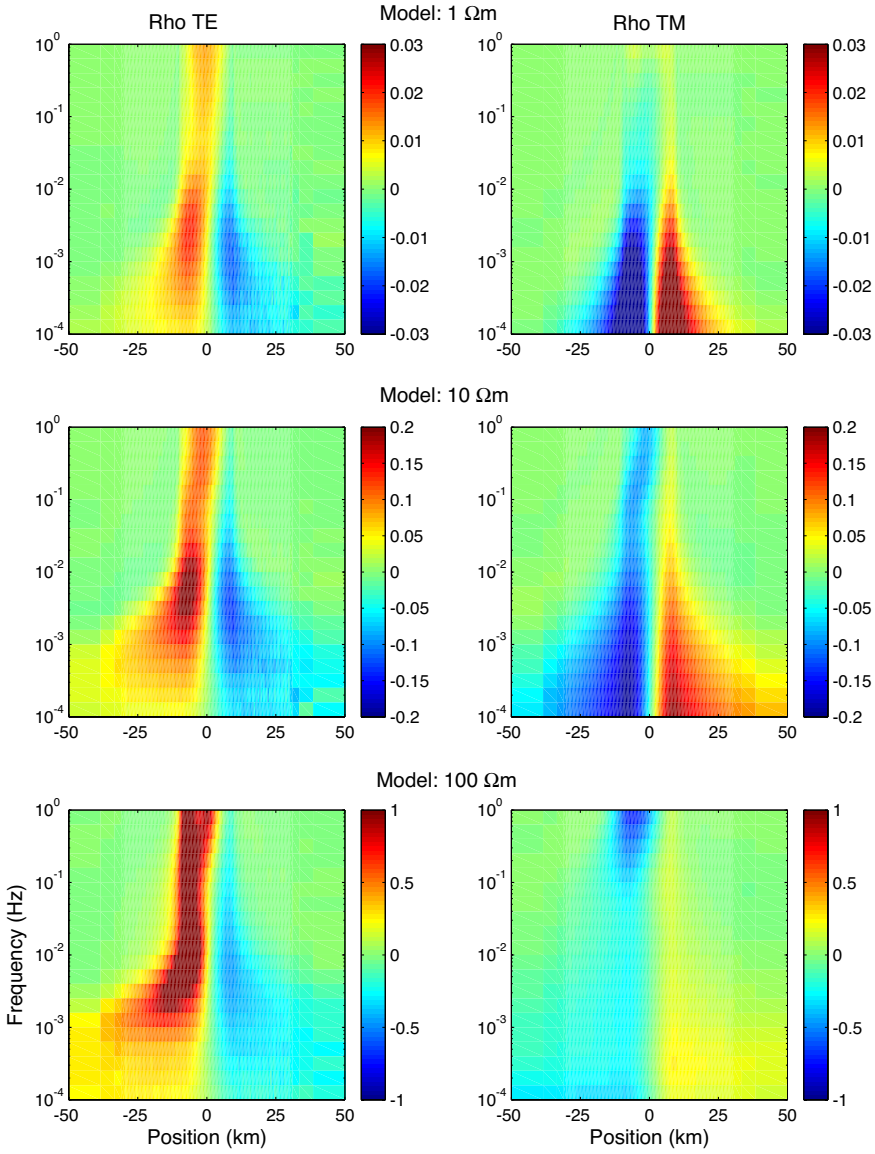

Figure 2.6: Anomalous MT apparent resistivity responses from the sinusoidal bathymetry step model shown in Figures 2.7 and 2.8. The MT responses are plotted for sites located along the seafloor at positions of -50 to 50 km and periods of 1-10,000 s. The anomalous response is the logarithm of the ratio of the MT apparent resistivity response to the seafloor resistivity. Therefore, a value of zero corresponds to a response equivalent to the 1D response and free of distortions from bathymetry. A value of ± 1 corresponds to an order of magnitude distortion in the response. The in-line field was calculated along the slope of the bathymetry, as is done with real data. Note the changing scale.

across strike) field at each seafloor site, which is combined with the strike aligned field to yield the impedance, is taken to be the field tangential to the seafloor slope, as opposed to using only the strictly horizontal field. This is to mimic real data, in which a seafloor instrument is most likely to be oriented parallel to the seafloor slope. The anomalous MT responses calculated from this study are shown in (Figure 2.6). The anomalous response is the logarithm of the ratio of the MT apparent resistivity to the seafloor resistivity. Therefore, a value of zero corresponds to a response equivalent to the 1D response and free of 2D distortions from the bathymetry; likewise a value of ± 1 corresponds to an order of magnitude distortion in the response.

The 1 Ωm model responses, shown in the top row in Figure 2.6, show anomalous responses up to $0.02 - 0.04$, corresponding to about a 5-10% difference from the 1D response. The most dramatic effects are seen at periods in excess of about 300 seconds for the TM mode. The distortions are present within the region containing the sloping seafloor (-10 to 10 km) and also extend outside this region at longer periods. Marine environments such as the northern Gulf of Mexico, offshore west Africa and other similarly heavily sedimented continental margins have crustal resistivity structure on the order of about 1 Ωm and so this model study illustrates that similar or less dramatic bathymetry features in these regions will have negligible effects on measured MT responses for periods less than about 300 s, but may have an appreciable effect at longer periods. Anomalous responses for the 10 Ωm model, shown in the second row of Figure 2.6, are as large as about ± 0.2 (or about 60%) for sites located within the region of the bathymetric rise and have smaller effects that extend to at least ± 50 km at longer periods. The distortions become even larger and extend to a farther lateral extent when the seafloor resistivity is increased to 100 Ωm, as shown in the bottom row of Figure 2.6. At mid-ocean ridges, where the bathymetric relief is dramatic and the upper crust beneath the seafloor has a resistivity of around 10-100 Ωm, MT data can be distorted by the shape of the seafloor, even for sites located 10's of kilometers

away from bathymetry features. The general distorting effect of the bathymetry rise modeled here is an increase in the TE and a decrease in the TM responses for sites located on the lower half of the bathymetry, while sites located on the upper half show an increase in TM and a decrease in TE response. More complicated structures such as 3D shaped seamounts and basin-like structures will have more complex distortions than the simple rise modeled here.

While the distorted MT responses show the dependence on period and extent of bathymetry effects, inspection of the electric and magnetic fields elucidates the nature of the distortions. Strike aligned electric and magnetic fields at each FE mesh node are shown for periods of 1 and 100 s for the 1 Ωm model (Figure 2.7) and the 100 Ωm model (Figure 2.8). The TE mode E_x and TM mode H_x fields for the 1 s period and 1 Ωm model in the top of Figure 2.7 both show attenuation through the ocean (the white portion of the model) and the seafloor. On the right side of the model, the fields entering the seafloor have larger skin depths (due to the increase in resistivity) and do not attenuate as fast as in the ocean (more closely spaced contours means the field is attenuating more). The same thing happens on the left side of the model, except that the fields travel through a thicker ocean and thus are attenuated more when reaching the seafloor. Continuity of tangential fields requires the contours on the left and right sides to smoothly meet in the sloping bathymetry region. When the seafloor resistivity is increased to 100 Ωm, as shown in the top model of Figure 2.8, the effect is even more pronounced due to the larger skin depth of the fields beneath the seafloor. When the period is increased (the bottom models of Figures 2.7 and 2.8), the skin depth increases in both the ocean and the seafloor, resulting in even more complicated effects. At 100 s period the skin depth in the ocean is about 3 km, or 3 times the ocean depth on the model right side. Thus, the field at the ocean surface is sensitive to reflections from the flat seafloor and the sloping bathymetry.

Auxiliary fields for each mode can can found using Ampere's Law (equa-

tion 2.2) for the TE mode

$$H_y = \frac{i}{\omega\mu}\frac{\partial E_x}{\partial z} \qquad H_z = -\frac{i}{\omega\mu}\frac{\partial E_x}{\partial y}, \tag{2.37}$$

and by using Faraday's law (equation 2.1) for the TM mode

$$E_y = -\frac{i}{\omega\sigma}\frac{\partial H_x}{\partial z} \qquad E_z = \frac{i}{\omega\sigma}\frac{\partial H_x}{\partial y}. \tag{2.38}$$

Unlike the electric field, the magnetic H_x field contours (shown in red) bend up around the bathymetry rise, especially for the 100 s period 100 Ωm model. The reason for this can be found by considering the auxiliary electric E_y field and its current density $J_y = \sigma E_y$. Equation 2.38 shows that J_y is proportional to the attenuation of the H_x with depth. As Figure 2.8 shows, when the seafloor becomes much more resistive than the ocean H_x is much more attenuated in the ocean than the seafloor. Consequently, the J_y is much higher in the ocean than the seafloor and this induced current will tend to stay in the conductive ocean rather than the resistive seafloor. Thus, J_y current density in the ocean will increase from left to right across the model as the current is squeezed into a shallower ocean. In order to support such high current densities, the H_x must attenuate more in the ocean on the right side of the model, hence the bending up of the contour lines. Vertical fields are also generated by the bathymetric slope. As shown in equations 2.37 and 2.38, lateral gradients in the field contours result in vertical magnetic (H_z) and electric (E_z) fields. Both Figures 2.7 and 2.8 show upward or downward bends in the contour lines that indicate lateral field gradients and the presence of vertical fields. The vertical electric field E_z is also the result of charge build-up on the sloping bathymetry.

Several solutions to handling bathymetry in numerical models have been proposed. For very long period (> 500 s) studies the thin-sheet method [*Vasseur and Weidelt*, 1977; *McKirdy et al.*, 1985; *Ranganayaki and Madden*, 1986] can be used to either include or remove 3D bathymetric distortions. The thin-sheet approximation is that for sufficiently long periods, the skin depth is large enough

that the electric field is not attenuated at all in the ocean layer and the 3D problem can be transformed into a 2D problem by converting the ocean layer into a thin-sheet of lateral varying conductance (determined by the water depth and sea water conductivity). This approach has used to estimate bathymetric effects [*Heinson et al.*, 1993] and to remove the bathymetry distortion from the MT impedance [*Nolasco et al.*, 1998]. In addition to being accurate only at long periods, the method is also seriously limited because the thin-sheet can only be underlain by 1D structure and therefore limits the scope of resulting models to be 1D. Topography can also be included in finite difference (FD) modeling codes as steps or blocks in 2D and 3D meshes. The scale of bathymetry structure is much less than the usual target dimensions and requires many more nodes to mesh than for the target region. Additionally the rectilinear nature of standard FD meshes means that the small node spacings extend both laterally and horizontally to the ends of the mesh, resulting in computationally expensive meshes. A more recent approach uses a material transformation tensor to effectively flatten the seafloor topography [*Baba and Seama*, 2002] and results in much smaller FD meshes. Unlike the thin-sheet method, this method does not suffer from an inherent frequency limitation and can be adapted to handle short periods. At mid-ocean ridges where the bathymetry is often predominantly 2D, the finite element code described previously [*Wannamaker et al.*, 1987] has been used to effectively include bathymetry in numerical models (see Chapter 4).

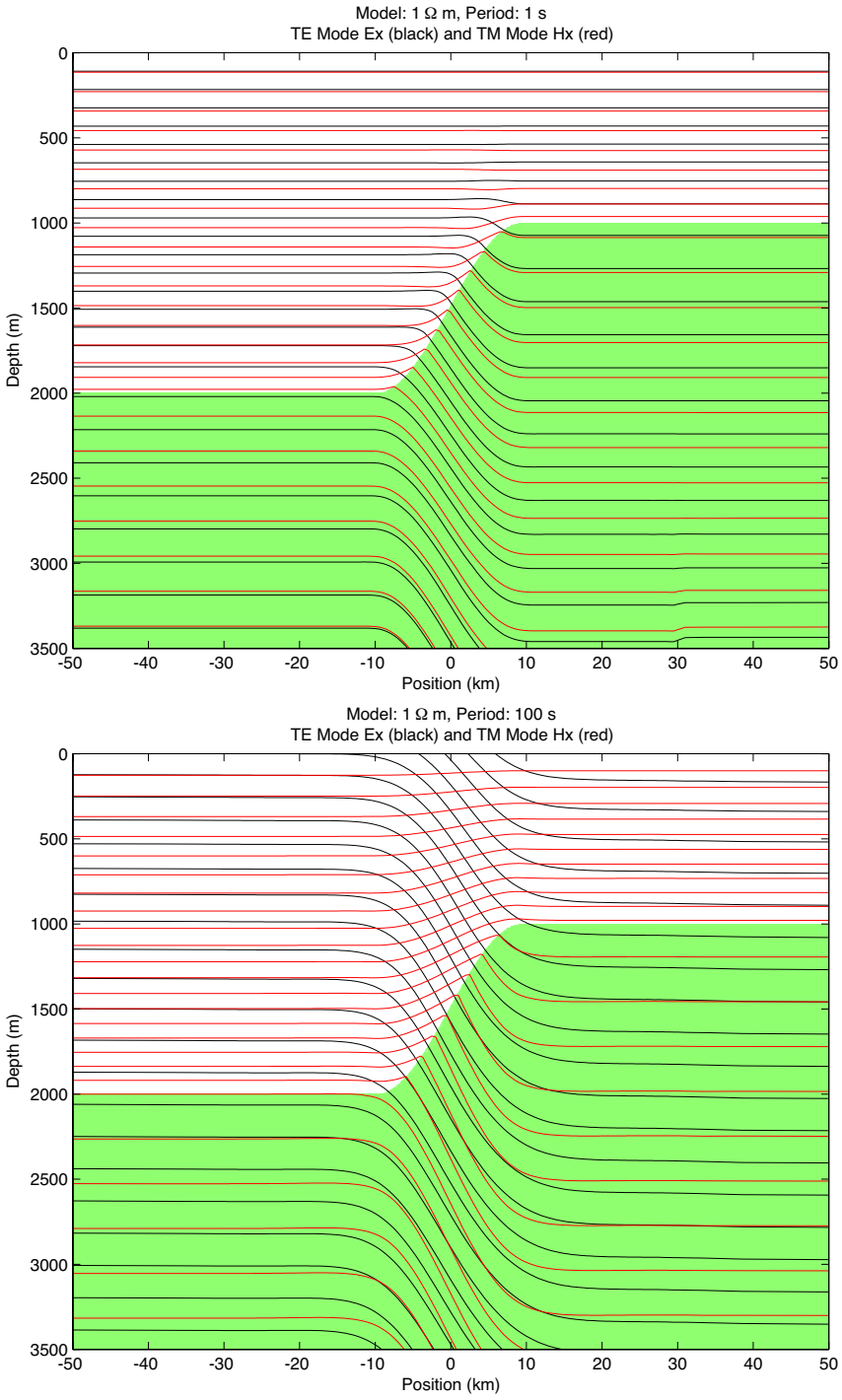

Figure 2.7: MT electric and magnetic field magnitudes at 1 s (top) and 100 s (bottom) period for a 1 Ωm sinusoidal bathymetry step 1 km high and 20 km wide. The TE mode E_x field is shown as black contours (x points into the page) and the TM mode H_x field is shown as red contours. The contours are of $\log_{10}$ field magnitude.

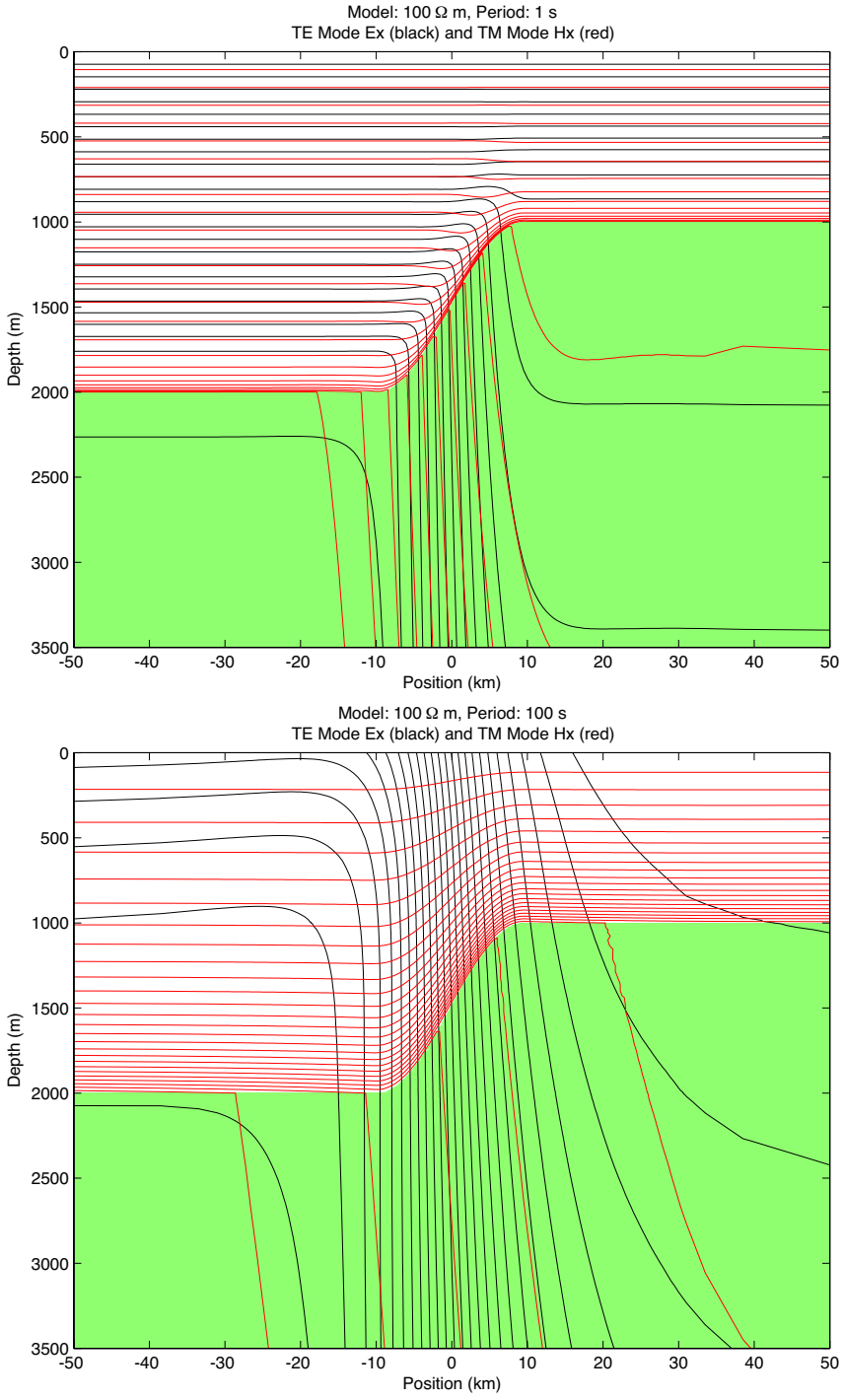

Figure 2.8: MT electric and magnetic field magnitudes at 1 s (top) and 100 s (bottom) period for a 100 Ωm sinusoidal bathymetry step 1 km high and 20 km wide. The TE mode E_x field is shown as black contours (x points into the page) and the TM mode H_x field is shown as red contours.

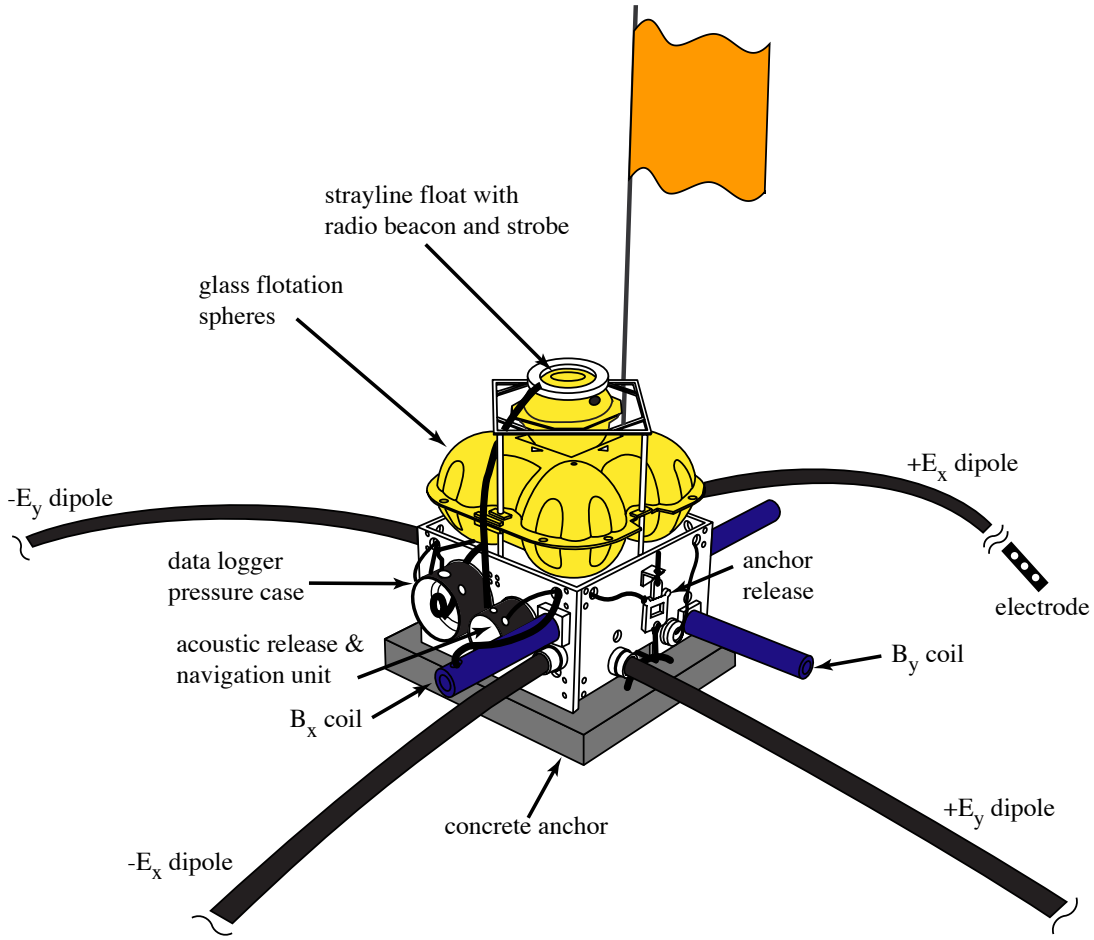

Figure 2.9: Diagram of the Scripps Institution of Oceanography broadband marine MT instrument [*Constable et al.*, 1998].

2.3 Broadband Instrumentation

Marine magnetotelluric instrumentation underwent a major advancement during the late 1990's with the introduction the Scripps Institution of Oceanography broadband marine MT instrument [*Constable et al.*, 1998], which enabled measurement of shorter period signals than before. Traditional marine MT instrumentation used by academics to study the mantle [e.g. *Filloux*, 1980] utilized fluxgate magnetometers and DC coupled electric field sensors which measured fields in the period range of about 500-100,000 s. As has already been shown in Figure 2.2, such long periods are not very sensitive to structures at the relatively shal-

low depths (0-10 km) of petroleum exploration targets on the continental shelves and the crustal and upper mantle magmatic systems at mid-ocean ridges. The broadband instrument [*Constable et al.*, 1998] overcomes this difficulty by utilizing AC-coupled sensors which remove the large DC (i.e. very long period) portion of the signal so that the smaller signal at periods of about 0.1-10,000 s can be amplified to a suitable recording level. Over the past 8 years, refinements developed from nearly 1000 commercial and academic deployments have resulted in a highly reliable, robust and efficient marine instrument system. A diagram of the instrument is shown in Figure 2.9.

The current (October, 2003) instrument configuration is described as follows. A system of low noise and low impedance silver-silver chloride electrodes and an AC-coupled electric field amplifier [*Webb et al.*, 1985] measures the horizontal electric field at the end of 10 m long dipole arms. A stiff vertical arm can also be added to record vertical electric fields for controlled-source electromagnetic surveys. The electric field amplifier has a gain of 10^6 and uses a one-pole low-cut filter with a corner frequency at 10 s period. Horizontal magnetic fields are measured using highly sensitive, light weight and low power induction coil magnetometers [*Key and Constable*, in preparation]. The magnetometer consist of a 174 cm long and 1.25 cm diameter Permalloy bar (high magnetic permeability) with 4 bobbins of aluminum wire coils (about 44,000 turns total). Since instruments must be floated back to the surface under their own buoyancy, weight is an important consideration; aluminum wire is used rather than copper since it has a density one-third that of copper. Sensor weight is thus minimized, decreasing the recovery time and increasing survey efficiency. The Permalloy bar acts to gather magnetic flux with a resulting gain of about 4000 times more flux passing through the windings than if no bar was used. The magnetic field amplifier used is similar to that for the electric field amplifier but has no low-cut filtering, since the induction coil magnetometer has a natural response proportional to the signal frequency. This configuration makes the instrument capable of measuring both electric and mag-

netic fields in the 0.1 to 10,000 s period range, although the attenuation of the natural source MT fields through the ocean limits the shortest periods to about 1-10 s, depending on the depth of water (see section 2.2.1). Each instrument is outfitted with a state-of-the-art, 4 or 8 channel, 24-bit data logger. All instruments utilize Seascan clocks with drift rates of less than 5 ms/day. A 150 kg concrete anchor stabilizes the instrument on the seafloor. An independent acoustic unit is used to track the instrument through the sea column during deployment and recovery, and also for releasing the instrument from the anchor. An electronic magnetic compass/tiltmeter records the instrument's orientation on the seafloor. A stray-line buoy containing a strobe light, fixed light, and radio beacon ensure instrument recoveries can be performed at night and in limited visibility conditions during daylight. An example of the time series data collected with this instrument in the Gulf of Mexico (see Chapter 3) is shown in Figure 2.3.

Figure 2.10: Time series of electric and magnetic fields collected at Gemini Prospect, Gulf of Mexico (see Chapter 3).

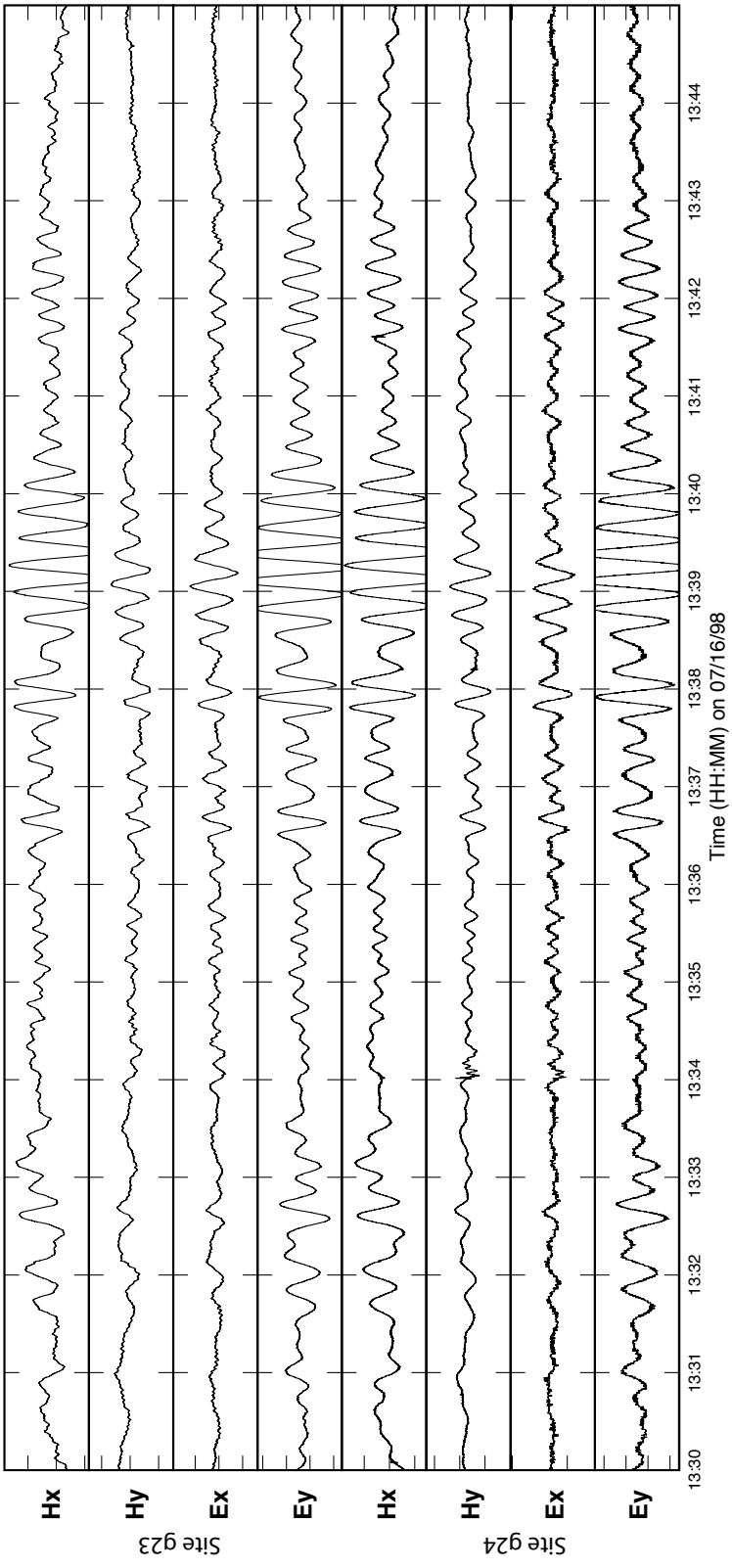
Hx
Hy
Ex
Ey
Site g23
Hx
Hy
Ex
Ey
Site g24
13:30
13:31
13:32
13:33
13:34
13:35
13:36
13:37
13:38
13:39
13:40
13:41
13:42
13:43
13:44
Time (HH:MM) on 07/16/98

2.4 Data Processing

After electric and magnetic time series are collected, impedance tensor estimates for each site are made for discrete, evenly spaced frequencies. Processing of the time series to yield impedance tensor estimates is referred to as data processing, and MT responses (impedances or apparent resistivities) output from the data processing are typically referred to as MT data, since this is the quantity fit by forward and inverse models. Several major advancements in magnetotelluric data processing have occurred in the past 20 years. The current state-of-the-art method for data processing is a robust multiple-station processing routine by *Egbert* [1997; 2002]. While this work progresses techniques established by its predecessors, major new features of this code allow for much stronger characterization of time series and MT responses than previously available. Since most MT surveys now involve simultaneous collection of data at multiple MT stations, more reliable estimates of the impedance tensor are made by using the information from all data channels to discriminate between signal and noise. Egbert's code has been adapted and modified to accommodate the Scripps MT data format, and marine MT responses calculated using this technique are presented in Chapters 3 and 4. Below is a review of the evolution of MT processing with an emphasis on the multiple-station routine.

2.4.1 Basics

Working in the frequency domain, the goal of MT data processing is to provide noise free estimates of the 2×2 impedance tensor $\mathbf{Z}$ at many frequencies over the band of interest. Noise in MT data can often be intermittent, and so the first attempt in minimizing noise in $\mathbf{Z}$ is to make many estimates of $\mathbf{Z}$ and to average them. This is accomplished by dividing the time series up into many small pieces and performing a fast Fourier transform (FFT) on each section, yielding frequency domain estimates of the electric and magnetic fields, referred to as

Fourier coefficients (FCs). If the MT fields are stationary and not corrupted by intermittent noise, a long FFT of the entire time series would provide FCs from which an adequate estimate of $\mathbf{Z}$ for each frequency could be made. However, noise can be intermittent and the source fields non-stationary, so a large set of FCs allows for discrimination between "good" and "bad" sections of the time series. Impedance estimates are usually desired over a broad range of frequencies (usually several decades) and so a technique known as *cascade decimation* [*Wight and Bostick*, 1986] is utilized. The basic idea behind cascade decimation is to maximize the number of FCs calculated in a given frequency band, thus allowing for non-stationary source fields and also for noise minimization by averaging. The time series is divided up into small overlapping windows (usually about 128 samples per window with an overlap of about 25%) and transformed into the frequency domain using the multitaper method [*Thomson*, 1982]. Then the original raw time series is low-pass filtered and decimated (usually by a factor of 2-4) to a lower sampling frequency. The decimated data are transformed to the frequency domain, providing another set of FCs at a lower frequency band. This process repeats itself until FCs for the lowest frequency band of interest have been calculated. The FCs calculated from this process are then corrected for instrument sensor calibrations and amplifier gains. Once a suitable set of FCs is calculated, the next step is to use the FCs to form a reliable estimate of $\mathbf{Z}$. Several methods for this have been proposed. The next few sections are a review of these methods.

2.4.2 Least Squares Analysis

The classic least squares analysis used in MT studies during the 1960's and 1970's was to estimate the impedance tensor at a given frequency band by fitting the FCs in a least squares sense. The method starts by defining a residual vector $\mathbf{r}$ that measures the misfit of the impedance estimate $\hat{\mathbf{Z}}$ to the set of FCs for the electric and magnetic fields in a given frequency band

$$\mathbf{r} = \mathbf{E} - \mathbf{H}\hat{\mathbf{Z}}, \tag{2.39}$$

where $\mathbf{r}$, the electric field FCs $\mathbf{E}$ and the magnetic field FCs $\mathbf{H}$ are $N \times 2$ vectors, $\hat{\mathbf{Z}}$ is 2×2 and N is the number of FCs (number of frequencies in a band times number of time windows used per frequency band). Least squares estimation (also known as L2 norm minimization) seeks to find the solution that minimizes the sum of the squared data residuals, written as a norm

$$\min \left| \mathbf{r}^{\dagger} \mathbf{r} \right| = \min \left| \left(\mathbf{E} - \mathbf{H}\hat{\mathbf{Z}} \right)^{\dagger} \left(\mathbf{E} - \mathbf{H}\hat{\mathbf{Z}} \right) \right|, \tag{2.40}$$

where $\dagger$ denotes the complex conjugate transpose. Seeking the minimum of $\mathbf{r}^{\dagger}\mathbf{r}$ we take the derivative of equation 2.40 with respect to $\hat{\mathbf{Z}}$ and set it equal to zero, yielding the classic least squares normal equations

$$\hat{\mathbf{Z}} = \left(\mathbf{H}^{\dagger}\mathbf{H} \right)^{-1} \mathbf{H}^{\dagger}\mathbf{E}. \tag{2.41}$$

$\mathbf{H}^{\dagger}\mathbf{H}$ and $\mathbf{H}^{\dagger}\mathbf{E}$ are averaged autopower and cross-power spectral estimates. Implicit in the least squares analysis is that $\mathbf{H}$ (i.e. the input of the process) is noise free. While any uncorrelated noise in both $\mathbf{E}$ and $\mathbf{H}$ won't affect the cross-power term $\mathbf{H}^{\dagger}\mathbf{E}$, noise in $\mathbf{H}$ causes the autopower term $\mathbf{H}^{\dagger}\mathbf{H}$ to be overestimated and will bias downward the impedance amplitudes [e.g. *Sims et al.*, 1986]. A simple way to overcome this shortcoming is by using the remote reference technique.

2.4.3 Remote Reference Analysis

The remote reference technique [*Gamble et al.*, 1979] utilizes measurements of $\mathbf{H}$ at an additional (remote) site to reduce the effects of noise in $\mathbf{H}$. The remote site's location is chosen to be sufficiently far away that noise in the remote site's measured magnetic field intensity $\mathbf{H_R}$ will not be coherent with noise in the local $\mathbf{H}$, but sufficiently close that the magnetic source field is uniform between the remote and local sites. A residual vector $\mathbf{r_R}$ can then be defined as in equation 2.39, but using $\mathbf{H_R}$ instead of $\mathbf{H}$. The remote reference solution which minimizes the norm $\left| \mathbf{r}_{\mathbf{R}}^{\dagger}\mathbf{r} \right|$ is

$$\hat{\mathbf{Z}} = (\mathbf{H}_{\mathbf{R}}^{\dagger}\mathbf{H})^{-1}\mathbf{H}_{\mathbf{R}}^{\dagger}\mathbf{E}.$$

If the noise between the two sites is incoherent then the cross-power term $\mathbf{H_R^\dagger H}$ will not be overestimated and $\hat{\mathbf{Z}}$ will not be biased downward as in the least squares estimate.

2.4.4 Robust Remote Reference Analysis

The remote reference technique greatly improved MT processing over least squares methods by reducing the effect of noise in the magnetic components. What the remote reference technique lacks is the ability to deal with large outliers (noise) present in the data at both the site of interest and the remote site. Large outliers violate the least squares assumption of normally (Gaussian) distributed residuals and can lead to catastrophic failure of the least squares approach. A scheme that can form reliable estimates in the presence of outliers in the data is said to be "robust". One such scheme is known as a regression M-estimate, and like the least squares method seeks to minimize the difference between the prediction and observations [e.g. *Egbert and Booker*, 1986; *Chave and Thomson*, 1989]. M-estimates are a variation of maximum likelihood estimates and seek to find the model parameters that are most likely given the probability distribution of the data. The solution is similar to the least squares normal equations, but with an adaptive weight term added

$$\hat{\mathbf{Z}} = \left(\mathbf{H}^\dagger \mathbf{w} \mathbf{H}\right)^{-1} \mathbf{H}^\dagger \mathbf{w} \mathbf{E}.$$

The weight function $\mathbf{w}$ is determined by the size of the residual of each segment

$$w(\mathrm{r}) = \begin{cases} 1 & |\mathrm{r}| < r_0 \\ r_0 / |\mathrm{r}| & |\mathrm{r}| \geq r_0 \end{cases}.$$

Typically r_0 is set to 1.5 times the standard deviation. For small residuals (r$\leq r_0$ standard deviations) the weighted observations are identical to their original observation (as in L2 minimization), but larger residuals are down-weighted towards their predicted values. This method is solved iteratively by initially solving for $\hat{\mathbf{Z}}$ using least squares, then forming weights based on the residual and using

the weighted least squares equations until convergence. To eliminate the worst points completely the final two iterations proceed with Thomson's weight function [*Egbert and Booker*, 1986]

$$w(\mathrm{r}_i) = \exp\left\{-\exp\left(r_0(|\mathrm{r}| - r_0)\right\}\right.,$$

with r_0=2.8. The benefits of the remote reference technique can be included with the robust weighting scheme by replacing $\mathbf{H}^\dagger$ with $\mathbf{H}^\dagger_{\mathbf{R}}$, giving the robust remote reference equation

$$\hat{\mathbf{Z}} = \left(\mathbf{H}^\dagger_{\mathrm{R}}\mathbf{w}\mathbf{H}\right)^{-1}\mathbf{H}^\dagger_{\mathrm{R}}\mathbf{w}\mathbf{E}.$$

2.4.5 Robust Multiple-Station Processing

The previous three subsections all used a univariate regression for the model

$$\mathbf{E} = \mathbf{H}\mathbf{Z} + \mathbf{r}. \tag{2.42}$$

This model explicitly allows for noise, but only in **E**. While the robust remote reference method can minimize incoherent noise in **H** and damp out the effects of severe outliers, it lacks the ability to explicitly include noise in **H** and does not provide a means to estimate coherent noise and non-plane wave source field effects. In other words, coherent noise and non-uniform source effects will be folded into the estimate of **Z** with no diagnostic to reveal their presence other than that **Z** may look unusual or have non-physical behavior. An alternative method known as the robust multivariate errors-in-variables (RMEV) approach [*Egbert*, 1997; 2002] allows for noise on all channels as well as providing an estimate of the source field dimension. This technique incorporates data from multiple simultaneously recording MT sites to allow for better discrimination of signal and noise.

The RMEV approach uses the following model *Egbert* [1997]

$$\mathbf{X}_i = \begin{bmatrix} \mathbf{h}_{1i} \\ \mathbf{e}_{1i} \\ \vdots \\ \mathbf{h}_{Ji} \\ \mathbf{e}_{Ji} \end{bmatrix} = \mathbf{U}\mathbf{a}_i + \mathbf{V}\mathbf{b}_i + \epsilon_i = \mathbf{W}\mathbf{c}_\mathbf{i} + \epsilon_i. \tag{2.43}$$

The frequency domain MT array data vectors $\mathbf{X_i}$ are for a given frequency band and time segments $i = 1, \cdots, I$. Supposing there are J sites with 4 channels of data each (E_x, E_y, H_x and H_y), then X_i is composed of $K = 4J$ data channels ($\mathbf{h}$ and $\mathbf{e}$). The data channels are related to $K \times M$ signal vectors contained in $\mathbf{U}$ that span the response space [*Egbert and Booker*, 1989]. For the quasi-uniform plane-wave source field assumption in the MT method, $M = 2$ and the two columns of $\mathbf{U}$ give the total fields associated with two independent and time-varying source polarizations given in $\mathbf{a_i}$ (dimension 2×1). This model accounts for sources of coherent noise and non-uniform source effects with the matrix $\mathbf{V}$ and its polarization vector $\mathbf{b_i}$. The number of columns L of $\mathbf{V}$ is dictated by the number of coherent noise sources. The K dimensional incoherent noise vector ϵ allows for incoherent noise on each channel. The source field and coherent noise are combined into the matrix $\mathbf{W}$. The number of columns in $\mathbf{W}$, $N = M + L$, is known as the coherence dimension of the data [*Egbert*, 1997] and represents the linear combination of coherent signal and coherent noise vectors. With a suitable estimate of $\mathbf{W}$, the coherence dimension N can be found, allowing one to test if the data are free of coherent noise and compatible with the plane wave source field assumption (i.e. $N = 2$).

Estimation of $\mathbf{W}$ is accomplished by computing the eigenvector decomposition of the scaled spectral density matrix [*Egbert*, 1997]. Starting with the spectral density matrix (the matrix of all cross-product averages) $\mathbf{S}$

$$\mathbf{S} = \left\langle \mathbf{X}\mathbf{X}^\dagger \right\rangle = 1/I \sum_i \mathbf{X}\mathbf{X}^\dagger,$$

scaling $\mathbf{S}$ by the estimated incoherent noise diagonal covariance matrix $\mathbf{\Sigma}_N =$

$\mathbf{E}(\epsilon\epsilon^{\dagger})$, and taking an eigenvector decomposition yields

$$\mathbf{S}' = \mathbf{\Sigma}_N^{-\frac{1}{2}} \mathbf{S} \mathbf{\Sigma}_N^{-\frac{1}{2}} = \mathbf{W} \mathbf{\Lambda} \mathbf{W}^{\dagger}. \tag{2.44}$$

In Equation (2.44) $\mathbf{\Lambda}$ is a diagonal matrix of eigenvalues and the columns of $\mathbf{W}$ are the corresponding eigenvectors. The number of eigenvalues of $\mathbf{W}$ that are significantly larger than one provides an estimate of the coherence dimension N of the data [*Egbert*, 1997]. If $N = 2$ the data are compatible with the plane wave source model, while $N > 2$ suggests the presence of coherent noise or more complicated source fields. When $N = 2$, $\mathbf{U} = \mathbf{W}$ and the transfer tensor $\mathbf{T}$ between any pair of channels and all other channels in $\mathbf{X}$ can be computed by partitioning the matrix $\mathbf{U}$ into a 2×2 matrix $\mathbf{U_1}$ containing the single pair of channels and a $(K-2) \times 2$ matrix $\mathbf{U_2}$ containing all other channels, then taking the product

$$\mathbf{T} = \mathbf{U_2} {\mathbf{U_1}}^{-1}.$$

In this way impedance estimates can be calculated for each site, as well as all inter- and intra-station transfer functions. *Egbert* [1997] describes the details of a robust weighting scheme for the spectral denstiy matrix $\mathbf{S}$ and an iterative procedure for approximately unbiased estimates of the incoherent noise variances. Suggestions for decomposing $\mathbf{W}$ into $\mathbf{U}$ and $\mathbf{V}$ for the case when $N > 2$ are given in *Egbert* [1997; 2002].

Figure 2.11 shows an example of the SDM matrix eigenvalues computed from a subset of sites from the Gemini Prospect MT survey (Chapter 3). Five MT sites (20 channels of data) were used in the RMEV estimation scheme and eigenvalues were output for each frequency band. Over most of the period range there are only two dominant eigenvalues (solid lines), suggesting the data are compatible with the plane wave source field assumption and are free of coherent noise sources. At periods less than about 3 seconds the source field has become attenuated due to the overlying ocean layer and is no longer distinguishable from the background noise, as shown by the eigenvalues falling close to 0 dB. At periods

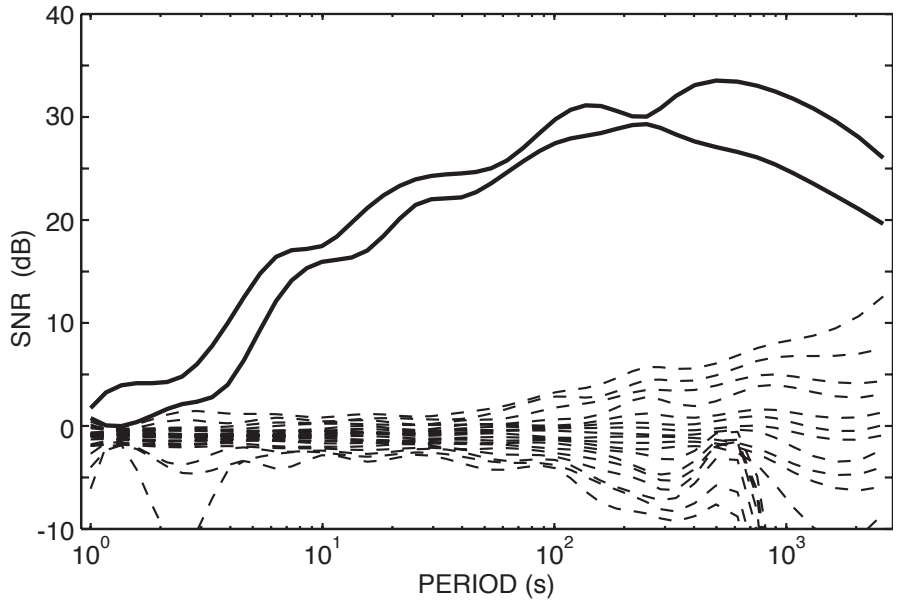

Figure 2.11: Example of an eigenvalue spectrum computed from 5 MT sites from the Gemini Prospect, Gulf of Mexico (Chapter 3).

greater than about 100 s more eigenvalues rise above the estimated incoherent noise level (the eigenvalues have been normalized by the incoherent noise level, so 0 dB corresponds to the incoherent noise level) and suggest other sources of signal in the MT data, however, they are still much smaller than the 2 dominant eigenvalues.

2.5 Seafloor Orientations of MT Instruments

Prior to 2003, the broadband marine MT instruments utilized locking mechanical compasses to determine the orientation of the electric and magnetic field sensors on the seafloor. These have now been replaced with electronic compasses. Neither system is fail-proof; the locking mechanical compasses sometimes do not properly lock and the electronic compasses can be severely biased if the data logger batteries or disk drive are DC magnetized. In such situations an instrument's seafloor orientation can be estimated by examining the inter-station

transfer functions between MT sites. Over a given frequency band, the magnetic field $\mathbf{H_1}$ (and similarly $\mathbf{E_1}$) at a site can be related to the field $\mathbf{H_2}$ at another site with a 2×2 transfer tensor $\mathbf{T}$

$$\mathbf{H}_1 = \mathbf{T}\,\mathbf{H}_2 = \begin{bmatrix} H_{x1} \\ H_{y1} \end{bmatrix} = \begin{bmatrix} T_{xx} & T_{xy} \\ T_{yx} & T_{yy} \end{bmatrix} \begin{bmatrix} H_{x2} \\ H_{y2} \end{bmatrix}. \tag{2.45}$$

Provided that local 3D inductive and galvanic effects are small at both sites, the diagonal elements of $\mathbf{T}$ will be at a maximum and the off-diagonal elements will reach a minimum when the x-axis of both instruments are aligned. Thus, the relative angle of one site from another, θ, (positive clockwise) can be determined by rotating the transfer tensor until the magnitude of the diagonal terms reaches a maximum and the off-diagonals reach a minimum. To resolve the 180° ambiguity, the positivity of both T_{xx} and T_{yy} is required. In practice this technique is accomplished by taking the matrix of all intra- and inter-station transfer functions $\mathbf{U}$ output by the multi-station processing code [*Egbert*, 1997] (see Section 2.4.5), extracting the sub-matrices of each frequency's transfer tensor that correspond to the two sites of interest, and rotating the transfer tensor incrementally over 180° to find the angle that maximizes $|diag(\mathbf{T}')|$

$$\mathbf{T}' = \mathbf{R}^T\,\mathbf{T}\,\mathbf{R}, \tag{2.46}$$

where $\mathbf{R}$ is the rotation matrix

$$\mathbf{R} = \begin{bmatrix} \cos\theta & \sin\theta \\ -\sin\theta & \cos\theta \end{bmatrix}. \tag{2.47}$$

An example using the magnetic fields of two MT sites from the Gulf of Mexico MT survey at Gemini Prospect (Chapter 3) is shown in Figure 2.12. The scatter in the relative angle between the two instruments is about ±2.5°, which is representative of the results obtained from typical data. The transfer tensor between electric fields can also be used and yields the same relative angle provided that local inductive effects are minimal at both sites. To determine the absolute orientation, two

different procedures can be used. The first method is to calculate the relative orientations between one reference site and all other sites of a survey using the transfer tensor method. Then relative angles between the sites are compared with relative angles determined from the compass data to figure out which compasses are consistent with the transfer tensor method. Absolute orientations can then be found for the remaining instruments by applying the transfer tensor relative orientations to the absolute compass orientations for the known sites. Another method is to compute the transfer function between a land remote site with known sensor orientations and the seafloor sites to yield the absolute orientation of the seafloor sensors. This technique was applied to early data in collected in 1996, 1997 and 1998 in the Gulf of Mexico and yields orientations consistent with using the first method, and also agrees with the mechanical compass orientations. One caution of this method is that the remote must be sufficiently close so that the source field is at least approximately quasi-uniform between the survey area and the remote site.

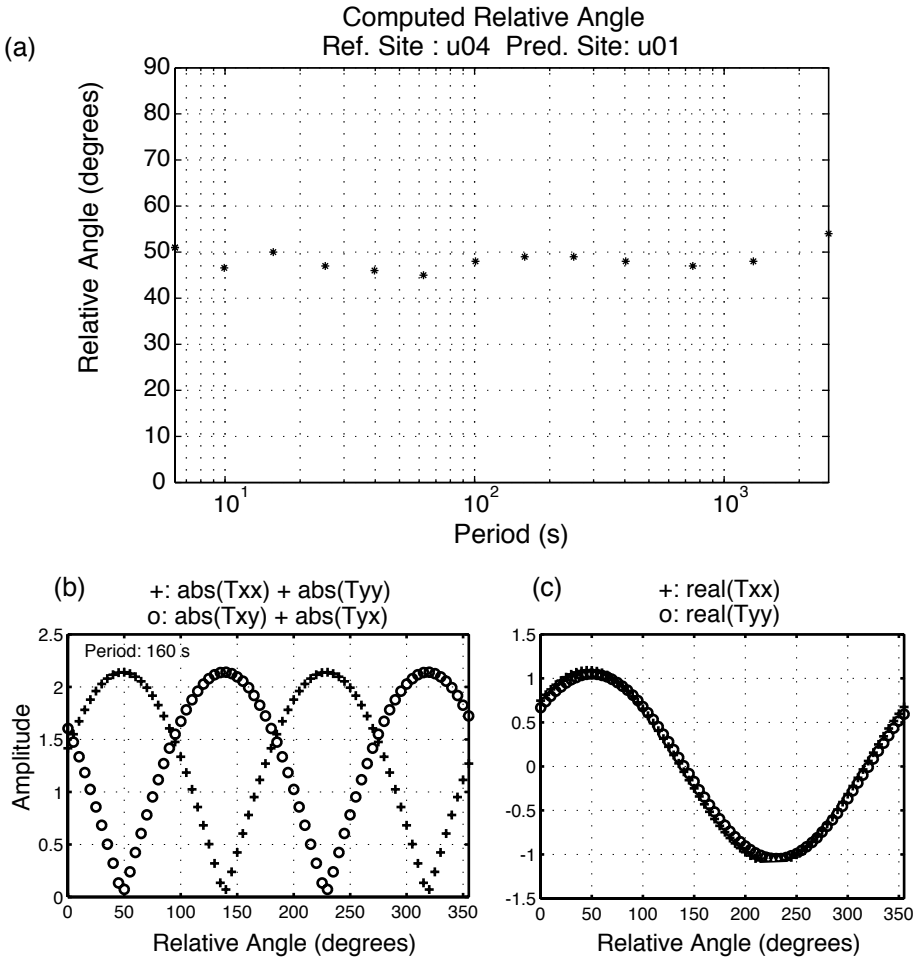

Figure 2.12: Example of rotating magnetic transfer tensor to determine the relative instrument orientation angle. (a) The best fit relative angle between two seafloor MT sites from the Gulf of Mexico plotted for each frequency band. The relative angle lies between 45-50° and maximizes $|T_{xx}| + |T_{yy}|$ while $|T_{xy}| + |T_{yx}|$ go to zero, as shown in (b). The 180° ambiguity shown in (b) is resolved by requiring that the real parts of T_{xx} and T_{yy} are positive as shown in (c).

References

Baba, K., and N. Seama, New technique for the incorporation of seafloor topography in electromagnetic modelling, *Geophys. J. Int.*, *150*, 392–420, 2002.

Chave, A. D., and D. J. Thomson, Some comments on magnetotelluric response function estimation, *J. Geophys. Res.*, *94*, 14,215–14,225, 1989.

Chave, A. D., S. C. Constable, and R. N. Edwards, Electrical exploration methods for the seafloor, in *Electromagnetic methods in applied geophysics*, edited by M. N. Nabighian, 02 ed., pp. 931–969, Soc. Expl. Geophys., 1991.

Constable, C., and S. Constable, Satellite magnetic field measurements: applications in studying the deep earth, in *State of the Planet: Frontiers and Challenges*, edited by C. J. Hawkesworth and R. S. J. Sparks, AGU Monograph, submitted, 2003.

Constable, S. C., A. S. Orange, G. M. Hoversten, and H. F. Morrison, Marine magnetotellurics for petroleum exploration Part I: A sea-floor equipment system, *Geophysics*, *63*, 816–825, 1998.

Egbert, G., and J. Booker, Robust estimation of geomagnetic transfer functions, *Geophys. J. R. astr. Soc.*, *87*, 173–194, 1986.

Egbert, G. D., Robust multiple-station magnetotelluric data processing, *Geophys. J. Int.*, *130*, 475–496, 1997.

Egbert, G. D., Processing and interpretation of electromagnetic induction array data, *Surveys in Geophysics*, *23*, 207–249, 2002.

Egbert, G. D., and J. R. Booker, Multivariate analysis of geomagnetic array data 1, The response space, *J. Geophys. Res.*, *94*, 14,227–14,248, 1989.

Filloux, J. H., North Pacific magnetotelluric experiments, *J. Geomag. Geoelectr.*, *32*, 33–43, 1980.

Gamble, T. D., W. M. Goubau, and J. Clarke, Magnetotellurics with a remote reference, *Geophysics*, *44*, 53–68, 1979.

Heinson, G., , and S. Constable, The electrical conductivity of the oceanic upper mantle, *Geophys. J. Int.*, *110*, 159–179, 1992.

Heinson, G. S., A. White, L. K. Law, Y. Hamano, H. Utada, T. Yukutake, J. Segawa, and H. Toh, EMRIDGE: The electromagnetic investigation of the Juan de Fuca Ridge, *Marine Geophys. Res.*, *15*, 77–100, 1993.

Hoversten, G. M., H. F. Morrison, and S. C. Constable, Marine magnetotellurics for petroleum exploration, Part II: Numerical analysis of subsalt resolution, *Geophysics*, *63*, 826–840, 1998.

Key, K., and S. Constable, A light-weight and low-power marine induction coil magnetometer, in preparation.

McKirdy, D. M., J. T. Weaver, and T. W. Dawson, Induction in a thin sheet of variable conductance at the surface of a stratified earth -II. Three-dimensional theory, *Geophys. J. R. astr. Soc.*, *80*, 177–194, 1985.

Nichols, E. A., H. F. Morrison, and J. Clarke, Signals and noise in measurements of low-frequency geomagnetic fields, *J. Geophys. Res.*, *93*, 13,794–13,754, 1988.

Nolasco, R., P. Tarits, J. H. Filloux, and A. D. Chave, Magnetotelluric imaging of the Society Islands hotspot, *J. Geophys. Res.*, *103*, 30,287–30,309, 1998.

Ranganayaki, R. P., and T. R. Madden, Generalized thin sheet analysis of magnetotellurics - An extension of Price' analysis, in *Magnetotelluric methods*, edited by K. Vozoff, pp. 344–356, Soc. Expl. Geophys., 1986, reprinted from Geophysical Journal of the Royal Astronomical Society, 60, 445-457.

Schmucker, U., Anomalies of geomagnetic variations in the southwestern United States, *Bull. Scripps Inst. Oceanogr.*, *13*, 1–170, 1970.

Sims, W. E., F. X. J. Bostick, and H. W. Smith, The estimation of magnetotelluric tensor elements from measured data, in *Magnetotelluric methods*, edited by K. Vozoff, pp. 167–171, Soc. Expl. Geophys., 1986, reprinted from Geophysics, 36, 938-942.

Swift, C. M. J., A magnetotelluric investigation of an electrical conductivity anomaly in the southwestern United States, in *Magnetotelluric methods*, edited by K. Vozoff, pp. 156–166, Soc. Expl. Geophys., 1986, not previously published.

Thomson, D. J., Spectrum estimation and harmonic analysis, *Proceedings of the IEEE*, *70*, 1055–96, 1982.

Vasseur, G., and P. Weidelt, Bimodal electromagnetic induction in non-uniform thin sheets with an application to northern Pyrenean induction anomaly, *Geophys. J. R. astr. Soc.*, *51*, 669–690, 1977.

Vozoff, K., The magnetotelluric method, in *Electromagnetic methods in applied geophysics*, edited by M. N. Nabighian, 02 ed., pp. 641–711, Soc. Expl. Geophys., 1991.

Wannamaker, P. E., J. A. Stodt, and L. Rijo, A stable finite-element solution for two-dimensional magnetotelluric modeling, *Geophys. J. R. astr. Soc.*, *88*, 277–296, 1987.

Ward, S. H., and G. W. Hohmann, Electromagnetic theory for geophysical applications, in *Electromagnetic methods in applied geophysics*, edited by M. N. Nabighian, 01 ed., pp. 131–312, Soc. Expl. Geophys., 1988.

Webb, S. C., S. C. Constable, C. S. Cox, and T. Deaton, A seafloor electric field instrument, *J. Geomag. Geoelectr.*, *37*, 1115–1130, 1985.

Wight, D. E., and F. X. Bostick, Cascade decimation - A technique for real time estimation of power spectra, in *Magnetotelluric methods*, edited by K. Vozoff, pp. 215–218, Soc. Expl. Geophys., 1986, reprinted from 1980 Proceedings IEEE International Conference on Acoustic Speech and Signal Processing, 626-629.

Chapter 3

Mapping 3D Salt with 2D Marine MT: Case Study from Gemini Prospect, Gulf of Mexico

Abstract

Gemini Prospect, Gulf of Mexico (GOM) has served as the test bed site for the continual development of the Scripps Institution of Oceanography broadband marine magnetotelluric (MT) instrument. The Gemini salt body lies 1-5 km beneath the seafloor in 1 km deep water and has a high electrical resistivity compared with the surrounding sediments, making it a suitable target for electrical methods. We have collected 42 sites of MT data in the period band of 1-3000 seconds in a two-dimensional (2D) grid over the Gemini salt body, making our data excellent for developing and testing 2D and three-dimensional (3D) modeling techniques.

We present 2D inversion models obtained from inverting subsets of the Gemini MT data, along with a comparison to the Gemini salt volume boundaries obtained from high resolution 3D seismic data. While some of the 2D inversion models recover the salt boundaries remarkably well despite the complex 3D shape of the Gemini salt body, the results are heavily dependent on inverting the correct

mode of data. Our experience suggests that inverting the mode with the electric field perpendicular to the dominant structural strike yields the best agreement with the seismically determined structure. Synthetic 2D inversions of the 3D MT forward response of the salt volume are used to validate the observed mode sensitivities. An improved structural interpretation is found through the joint analysis of the combined depth migrated seismic reflection and electrical resistivity models. A thin and shallow resistive feature outside the seismic salt structure in one MT inversion model correlates with seismic reflection layers and may indicate a change in porosity or pore fluids. An overhanging resistive feature in another MT inversion model correlates with a previously uninterpreted seismic reflection and illustrates how MT can provide structural constraints in areas where seismic methods perform poorly.

3.1 Introduction

Allochthonous salt structures such as those in the offshore northern Gulf of Mexico (GOM) region [e.g. *Schuster*, 1995; *Diegel et al.*, 1995; *Peel et al.*, 1995] play an important role in the deformation of sediments and subsequent formation of hydrocarbon reserves. Knowledge of the shape and extent of salt structures and their tectonic history is important in exploiting petroleum reserves trapped subsalt (i.e. beneath the salt). Reflection seismology, the primary technique for imaging both salt structures and the surrounding sediments, can provide detailed images of both top and base-of-salt surfaces, sedimentary layers, fault scarps and basement formations. This level of detail can be used to infer where sediment layers have been deformed or juxtaposed to form potential traps for hydrocarbons. However, there are many situations where reflection data do not provide sufficient detail of salt structures, resulting in interpretational ambiguities. Common problems include multiple reflections and mode conversions [e.g. *Ogilive and Purnell*, 1996], the loss of reflected energy from steeply dipping salt surfaces, and the lack of co-

herent features beneath salt structures. These complications motivated research of another, complementary, technique for mapping salt structures–the marine magnetotelluric (MT) method. The large resistivity contrast between resistive salt and relatively conductive porous sediments makes salt structures a suitable target for the MT method. While MT has been used effectively on land for petroleum exploration [e.g. *Vozoff*, 1972], early marine work was confined to very shallow water and of limited use due to bulky equipment and wave noise [*Hoehn and Warner*, 1986]. More recently, numerical model studies showed that marine MT data in the period band of about 1-1000 seconds are sensitive to salt geometry and can distinguish between shallow and deeply rooted salt structures [*Hoversten et al.*, 1998]. The amplitudes of such short period electric and magnetic fields lies below the sensitivity threshold of traditional academic marine MT instruments, which were designed to be sensitive to the stronger amplitude fields at periods greater than about 500 seconds [e.g. *Filloux*, 1980]. The recent introduction of a new breed of instrumentation–the broadband marine MT instrument–allows for measurement of both electric and magnetic fields in the period range of 0.1-10,000 seconds [*Constable et al.*, 1998]. The broadband instrument obtains such a bandwidth through the combined usage of ac-coupled sensors and low-noise amplifiers, which enable measurement of the smaller electric and magnetic field variations present at these short periods.

In this paper we investigate the effectiveness of using two-dimensional (2D) marine MT to map three-dimensional (3D) salt structures by presenting a case study of 42 sites of MT data collected at the subsalt discovery at Gemini Prospect in the northern GOM. Top and base-of-salt surfaces of the Gemini salt structure provided by an industry 3D seismic survey allow us to test how well MT can map out the resistive salt structure. We use regularized 2D inversion to model transects of data and present comparisons with the top and base-of-salt boundaries obtained from a 3D seismic survey. Synthetic 2D MT inversions of 3D forward MT responses of the seismic salt model are compared to the real data

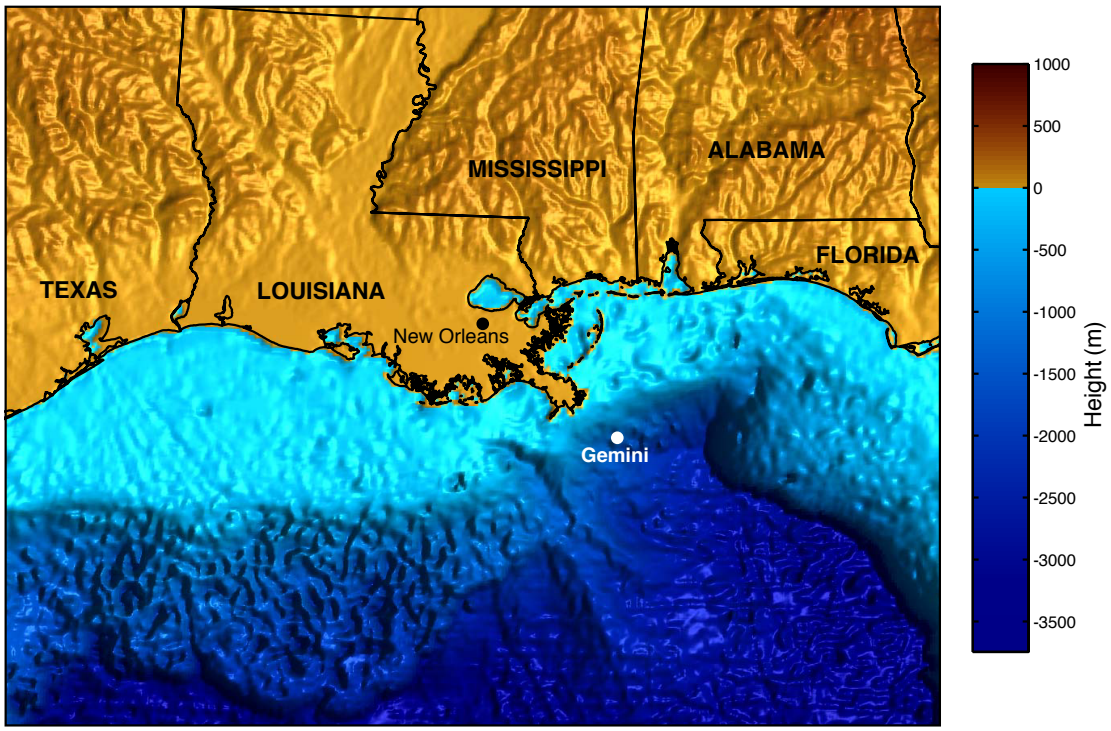

Figure 3.1: Location of Gemini Prospect in the northern Gulf of Mexico. Topography and bathymetry from *Smith and Sandwell* [1997].

inversions to assess model consistency and mode sensitivities in the 2D inversions. Finally, we show the improved interpretation possible by using both seismic and MT data in a combined image of depth migrated seismic reflection and inverted resistivity.

3.2 Gemini Prospect Salt Structure

Gemini Prospect lies about 200 km south-east of New Orleans in about 1 km deep water in the northern Gulf of Mexico (Figure 3.1). The Gemini salt structure is part of a roho system (described below) that is about 16-24 km wide and 72 km long (Figure 3.2). An interpretation of this system's tectonic history is given in *Schuster* [1995] and reviewed below. The salt originated as part of the autochthonous Louann salt that was extensively deposited over the northern

Gulf of Mexico during the Upper Jurassic as a post-rifting response to the Middle Jurassic opening of the Gulf of Mexico [*Peel et al.*, 1995]. In the Middle-late Miocene, sedimentation and differential loading led to the salt viscously flowing up to the seafloor through feeders and leaving behind a deflated residual thickness of autochthonous Louann salt [*Fletcher et al.*, 1995; *Schuster*, 1995]. At the seafloor a thin veneer of pelagic sediments covered the allochthonous salt and acted as a barrier to dissolution, allowing the salt to spread out laterally as a thin *salt glacier* [*Fletcher et al.*, 1995; *Schuster*, 1995]. By the late Miocene differential loading of the salt glacier by deltaic sediments led to up-dip (north-west to south-east) extension and the formation of major basin-ward listric growth faults that sole out at the base of the salt glacier, forming a *roho* system [*Schuster*, 1995]. Continual loading that lasted into the Pleistocene resulted in salt evacuation and basin-ward translation [*Schuster*, 1995]. As can be seen from Figure 3.2, Gemini lies on the eastern flank of the roho system where salt has been forced out both basinward and laterally, resulting in a complex 3D structure. Many of the features shown in Figure 3.2, such as faults and salt regions, are also evident as surface features shown in the bathymetry of Figure 3.3. The subsalt prospect at Gemini consists of a gas sand located at depths of about 4 km on the south-eastern edge of the Gemini salt structure [*Ogilive and Purnell*, 1996].

Top and base-of-salt surfaces from a commercial 3D seismic reflection survey illustrate the complex 3D shape of the salt structure (Figures 3.4-3.6). Most of the salt lies between about 2-5 km beneath the seafloor. The top-of-salt surface has a predominant north-west to south-east structural strike. In the region of the MT survey the base-of-salt surface has a basin-like shape with depths in excess of 6 km to the north-west. This deep portion of the base-of-salt is less well constrained, as the base-of-salt seismic reflections disappear here. There is some ambiguity as to whether the salt continues down to the evacuated Louann salt source layer as a feeder stock or if the salt merely bottoms out at depths around 6 km. Based on the lack of coherent reflections *Schuster* [1995] interprets this

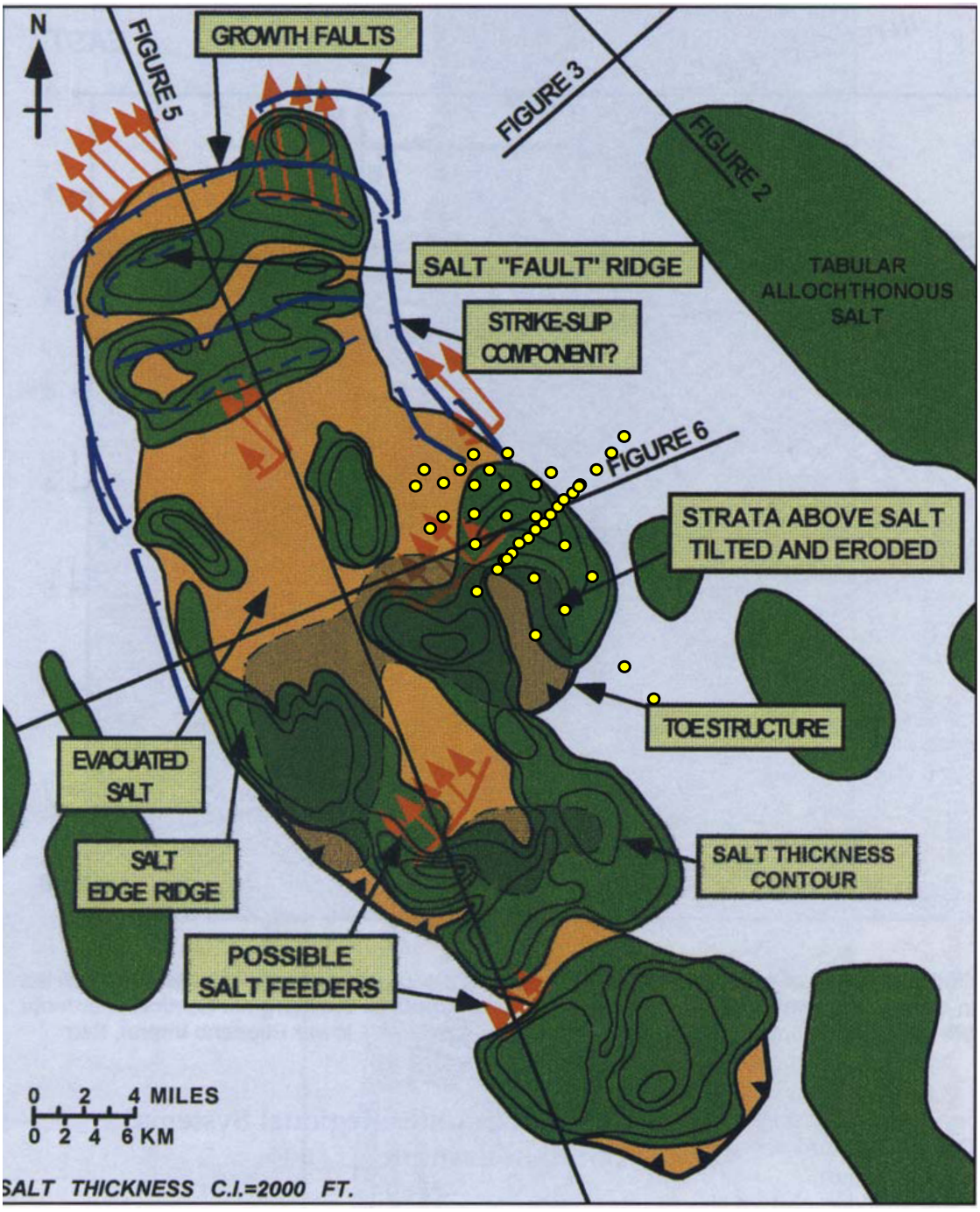

Figure 3.2: Regional isopach (salt thickness) map near Gemini Prospect, Gulf of Mexico (from *Schuster* [1995], Figure 7). Yellow circles show the locations of the MT sites at Gemini Prospect. Green regions show the location of salt structures and black lines show salt thickness contours. Evacuated salt surfaces are shown as orange regions. Blue lines show the seafloor location of growth faults. Orange arrows show possible salt roots (also termed feeders).

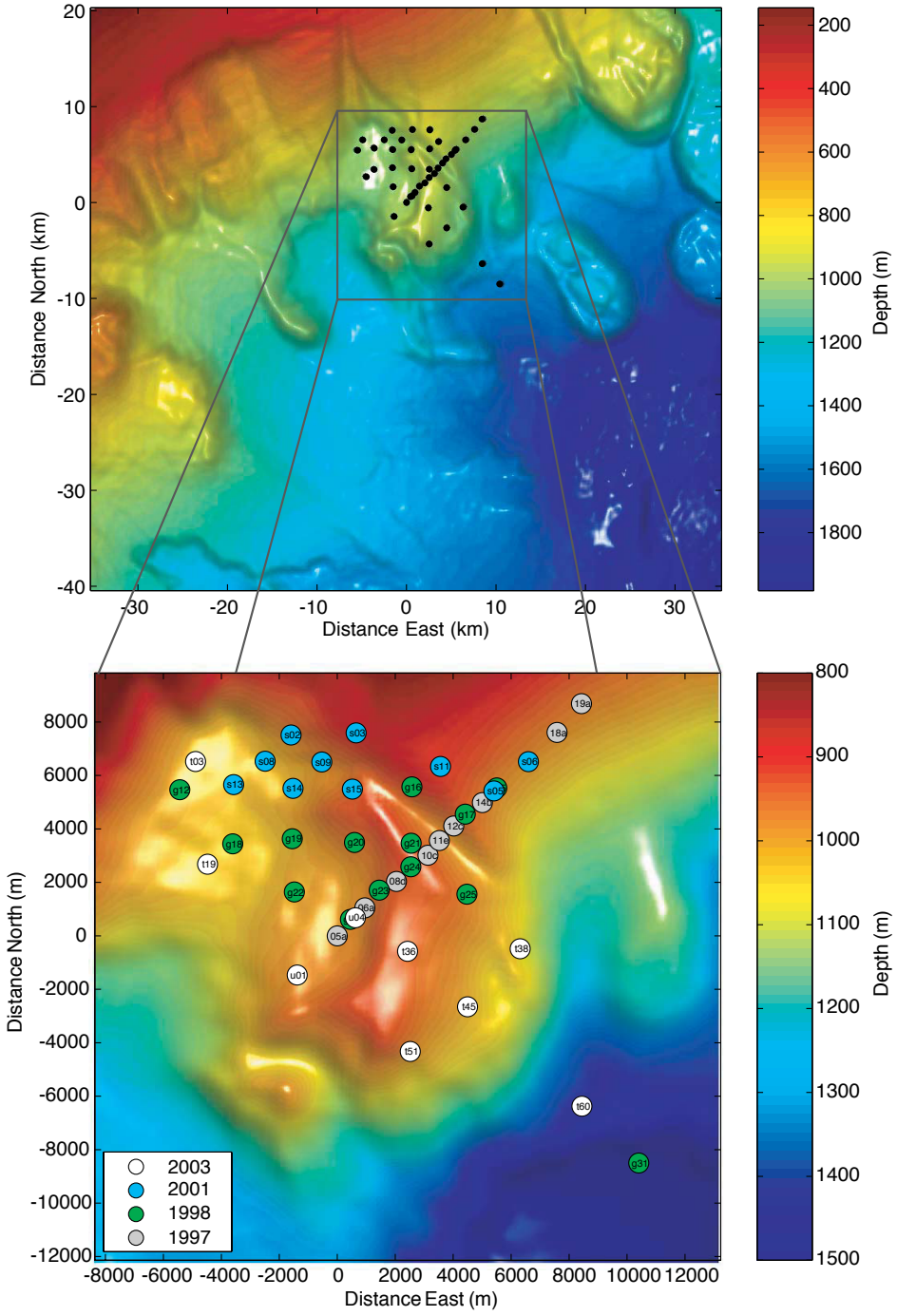

Figure 3.3: Bathymetry and MT site locations at Gemini Prospect. MT sites are shown as circles with the color indicating the year the site was acquired.

region as a *possible* salt feeder (orange arrows in Figure 3.2).

3.3 MT Surveys

Gemini has been the test-bed site for testing the ability of marine MT to map resistive salt structures [*Hoversten et al.*, 2000] and for the continual development of the Scripps Institution of Oceanography broadband marine MT instrument [*Constable et al.*, 1998]. Test deployments in the years 1997, 1998, 2001 and 2003 have resulted in 42 sites of MT data in the period band 1-3000 seconds (Figures 3.3-3.6). Two-dimensional inversion of the 9 sites collected in 1997 showed that even with only a few sites of data MT can recover the base of salt to within 5-10% of burial depth [*Hoversten et al.*, 2000]. While this result was received as a success for the method, the line of 1997 data is most amenable to 2D modeling (as evident in the predominantly 2D strike of the top-of-salt surface, see Figure 3.4) and leaves some doubt as to whether the method can handle more complicated structural geometries. To broaden the test of marine MT's ability to detect resistive salt, the following year's deployments were spread out across a wider region of the salt structure. In this paper we expand the 2D analysis to include all 42 sites of data. Many of these 2D transects are over highly 3D regions of the salt structure and thus provide a suitable test for assessing the capabilities of using of 2D marine MT to image 3D salt.

3.4 Data Processing

During each survey, time series of the horizontal electric and magnetic fields were collected simultaneously at several sites for about 1-2 days. The simultaneous recording of data at many sites allowed impedance tensor estimates to be calculated using a robust, multiple station transfer function estimation routine [*Egbert*, 1997]. Experience with this routine has shown that a land remote reference MT station is not required, and so land remote reference stations were no

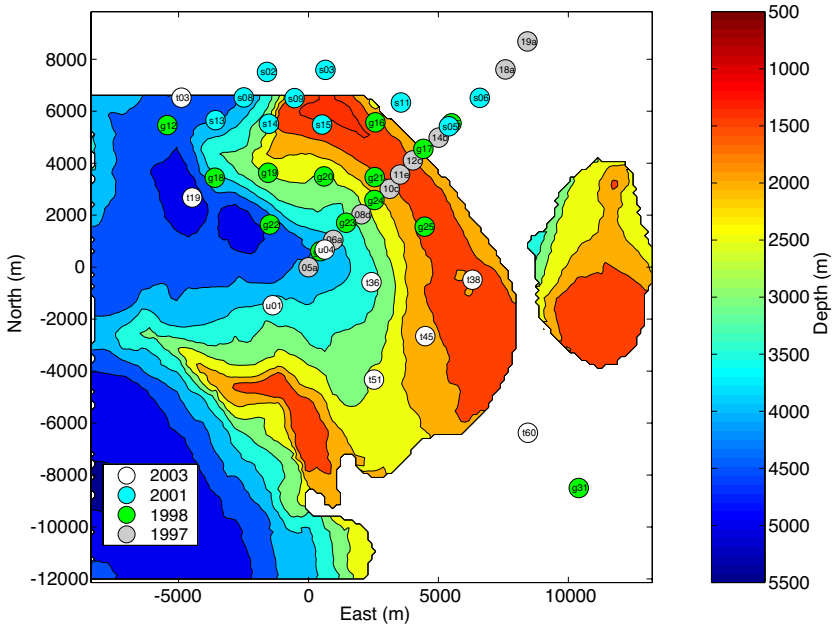

Figure 3.4: Top-of-salt depth map from 3D seismic data and MT site locations. Depths are relative to sea surface.

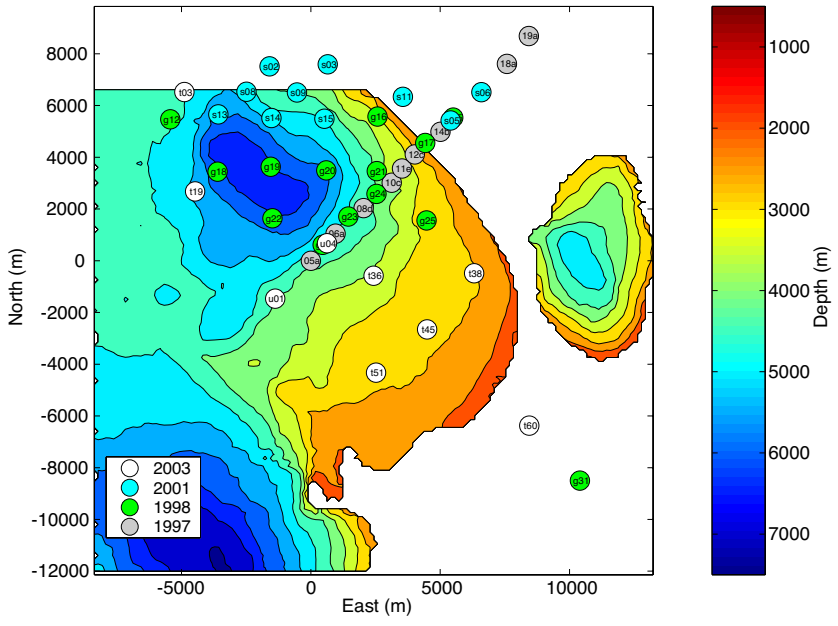

Figure 3.5: Base-of-salt depth map from 3D seismic data and MT site locations.

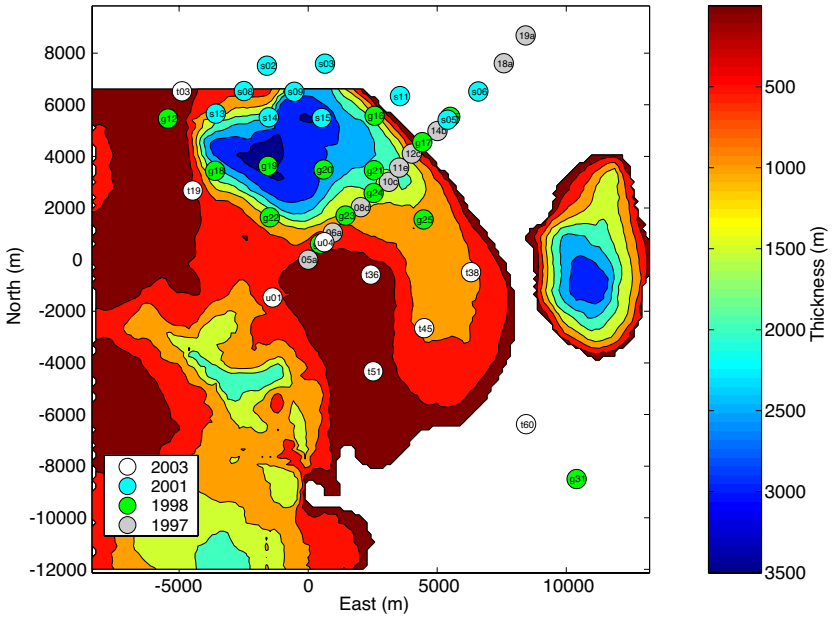

Figure 3.6: Salt isopach map from 3D seismic data and MT site locations.

longer occupied after the 1998 survey. Impedance tensor estimates were calculated for each site over the period band of 1-3000 s. Seafloor orientation of the sensors was determined through a combination of locking mechanical compass readings from each deployment and analysis of inter-station transfer tensors between both electric and magnetic fields. MT responses for each site are shown in Appendix A.

Data quality is variable between the different survey years and sites for several reasons. Deployments at Gemini were usually done as a shake-down of new instrument modifications before use on commercial surveys, and so inevitable problems were often discovered and fixed from these "test" deployments. For example, electric and magnetic fields were recorded on separate instruments during the 1997 survey due to noise problems associated with the data logger power consumption and instrument motional noise. The magnetic field instruments were outfitted with 200 kg concrete "sea-slabs" for anchors, which greatly stabilized the instrument on the seafloor and resulted in improved data quality. After fixing instrumental noise and utilizing the concrete anchors, subsequent surveys recorded both electric and magnetic fields on one instrument. Source field strength variations also affected

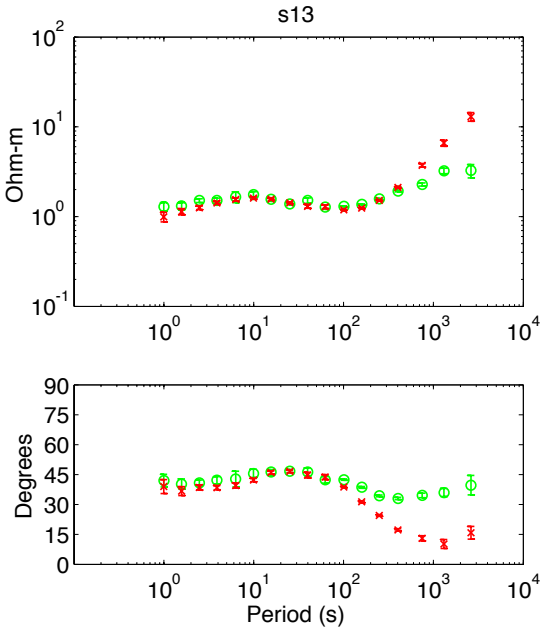

Figure 3.7: Example of high quality marine MT apparent resistivity and phase data from site 13. Red symbols are for the impedance component with the electric field oriented to the south-east and green symbols are for the electric field oriented to the north-east.

data quality. A large magnetic storm occurred during the spring 2001 survey and resulted in high quality data for all deployments. Conversely, shipboard problems during the 2003 survey resulted in short deployments that occurred coincident with a period of relatively low source field strength, yielding good data only in the period band of 10-1000 seconds. At short periods where the overlying seawater greatly attenuates the MT source field [e.g. *Constable et al.*, 1998], variations in source field strength resulted in some surveys acquiring data to periods as short as 1 s, while others yielded data good only to periods as short as 10 s.

An example of high quality marine MT data is shown in Figure 3.7. This site is located over the thick and deep portion of the salt structure (Figure 3.5). The slight increase in apparent resistivity centered around 10 s period is an example of the very small resistive MT response for sites located over the salt structure. Salt is very resistive (> 10 Ωm) when compared to seawater (0.3 Ωm)

and seawater saturated sediments like those found at Gemini (around 0.5 Ωm). Unlike the case of conductive targets that can generate large secondary fields and strong MT responses, the resistive salt forces induced currents to flow around it rather than through it and yields only minor secondary fields and very small MT responses. The MT response effectively saturates after the first factor of 10 or so in resistivity, and results in the seafloor impedances being more sensitive to the shape of the salt body rather than the resistance.

3.5 Modeling

The modeling section of this study consisted of two components. For the first part, two-dimensional regularized inversions were performed for the transect lines shown in Figure 3.8. Many of the inversion models showed large differences in structure when different modes of the data were inverted and so a second modeling component using a combination of three-dimensional forward and two-dimensional inverse modeling was done to address this disparity in component sensitivities.

3.5.1 Two-Dimensional Inversion

Apparent resistivity and phase data from each of the MT transects shown in Figure 3.8 were modeled using the regularized 2D MT inversion OCCAM2DMT [*Constable et al.*, 1987; *de Groot-Hedlin and Constable*, 1990]. Any given set of MT measurements is finite and imprecise and so an infinite number of solutions to the inverse problem exist. The approach used here and in most other geophysical inversion schemes is to restrict the set of solutions to those that meet some a priori criteria or regularization constraints. In the case of OCCAM2DMT, the inversion seeks to find a model that both fits the data and has smoothly varying parameters. While the *real* Earth may have sharply varying structures, the MT method is generally not sensitive enough to unambiguously resolve sharp versus smooth boundaries. In regions where the MT data are not sensitive to structure,

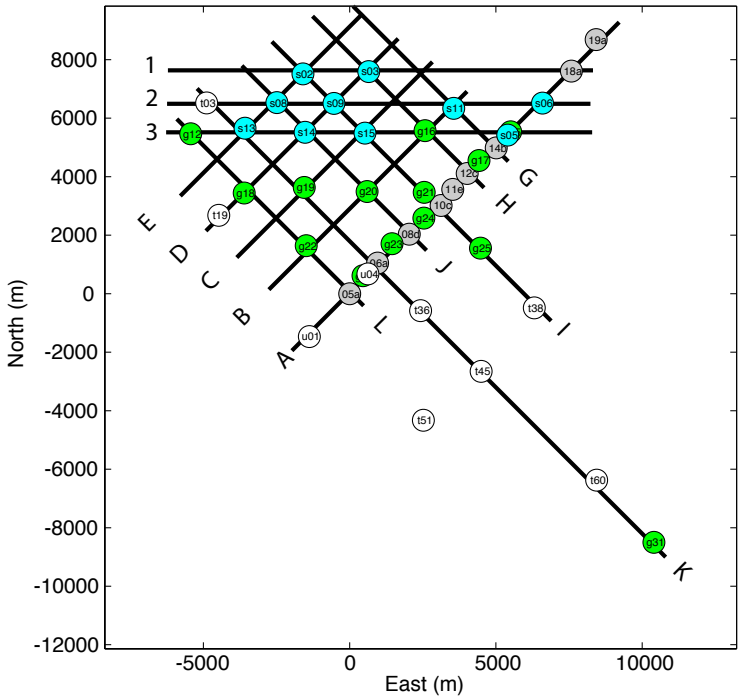

Figure 3.8: Map showing the profiles used in the 2D inversions.

the inversion models will have little structural variation. Since smooth inversions such as OCCAM2DMT only output structures required by the data, they are often referred to as as minimum structure inversions. Thus, a structure not sensed by the data will not be imaged in the inversion models. In addition to limiting the class of acceptable models, the smoothness requirement also acts to stabilize the inversion and increase the convergence rate. The general approach is outlined below, starting with a statement of the solution to the forward problem

$$\mathbf{d} = \mathbf{F}[\mathbf{m}],$$

where $\mathbf{d}$ is a vector of apparent resistivity and phase data and $\mathbf{F}$ is the forward operator that computes the MT response for a given set of model parameters (i.e. resistivities) $\mathbf{m}$. The inversion approach uses a Lagrange multiplier formulation and seeks to minimize the following unconstrained functional

$$\mathrm{U}[\mathbf{m}] = \|\boldsymbol{\partial}\mathbf{m}\|^2 + \mu^{-1}\left\{\|\mathbf{W}\mathbf{d} - \mathbf{W}\mathbf{F}[\mathbf{m}]\|^2 - X_*^2\right\}, \tag{3.1}$$

where $\| \cdot \|$ denotes the Euclidean or L_2 norm, $\boldsymbol{\partial}$ is a roughening matrix which acts to first difference adjacent model parameters, μ^{-1} is the Lagrange multiplier, $\mathbf{W}$ is a diagonal matrix of weights determined from the uncertainty of each data point, and X^2_* is the acceptable level of data misfit. The first term on the right is a measure of the model roughness. Minimizing this term limits the amount of model roughness, or conversely increases the model smoothness. The second term on the right determines how well the model fits the data. The Lagrange multiplier acts as a weighting term that is adjusted to strike a balance between minimizing the data misfit and minimizing the model roughness. Details of the iterative minimization of equation 3.1 can be found in *Constable et al.* [1987] and *de Groot-Hedlin and Constable* [1990]. The forward operator $\mathbf{F}$ is calculated using a standard 2D MT finite element modeling program [*Wannamaker et al.*, 1987]. The data vector $\mathbf{d}$ is comprised of the logarithm of the apparent resistivity and complex phase data from each site. For the first iteration, the model vector $\mathbf{m}$ consists of a uniform half-space resistivity value. Each iteration acts to refine $\mathbf{m}$ until an acceptable misfit to the data is found.

Before proceeding with the results of the 2D inversions, some details of the MT impedance must be discussed. The magnetotelluric impedance tensor $\mathbf{Z}$ relates the frequency dependent horizontal magnetic field vector $\mathbf{H}$ to the horizontal electric field vector $\mathbf{E}$ as

$$\mathbf{E} = \mathbf{ZH}$$

or

$$\begin{pmatrix} E_x \\ E_y \end{pmatrix} = \begin{pmatrix} Z_{xx} & Z_{xy} \\ Z_{yx} & Z_{yy} \end{pmatrix} \begin{pmatrix} H_x \\ H_y \end{pmatrix}.$$

For 1D structure, the off-diagonal components of $\mathbf{Z}$, which relate orthogonal components of the electric and magnetic fields, will be non-zero and equal to each other. The diagonal components, which relate parallel components of the electric and magnetic fields, will be zero for any rotation of the tensor. For 2D structure

the diagonal components will be zero when the tensor is rotated to the structural strike direction and the off-diagonal components will not be equal. For three dimensional structure the diagonal components Z_{xx} and Z_{yy} will not be zero for any rotation. Despite the complicated 3D geometry of the salt structure, the Gemini MT data have impedances that are mostly 1D with diagonal components very nearly zero in comparison to the off-diagonal components. At sites directly over the salt the impedances become slightly 2D at periods greater than about 10 seconds [see *Hoversten et al.*, 2000]. The lack of 3D impedances for such a 3D shaped structure is due in part to the physics of electromagnetic induction for a resistive rather than a conductive body. The salt resistivity is at least an order of magnitude greater than the surrounding sediments and induced currents in the sediments are occluded from the salt body and flow around the salt. Unlike a conductive target that can generate large secondary fields, very little induction occurs within the salt and there are no substantial secondary fields generated from within the salt body. Because very little current flows through the salt, charge build up on the salt boundaries is minimal. Instead the secondary field, or "salt signal," arises from small gradients in the primary fields as they bend around the salt body, resulting in a very small seafloor MT response from the salt that looks primarily 1D. Such a response is then more sensitive to the geometry rather than the resistivity of the salt.

In purely 2D modeling, two independent modes of data exist. In the transverse electric (TE) mode, the electric field E_x is oriented along the structural strike x and is orthogonal to the two auxiliary magnetic fields H_y and H_z. For the transverse magnetic (TM) mode, the magnetic field H_x is oriented along x and has accompanying E_y and E_z fields. The TE mode then corresponds to the Z_{xy} impedance and the TM mode the Z_{yx} impedance. Each mode has slightly different structural sensitivity from the field geometry and inversions can include either mode alone, or include both modes to increase the constraints on structure. In the presence of three-dimensional structure, assignment of TE and TM modes becomes

vague as structural strike is no longer clearly defined. Further references to TE and TM in this paper will adopt the convention of quasi-TE and quasi-TM modes in which the mode assignment refers to the field oriented in the direction orthogonal to the MT transect azimuth. For instance, Line A in Figure 3.8 is oriented at an azimuth of 45°, so the TE mode would correspond to the Z_{xy} impedance when $\mathbf{Z}$ is rotated so that x is at a 315° azimuth. In other words the TE mode has E_x oriented at 315°. While other principal directions could be used for the 2D modeling, we chose the line azimuth directions in order to minimize the number of 2D modeling assumptions violated to being only that the true structure is 3D instead of 2D. If some other intermediate principal directions were used the 2D model would then theoretically be equivalent to a projection of the MT sites onto a line perpendicular (or parallel) to the principal direction. Thus, the model would correspond to a model along the projection line, not the MT transect. This could present some difficulty since other sites, specifically those not along the original transect, might be more ideal to use on the projected transect.

Numerical modeling studies of salt structures [*Hoversten et al.*, 1998] showed that 2D inversions of 3D data are most accurate if only the TM mode is inverted and that 3D structures need only have aspect rations (length to width ratios) of greater than 2:1 to yield accurate TM inversion results. Thus, prior to inverting the Gemini data it was thought that TM mode inversions would yield the best agreement with the seismically determined salt structure. To test this result and to explore the sensitivity of the data to different parts of the Gemini structure, separate inversions of each mode were performed. Each inversion used a model consisting of about 2200 unknown model parameters. Data for each inversion consisted of 13 periods from 1 to 250 s for each site. Data at periods greater than 250 s were not included in the inversions for two reasons. First, the expected "salt" signal in the MT responses is small and many of the MT sites have very noisy responses at longer periods, so 250 s was chosen as a suitable cut-off period for including as much data as possible while minimizing the amount of noisy

data used. Additionally, numerical modeling of the distorting effects of nearby bathymetry (see Chapter 2) shows that a 5-10% distortion in the MT responses is seen at periods greater than about 300 s for a slope that is representative of the bathymetry near Gemini Prospect. Although the regional bathymetry trend is fairly 2D, it was not included in the 2D inversion models since the inversion lines have strike angles different than the bathymetry. Therefore, limiting the longest periods to 250 s minimizes the biasing of the inversion models from bathymetry distorted MT responses. The left column of Figures 3.9-3.22 show the results of independent TE and TM mode inversions of the 14 transects of data shown by the map in Figure 3.8. All inversions used an error floor of 5% (i.e. all errors less than 5% were set to 5%). Table 3.1 summarizes the number of sites used and the level of misfit obtained for each inversion. Most of the inversions easily achieved a misfit of 1.0, however, the TE inversion of Line A had trouble finding a misfit lower than about 1.69 without including some grossly irregular and obviously over-fit structure. Thus, the Line A TE inversion was set to converge to a misfit of 1.69 instead of 1.0. A few other inversions needed a similar relaxation of the target misfit level (see Table 3.1.)

Table 3.1: Table of number of sites and misfit for TE and TM mode two-dimensional inversions.

Line	A	B	C	D	E	G	H	I	J	K	L	1	2	3
# sites	17	4	2	5	3	2	3	7	4	8	4	3	5	6
TM misfit	1.10	1.0	1.0	1.0	1.0	1.0	1.24	1.17	1.0	1.20	1.44	1.0	1.0	1.0
TE misfit	1.69	1.0	1.0	1.0	1.0	1.0	1.0	1.17	1.0	1.0	1.0	1.44	1.0	1.3

Some of the inversions show good agreement with the seismic salt volume while others just barely show hints of resistive features and only where the salt is shallowest, or the inversion shows no resistive anomalies at all. However, some consistent features are prevalent when the models are compared. For instance, a marked difference in structure for each mode's inversion occurred for most of the transects. With the exception on line E, which does not resolve the deep and

thin salt, transects oriented at 45° (lines A-E) have better agreement with the seismic salt for TM mode inversions than for the TE mode. Conversely, transects oriented at 315° azimuths (lines G-L) generally show better agreement for TE mode inversions, except for transect K where the salt is thin. For the two transects oriented at 90° azimuth where salt volume data is available (lines 2 and 3), only line 3 shows a good agreement with the seismic salt for the TM mode inversion.

3.5.2 Synthetic 2D Inversions of 3D Forward Data

In order to assess the cause of the differences in structure between the TE and TM mode inversions, and to assess how much of the salt should be resolved if all sites had high quality data, a synthetic inversion study was done. It was assumed that the seismic salt model adequately represented the true Gemini salt structure. Creating synthetic 3D MT data from the seismic salt model and inverting it with the same 2D inversion used for the real data would illustrate whether the difference in mode sensitivities and structure was consistent with numerical simulations, or else arose from either differences between the true Gemini salt structure and the seismic salt or from particular noise features in the MT data.

The 3D MT forward response of the salt body was computed using a variation of a staggered grid finite difference formulation [*Newman and Alumbaugh*, 1995] which was written [*C. Weiss*, pers. comm.] to use a matrix-free approach [*Weiss*, 2001] to reduce computational storage requirements. A finite difference mesh was designed by dividing up the survey region into cells 350 by 350 m wide horizontally and 100 m thick vertically, resulting in a $113 \times 112 \times 111$ node grid. Resistivities within the salt region were set to a uniform value of 100 Ωm. Resistivity values outside the salt were set to 0.5 Ωm, a value commensurate with the 2D inversion results and equivalent to porous sediments saturated with seawater. A 1000 m thick seawater layer of 0.3 Ωm was added to the model in order to satisfy the seafloor boundary condition which allows vertical electrical current at the seafloor-sediment interface [*Hoversten et al.*, 1998]. MT forward responses

were calculated for the same site locations and frequencies used for the real data. The ideal (i.e. noise free) forward response data then had 5% random Gaussian noise applied to it to provide a more realistic set of data to for the inversion [e.g. *Constable*, 1991]. Data generated from this process will be referred to as *synthetic* data. The TE and TM mode synthetic data were then inverted using the same inversion routine and model parameterization as was done for the real data, a process referred to as *synthetic* inversion. All synthetic inversions were fit to a misfit of 1.0. The results are shown in the right hand columns of Figures 3.9-3.22.

Many of the features present in the real data inversions are also present in the synthetic inversions. Transects oriented at 45° (lines A-E) shows strong similarities in which the TM mode synthetic inversions recover shallow salt (less than about 4 km depth) but not deeper and thinner salt, while the TE mode synthetic inversions show no corresponding resistive features and look for the most part like 0.5 Ωm half-spaces. No basement was included in the 3D forward model and so the synthetic inversions differ from the real inversions in the lack of increase in resistivity at depths greater than about 6-7 km. Transects oriented at 315° (lines G-L) show some agreement with the real inversions in which the TE mode inversions recover the salt while the TM mode does not (lines H and I). Other 315° transects (lines J, K, L) show no resistive features that correspond to salt for either mode. Neither of the two 90° azimuth transects where salt volume data are available (lines 2 and 3) show good agreement with the salt boundaries for either TE or TM synthetic inversions. TE and TM mode synthetic inversions for line 1, which is north of the seismic salt volume show no resistive features.

3.6 Discussion of Modeling Results

The real and synthetic data inversions show that marine MT is able to image resistive salt given suitable conditions. The two most successful transects shown above are the TM mode inversion for line A (Figure 3.9) and the TE mode

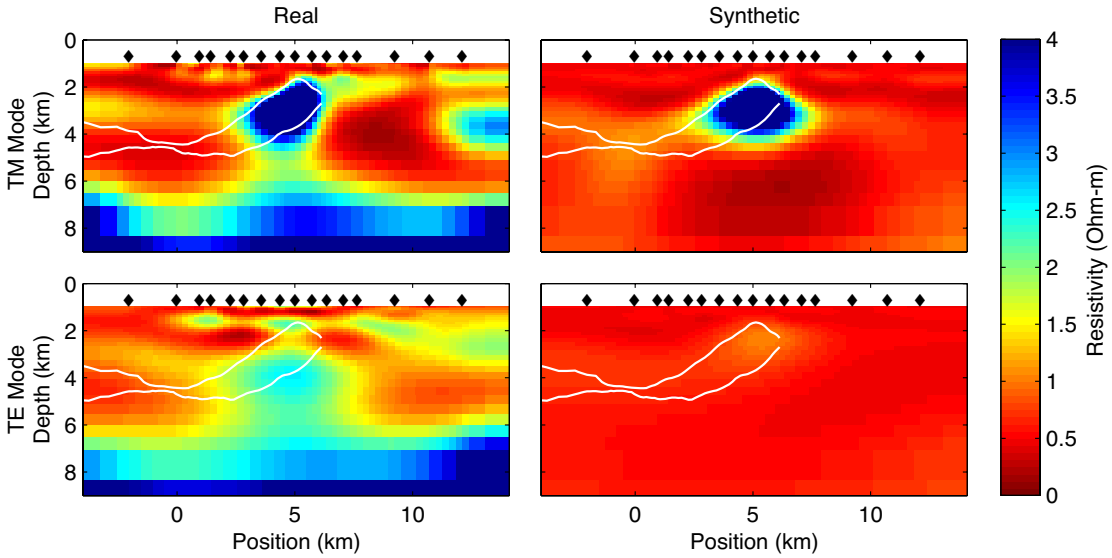

Figure 3.9: Inversion results for Line A. Real data were used for the figures on the left and synthetic 3D forward data for the figures on the right. The models are oriented from south-west (left) to north-east (right). The top and bottom rows show results for TM and TE mode data. The white outline shows the location of the top and bottom surfaces of the salt structure as determined from 3D seismic reflection data. MT site locations are shown as black diamonds. Resistivity values are shown on a *linear* color scale.

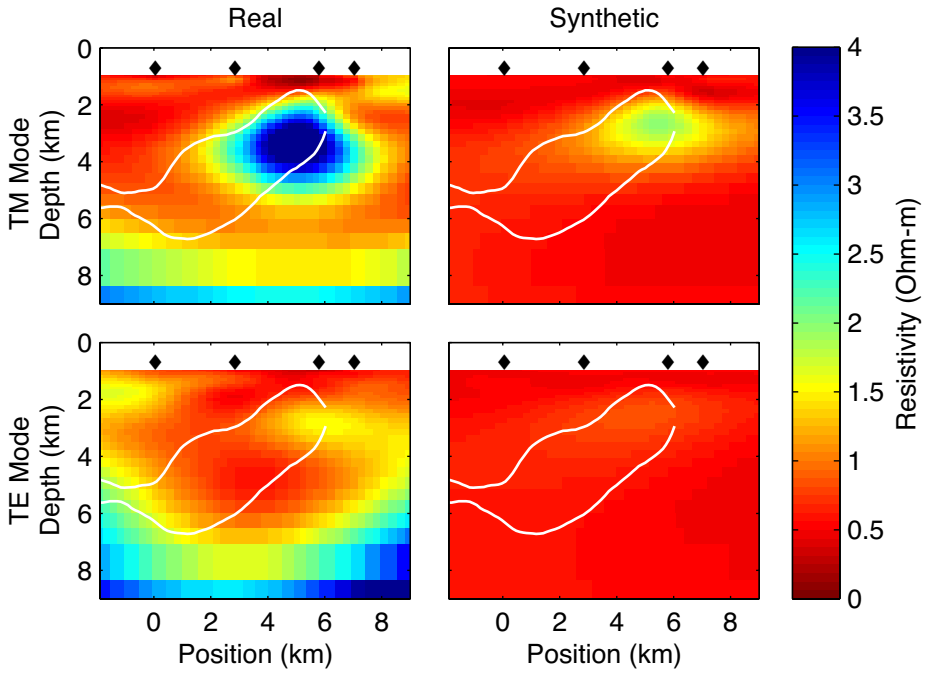

Figure 3.10: Inversion results for Line B. The models are oriented from south-west (left) to north-east (right).

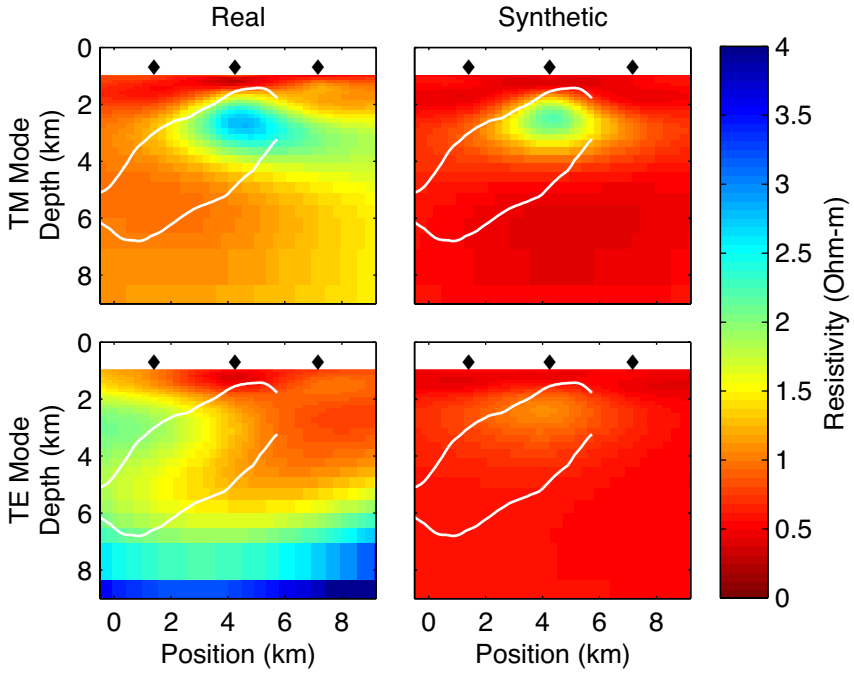

Figure 3.11: Inversion results for Line C. The models are oriented from south-west (left) to north-east (right).

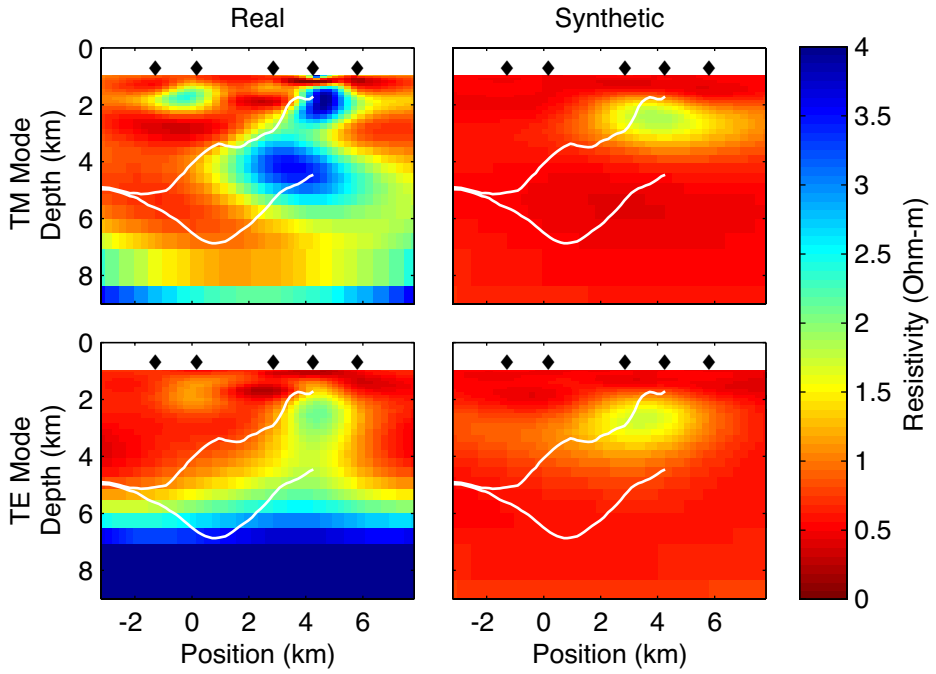

Figure 3.12: Inversion results for Line D. The models are oriented from south-west (left) to north-east (right).

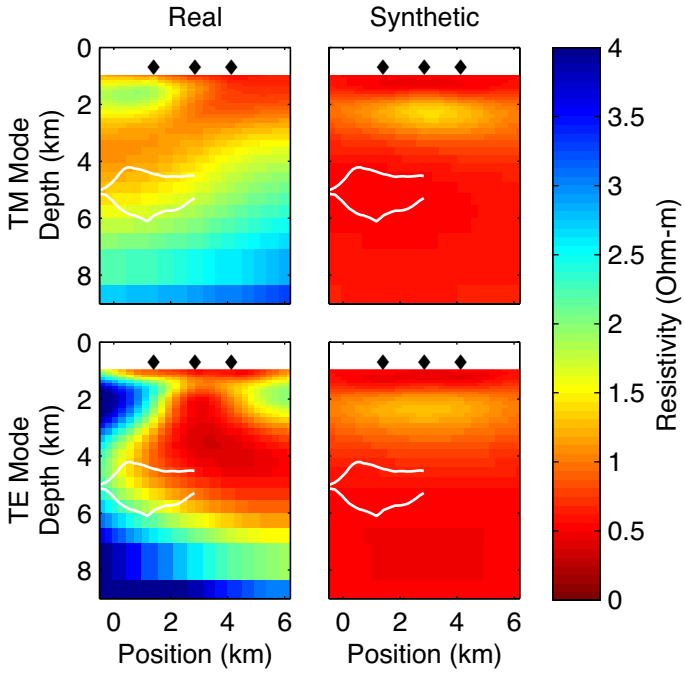

Figure 3.13: Inversion results for Line E. The models are oriented from south-west (left) to north-east (right).

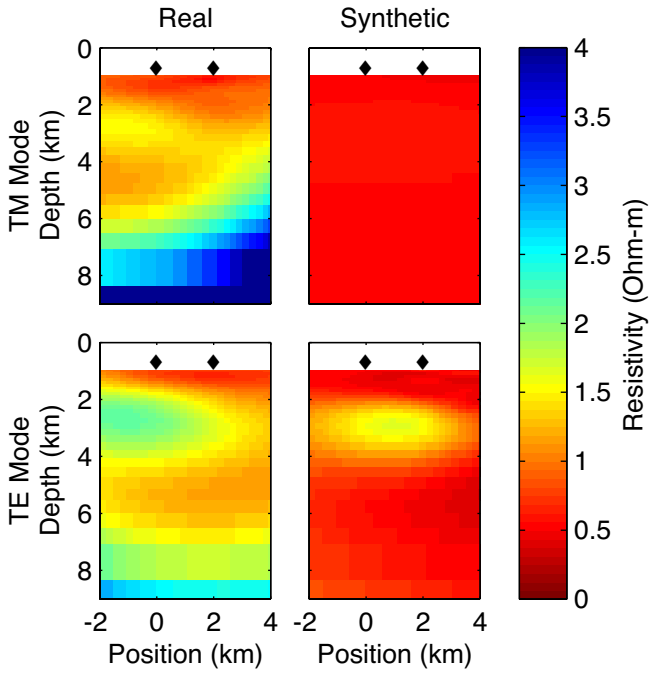

Figure 3.14: Inversion results for Line G. The models are oriented from south-east (left) to north-west (right).

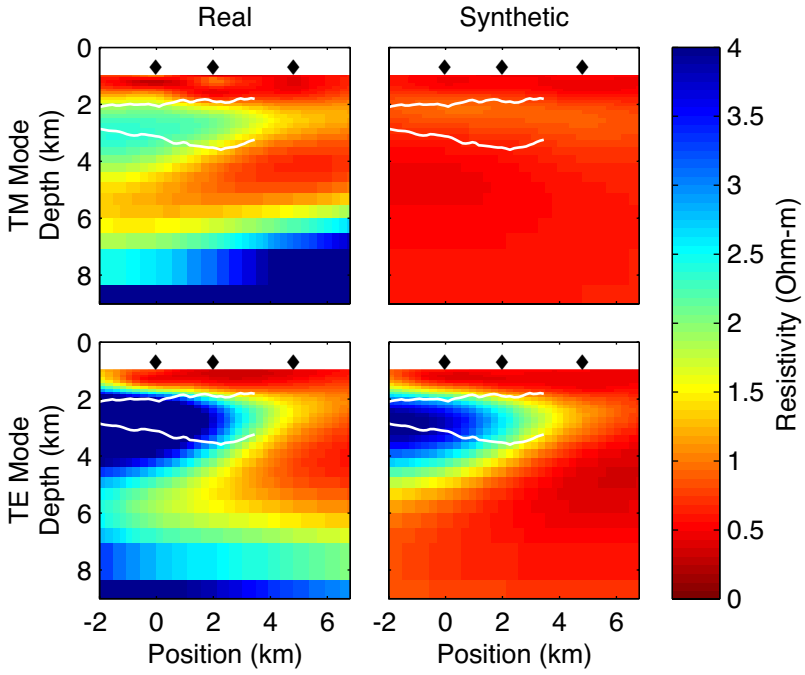

Figure 3.15: Inversion results for Line H. The models are oriented from south-east (left) to north-west (right).

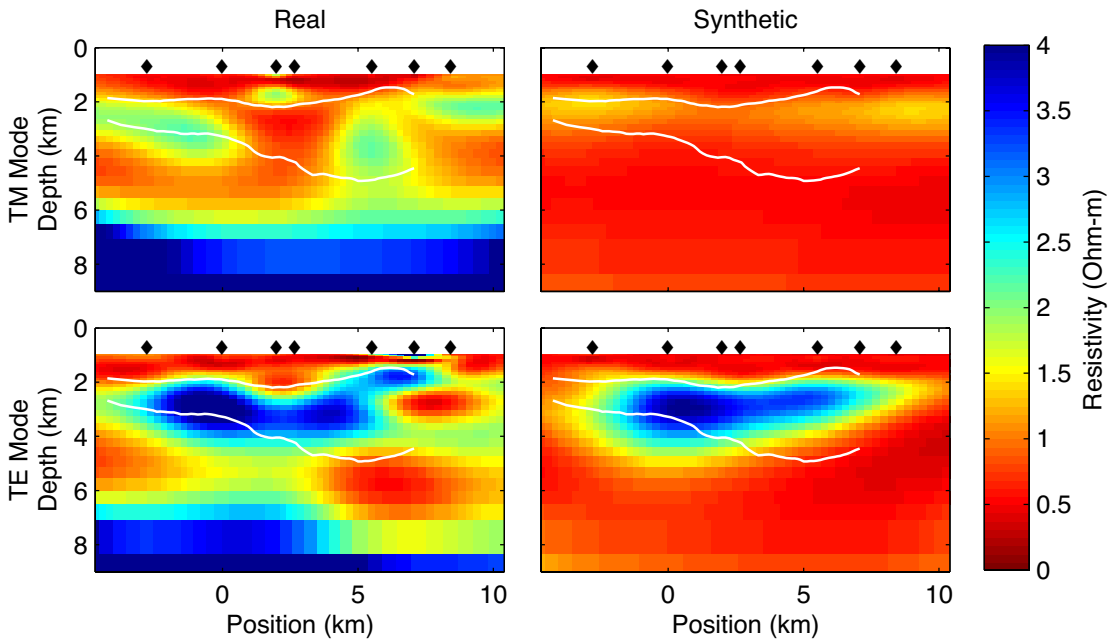

Figure 3.16: Inversion results for Line I. The models are oriented from south-east (left) to north-west (right).

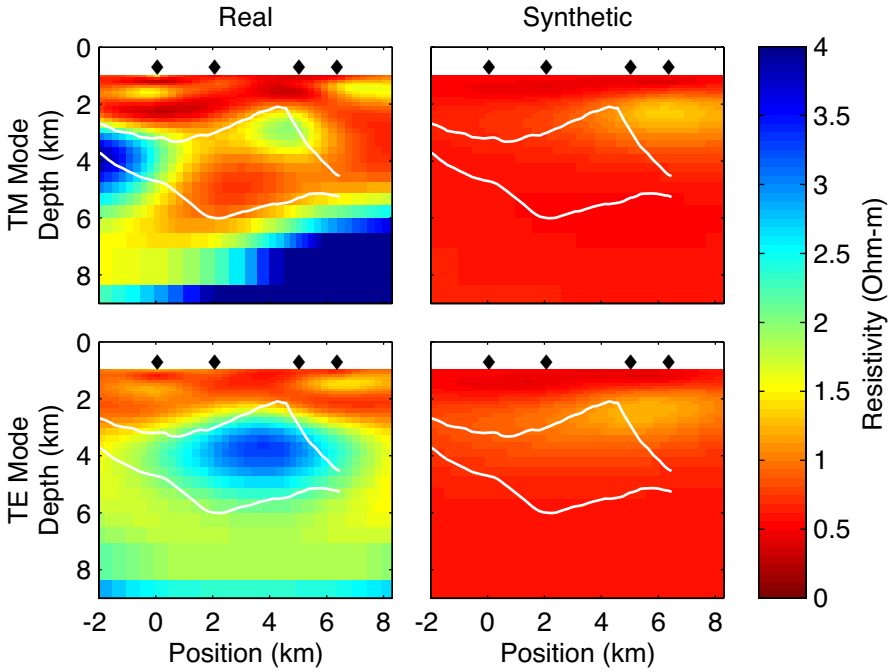

Figure 3.17: Inversion results for Line J. The models are oriented from south-east (left) to north-west (right).

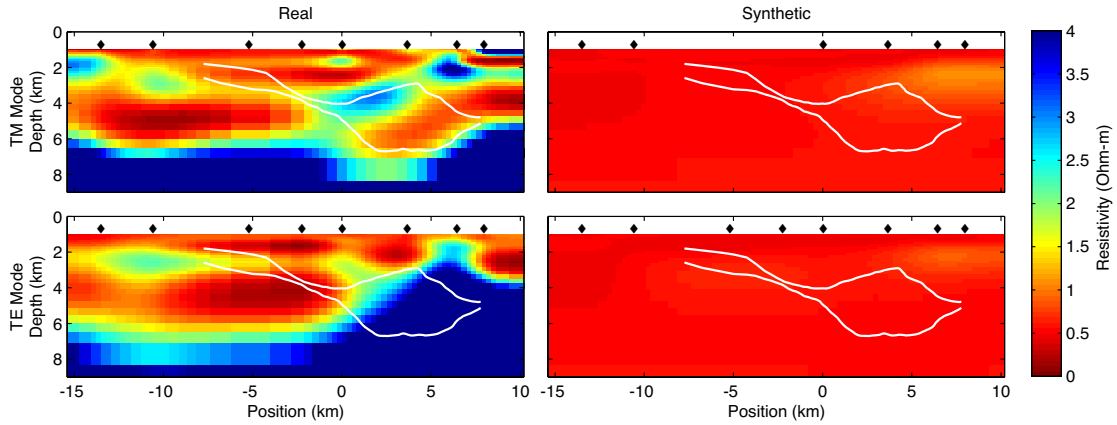

Figure 3.18: Inversion results for Line K. The models are oriented from south-east (left) to north-west (right).

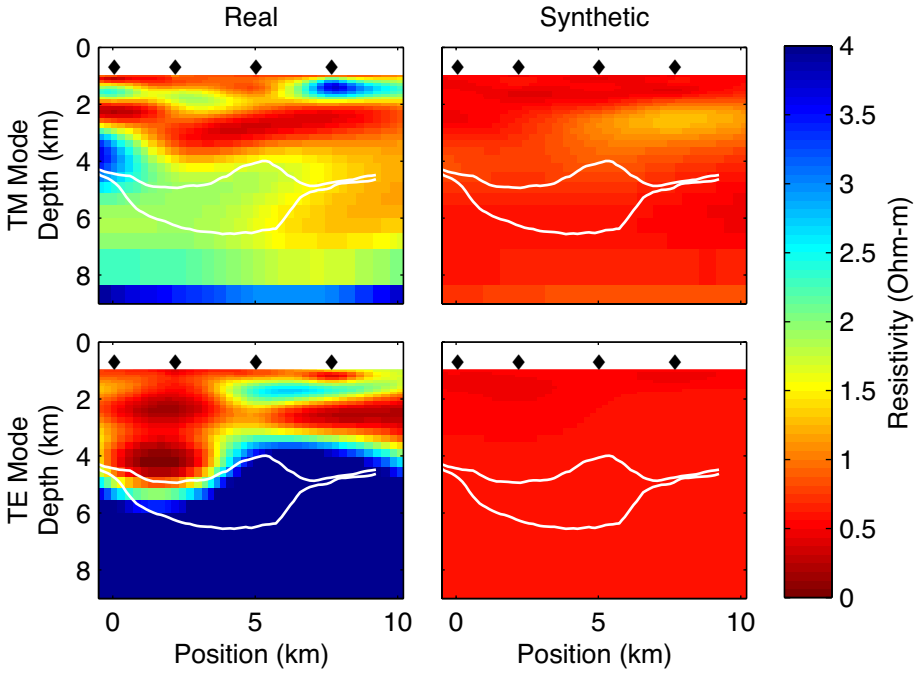

Figure 3.19: Inversion results for Line L. The models are oriented from south-east (left) to north-west (right).

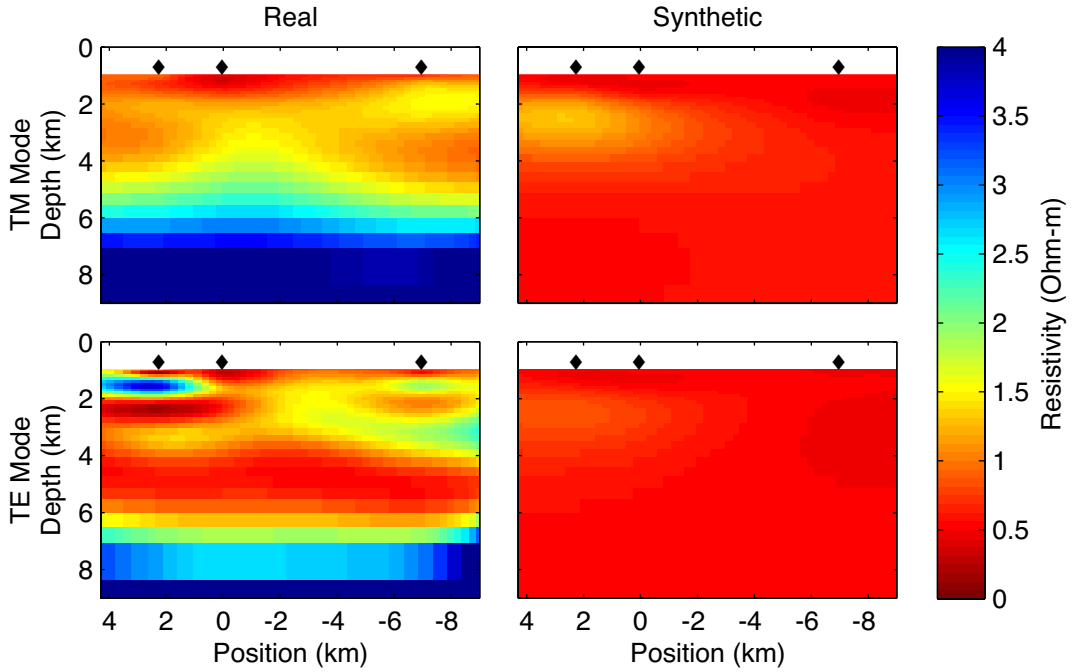

Figure 3.20: Inversion results for Line 1. The models are oriented from west (left) to east(right).

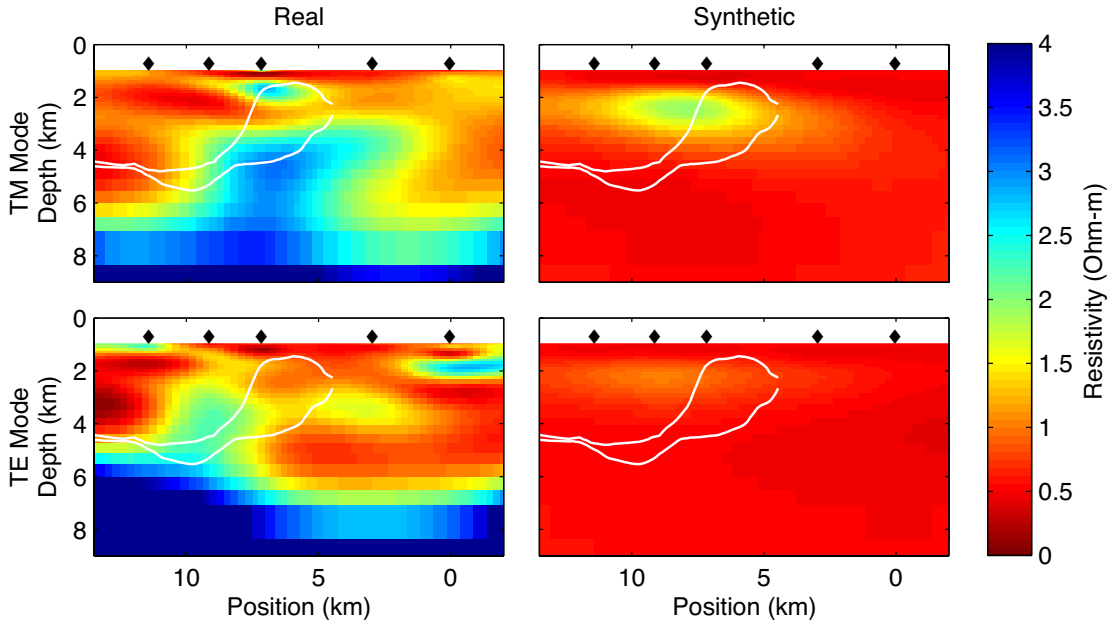

Figure 3.21: Inversion results for Line 2. The models are oriented from west (left) to east (right).

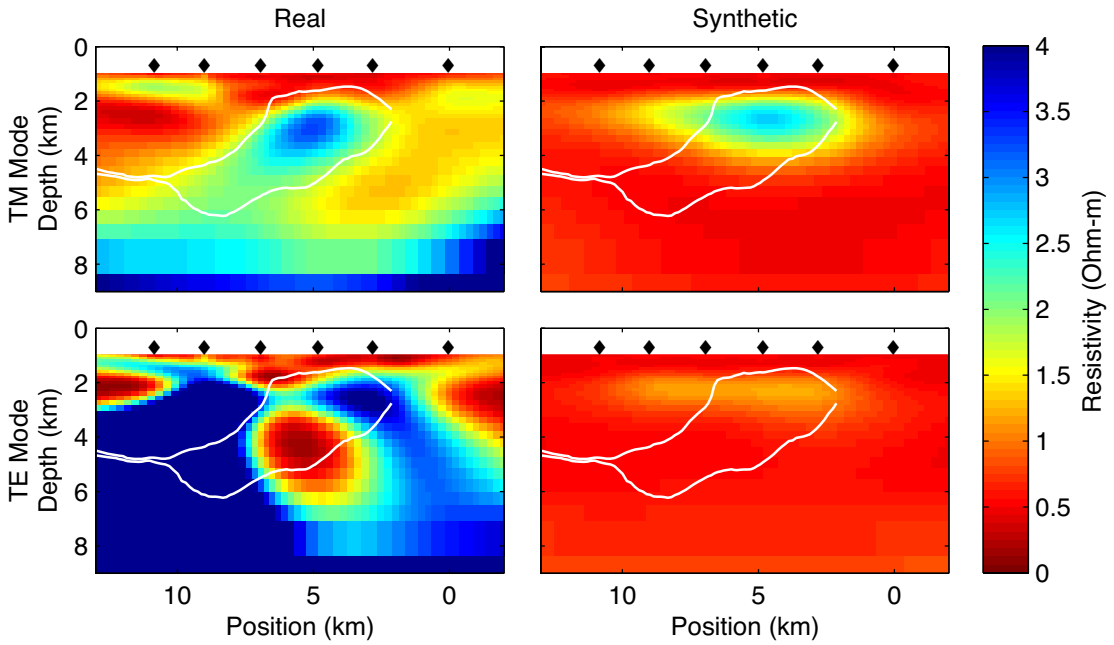

Figure 3.22: Inversion results for Line 3. The models are oriented from west (left) to east (right).

inversion of line I (Figure 3.16). The disparity in structure between the TM and TE mode inversion of line A agrees with the conventional wisdom that TM mode inversions would yield the better structural agreement than the TE mode [*Hoversten et al.*, 1998]. However, TE mode inversions of both real and synthetic data for line I contradict this. Looking at the dominant strike of the top-of-salt as shown in Figure 3.4 shows that both the TM mode data for line A and the TE mode data for line I have electric fields oriented orthogonal to the dominant structural strike. This suggests a new dictum: 2D inversion of 3D resistive structures yields the best agreement when inverting the mode with the electric field perpendicular to the dominant structural strike.

For most lines, resistive salt shallower than about 4-5 km is resolved by one of the TE or TM mode inversions. Where the salt is deeper most models show no resistive anomalies for both thick and thin salt. The exceptions are the TE mode inversions for lines K and L which show deep salt that blends down into the resistive

basement. The lack of resolution of the deeper salt is in agreement with numerical modeling [*Hoversten et al.*, 1998] that showed 2D inversions will not recover deep salt when its lateral extent is limited. *Hoversten et al.* [1998] also showed that deep salt with a 12 km strike length resulted in a 25% TM apparent resistivity anomaly at 1000 s period, which suggests that future 3D inversion may recover the deep salt since an appreciable signal is present in the MT response. TE inversions for lines J-L show progressively different structure for the real inversions while synthetic inversions show no resistive structure at all. As the real data inversion shows, it may indeed be the case here that the salt *is* deeply rooted or attached to the autochthonous Louann source layer. If the salt is deeply rooted, the synthetic inversions may not have recovered this structure since the forward modeled salt volume used to create the synthetic data did not include a deep root or resistive basement.

The synthetic inversions show a systematically smaller salt resistivity than the real data inversions, and typically underestimate the salt size as well. This may be because we did not include a resistive basement in the synthetic models. As shown in Chapter 2, the MT electric fields in the seawater become stronger (and have a higher current density) as the seafloor resistivity increases. The same situation holds for the relatively conductive sediments over a resistive basement; the current density in the sediments above the basement is much higher than the case of no resistive basement. The higher current density may result in a slightly larger MT response and sensitivity to the salt structure, which allows the inversion to recover more of the salt. Conversely, the size difference may also be due to the difference in error structure of the real versus synthetic data. While the real data have error bars that may vary in size from period to period, the synthetic data have a uniform 5% error structure. The real data tend to have smaller error bars at periods where the signal level is highest, which are also periods most sensitive to the salt; it may be that the real inversions are using the misfit budget to fit data that are more sensitive to the salt while relatively ignoring periods with larger

error bars and less salt sensitivity. The synthetic inversions instead spend the misfit budget trying to fit all periods of data equally well since the error structure is uniform.

The effect of the resistive basement may also account for the unusually large misfit for the TE inversion for Line A. While the synthetic TE inversion easily achieved a misfit of 1.0 with a nearly uniform half-space model, the real TE inversion only achieved a misfit of 1.69 and has considerable structure that only partially agrees with the seismic salt volume. As mentioned above, the high basement resistivity may allow for more sensitivity to the overlying 3D salt. Since Line A has the highest MT site density, it may be harder to find a 2D TE model compatible with the data than it is for another, lower site density transect, such as Line B, since there are more constraints on where model structure is allowed by the data. Future 3D inversion or synthetic 2D inversion using a 3D forward model that includes a resistive basement may verify this.

3.7 Joint Analysis with Seismic Reflection Data

The above sections have shown that 2D MT is effective for imaging the resistive salt structure; it is also worthwhile to examine other features of the resistivity model. To increase the reliability of interpreting the model features, a joint presentation of seismic reflection profiles and the resistivity models is shown here. Depth migrated seismic reflection profiles were provided for lines A and I by WesternGeco and ChevronTexaco [David Bartel, pers. comm.]. Figure 3.23 shows the combined models for line A and figure 3.24 shows the combined models for line I. The top and base-of-salt reflections are readily apparent in Figure 3.23 as they are the strongest reflections at depths less than about 6 km. As was shown earlier, the MT model shows good agreement with the salt structure where it is shallower than about 4-5 km. Bright reflections seen at depths of about 7 km correspond with an increase in resistivity and show the transition to either basement rocks or an

overlying *chalk* layer [*Schuster*, 1995]. An increase in resistivity to about 1.5 Ωm at depths of about 2 km and horizontal positions of about 6 to 10 km correlates well with some reflections. There is also an indication that this feature continues farther to the right of the model. A thin resistive feature in this region is also required by recently collected controlled-source EM data [J. Behrens, pers. comm.]. This region lies outside the seismically modeled salt volume and so is probably not salt. As indicated Figure 3.2, this region is on the outside edge of a lateral portion of the roho system that Gemini lies within and there may be a component of strike-slip to the roho system along this edge. Given this information, a few explanations are possible for the increase in resistivity. One is that the resistive feature represents a less permeable sedimentary layer which has a higher resistivity since it contains less seawater than the surrounding sediments. The layer may have once been continuous to the left portion of the model, but the listric growth faulting of the roho system and the salt intrusion has since moved this layer away (basin-ward). Another explanation is that the increase in resistivity represents an increase in the pore fluid resistivity. Resistive fluids in this layer may be contained by a natural trap formed by the salt intrusion and faulting, as shown by the seismic reflections bending up against the salt. If the resistive fluids are less dense then seawater, then they may have migrated laterally along the sloping sedimentary layers and become trapped by the relatively impermeable salt. The resistive fluid may be a hydrocarbon as it would then meet the requirement of being more resistive than seawater and less dense. The subsalt prospect at Gemini is a gas sand at about 4 km depth [*Ogilive and Purnell*, 1996], and so this shallower resistive feature may be another, undetected gas reservoir. At the depths of this feature the temperature is expected to be low enough allow the formation of gas hydrates; gas that has migrated upward from the gas sand and collected here may exist in hydrate form.

The combined image for line I shown in Figure 3.23 illustrates how MT can help resolve structure in regions where seismic models are ambiguous. While

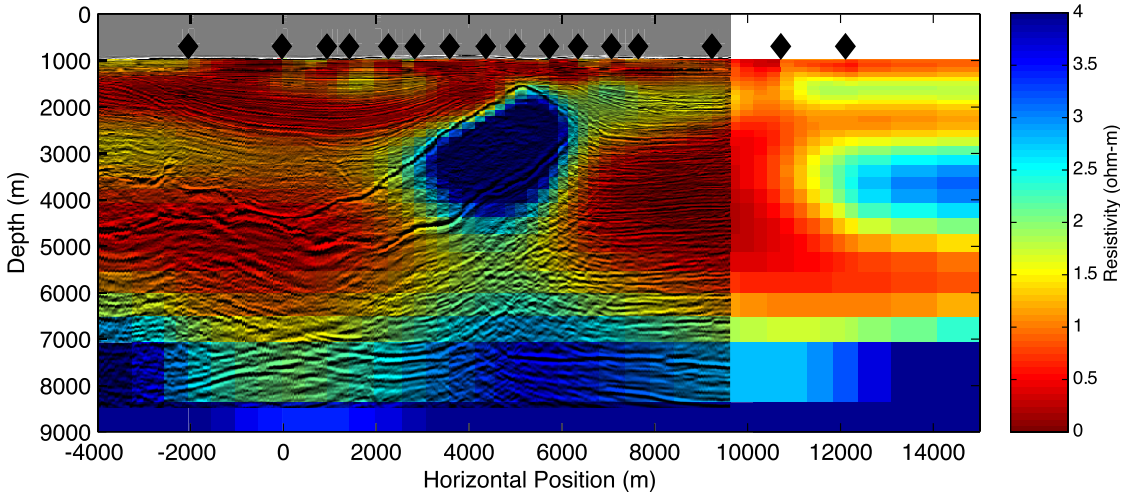

Figure 3.23: Line A: combined MT and reflection models. Black lines show depth migrated reflections from a 3D seismic survey.

the top-of-salt reflection is easily seen, the base-of-salt reflection loses coherence at lateral positions of about 5 km. The resistivity model helps resolve this ambiguity by suggesting that the salt is not deeply rooted in this region, as indicated by the low resistivity at depths of about 5-7 km. A shallow and thin finger of salt seen as a resistive feature at positions of about 5-8 km and depths around 2 km also correlates well with the top-of-salt reflection and another strong reflection at about 2.5 km depth. As shown in Figure 3.16, the interpreted base-of-salt from the seismic survey lies much deeper than this overhanging feature. The MT model contradicts this by indicating that the salt finger overhangs a conductive zone that is probably porous sediments. Beneath the conductive zone the resistivity increases slightly at depths of about 3.5-4.5 km, but then decreases again at depths greater than about 4.5 km, indicating that the salt does not have a resistive root here.

3.8 Conclusions

This study shows that given suitable conditions, 2D marine MT is effective for mapping resistive 3D salt structures and can recover the salt volume boundaries when inverting the mode with the electric field oriented across the

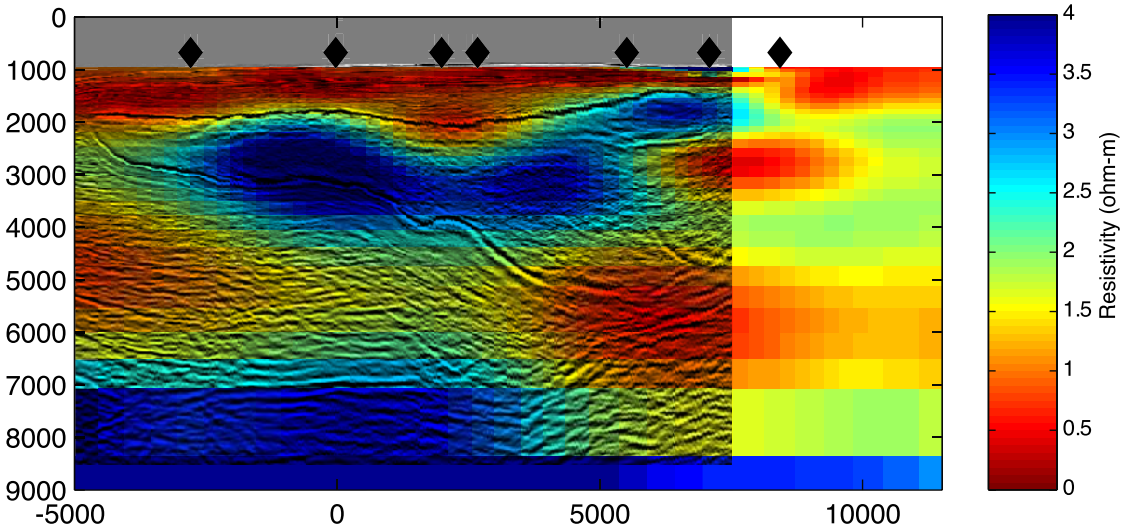

Figure 3.24: Line I: combined MT and reflection models. Black lines show depth migrated reflections from a 3D seismic survey.

dominant structural strike. For most lines of MT stations, one of the TE or TM inversions recovered salt shallower than about 5-4 km. However, deeper salt and 3D regions of the salt were not recovered by the 2D inversions and suggests the need for fully 3D inversion of the MT data. The joint presentation of seismic reflection and electrical resistivity allows for a more complete interpretation of both data sets, and allows stronger conclusions to be made about the salt structure and surrounding sediments. Ambiguities in the seismic interpretation, particularly in regions where the base-of-salt reflections are incoherent, can be resolved through such joint interpretation.

Acknowledgments

The Seafloor Electromagnetic Methods Consortium at Scripps Institution of Oceanography provided the necessary funding to carry out this work. Consortium members past and present include: Anadarko, Shell, Texaco, Chevron, AGIP, BP, BHP, British Gas, ExxonMobil, GERD, AOA Geophysics, Norsk-Hydro, Statoil, OHM and ISL. The authors thank David Bartel, ChevronTexaco and West-

ernGeco for providing the 3D seismic data and salt volume. Arnold Orange and AOA Geophysics are thanked for their collaboration in collecting the MT data. The authors also thank the Captains and crews of the R/V Pelican, R/V Gyre, and R/V Longhorn and the following people for their efforts for the research cruises: Jacques Lemire, David Willoughby, Lisl and Rhodri Lewis, Ransom Reddig, Marianne Mulrey, Almuth von den Steinen, Adam Agundes, James Behrens, Mark Everett, Joshua King, Lucy MacGregor, Hiatt Sheller, Cristiano Signorini, and Stephanie Rothe.

The text of this chapter, in part or in full, is a reprint of the material as has been submitted for publication as Key, K., S. Constable, and C. Weiss, Mapping 3D Salt with 2D Marine MT: Case Study from Gemini Prospect, Gulf of Mexico, *Geophysics.* The dissertation author was the primary researcher and author of the published work. The co-author listed in the publication directed and supervised the research which forms the basis for this chapter.

References

Constable, S., Comment on 'Magnetic appraisal using simulated annealing' by S. E. Dosso and D. W. Oldenburg, *Geophys. J. Int.*, *106*, 387–388, 1991.

Constable, S. C., R. L. Parker, and C. G. Constable, Occam's inversion - A practical algorithm for generating smooth models from electromagnetic sounding data, *Geophysics*, *52*, 289–300, 1987.

Constable, S. C., A. S. Orange, G. M. Hoversten, and H. F. Morrison, Marine magnetotellurics for petroleum exploration Part I: A sea-floor equipment system, *Geophysics*, *63*, 816–825, 1998.

de Groot-Hedlin, C., and S. Constable, Occam's inversion to generate smooth two-dimensional models from magnetotelluric data, *Geophysics*, *55*, 1613–1624, 1990.

Diegel, F. A., J. F. Karlo, D. C. Schuster, R. C. Shoup, and P. R. Tauvers, Cenozoic structural evolution and tectono-stratigraphic framework of the norther Gulf Coast continental margin, in *Salt tectonics: a global perspective: AAPG Memoir 65*, edited by M. P. A. Jackson, D. G. Roberts, and S. Snelson, pp. 109–151, 1995.

Egbert, G. D., Robust multiple-station magnetotelluric data processing, *Geophys. J. Int.*, *130*, 475–496, 1997.

Filloux, J. H., North Pacific magnetotelluric experiments, *J. Geomag. Geoelectr.*, *32*, 33–43, 1980.

Fletcher, R. C., M. R. Hudec, and I. A. Watson, Salt glacier and composite sediment-salt glacier models for the emplacement and early burial of allochthonous salt sheets, in *Salt tectonics: a global perspective: AAPG Memoir 65*, edited by M. P. A. Jackson, D. G. Roberts, and S. Snelson, pp. 77–108, 1995.

Hoehn, G. L., and B. N. Warner, Magnetotelluric measurements in the Gulf of Mexico at 20 m ocean depths, in *Magnetotelluric methods*, edited by K. Vozoff, pp. 578–597, Soc. Expl. Geophys., 1986, reprinted from CRC Handbook of Geophysical Exploration at Sea, 397-416.

Hoversten, G. M., H. F. Morrison, and S. C. Constable, Marine magnetotellurics for petroleum exploration, Part II: Numerical analysis of subsalt resolution, *Geophysics*, *63*, 826–840, 1998.

Hoversten, G. M., S. C. Constable, and H. F. Morrison, Marine magnetotellurics for base-of-salt mapping: Gulf of Mexico field test at the Gemini structure, *Geophysics*, *65*, 1476–1488, 2000.

Newman, G. A., and D. L. Alumbaugh, Frequency-domain modelling of airborne electromagnetic responses using staggered finite differences, *Geophys. Prosp.*, *43*, 1021–1042, 1995.

Ogilive, J. S., and G. W. Purnell, Effects of salt-related mode conversions on subsalt prospecting, *Geophysics*, *61*, 331–348, 1996.

Peel, F. J., C. J. Travis, and J. R. Hossack, Genetic structural provinces and salt tectonics of the cenozoic offshore U.S. Gulf of Mexico: a preliminary analysis, in *Salt tectonics: a global perspective: AAPG Memoir 65*, edited by M. P. A. Jackson, D. G. Roberts, and S. Snelson, pp. 153–175, 1995.

Schuster, D. C., Deformation of allochthonous salt and evolution of related salt-structural systems, eastern Louisiana Gulf Coast, in *Salt tectonics: a global perspective: AAPG Memoir 65*, edited by M. P. A. Jackson, D. G. Roberts, and S. Snelson, pp. 177–198, 1995.

Smith, W. H. F., and D. T. Sandwell, Global sea floor topography from satellite altimetry and ship depth soundings, *Science*, *277*, 1956–1962, 1997.

Vozoff, K., The magnetotelluric method in the exploration of sedimentary basins, *Geophysics*, pp. 98–141, 1972.

Wannamaker, P. E., J. A. Stodt, and L. Rijo, A stable finite-element solution for two-dimensional magnetotelluric modeling, *Geophys. J. R. astr. Soc.*, *88*, 277–296, 1987.

Weiss, C. J., A matrix-free approach to solving the fully 3D electromagnetic induction problem, *SEG Int'l Exposition and Annual Meeting, San Antonio, Texas*, 2001.

Appendix A: MT Responses

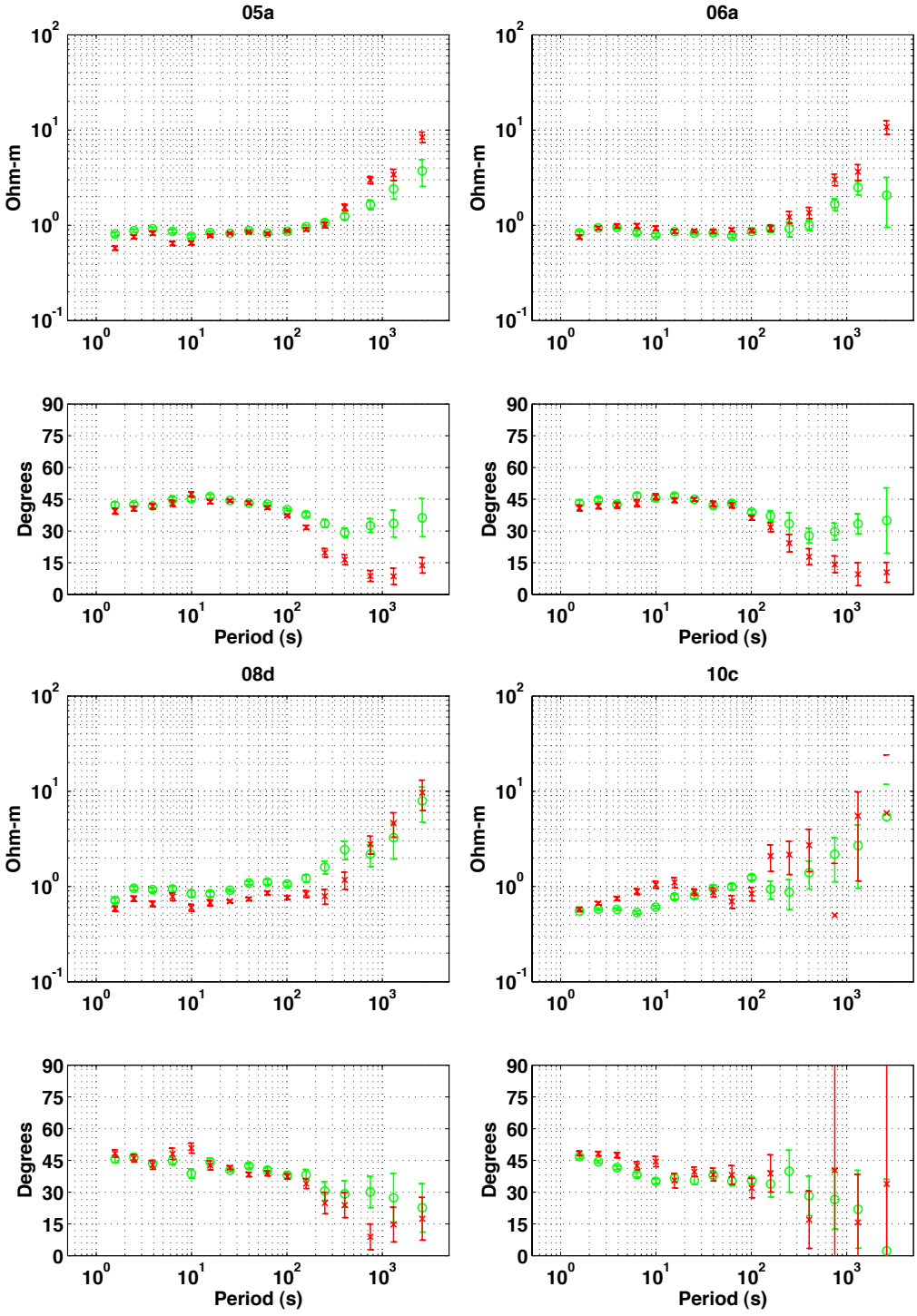

Figure 3.25: Gemini Prospect MT responses for sites 05a, 06a, 08d, and 10c. Green symbols correspond to Zxy, where x is oriented at 45° from North, and red symbols are for Zyx. See Figure 3.3 for site locations.

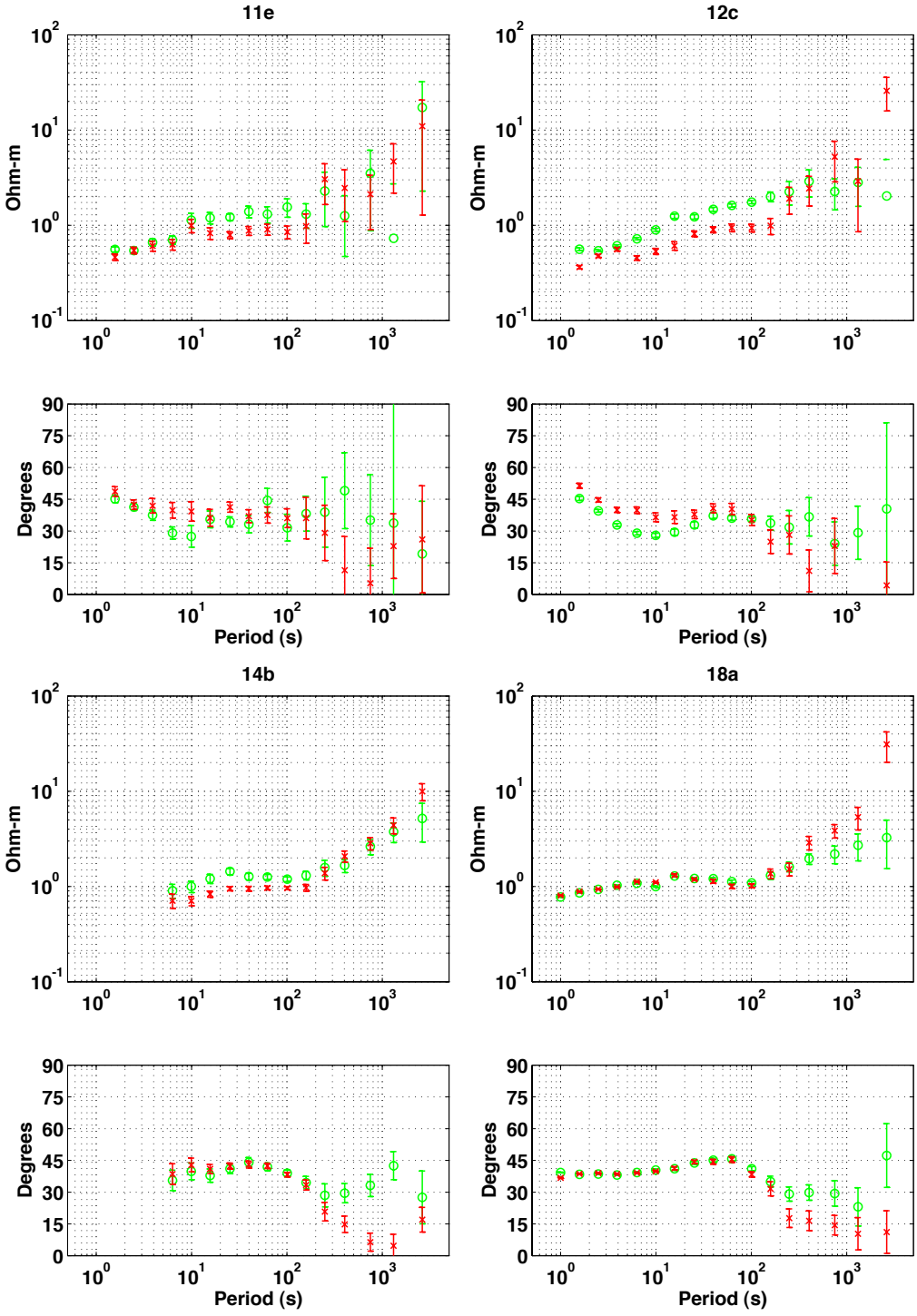

Figure 3.26: Gemini Prospect MT responses for sites 11e, 12c, 14b, and 18a. Green symbols correspond to Zxy, where x is oriented at 45° from North, and red symbols are for Zyx.

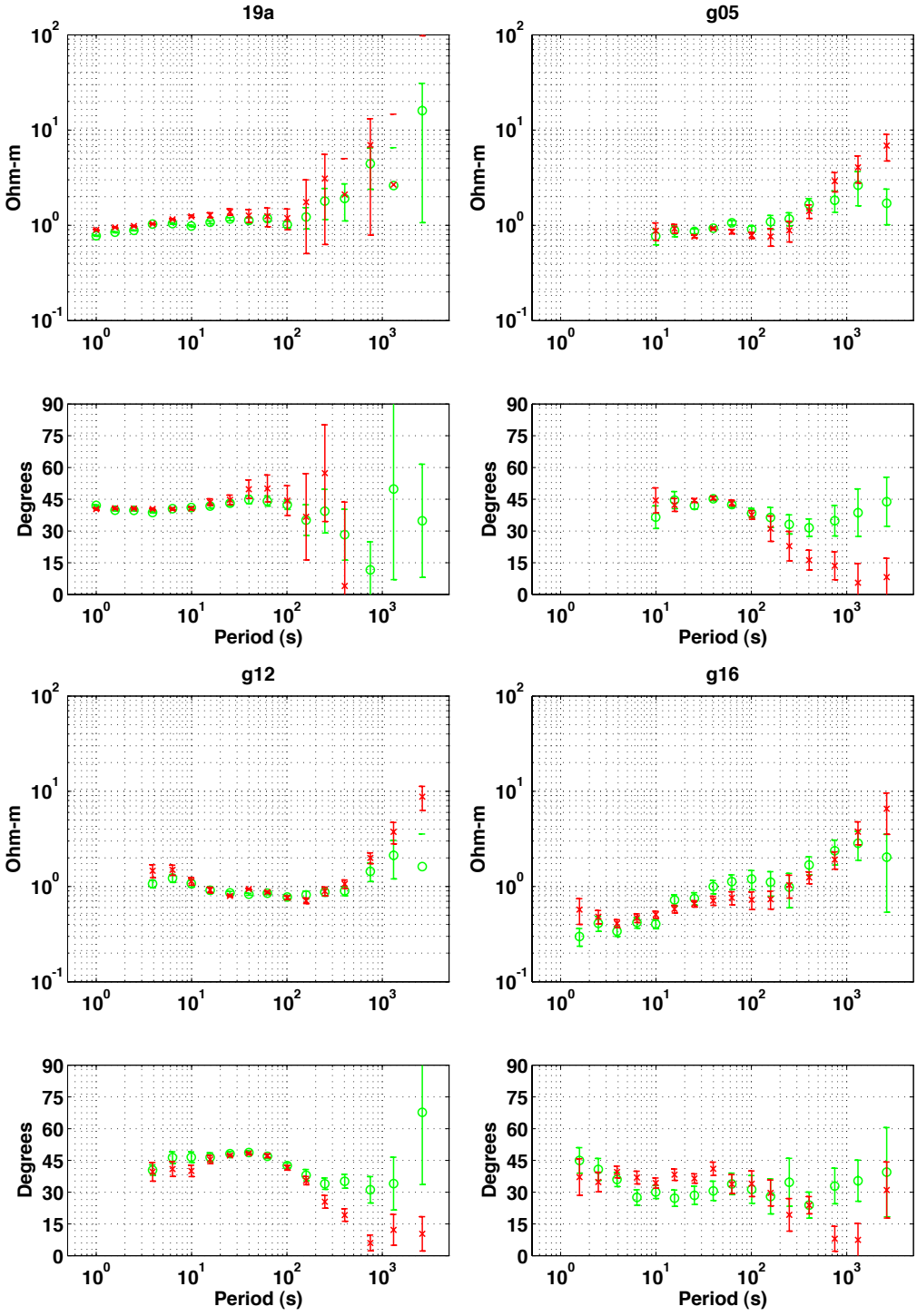

Figure 3.27: Gemini Prospect MT responses for sites 19a, g05, g12, and g16. Green symbols correspond to Zxy, where x is oriented at 45° from North, and red symbols are for Zyx.

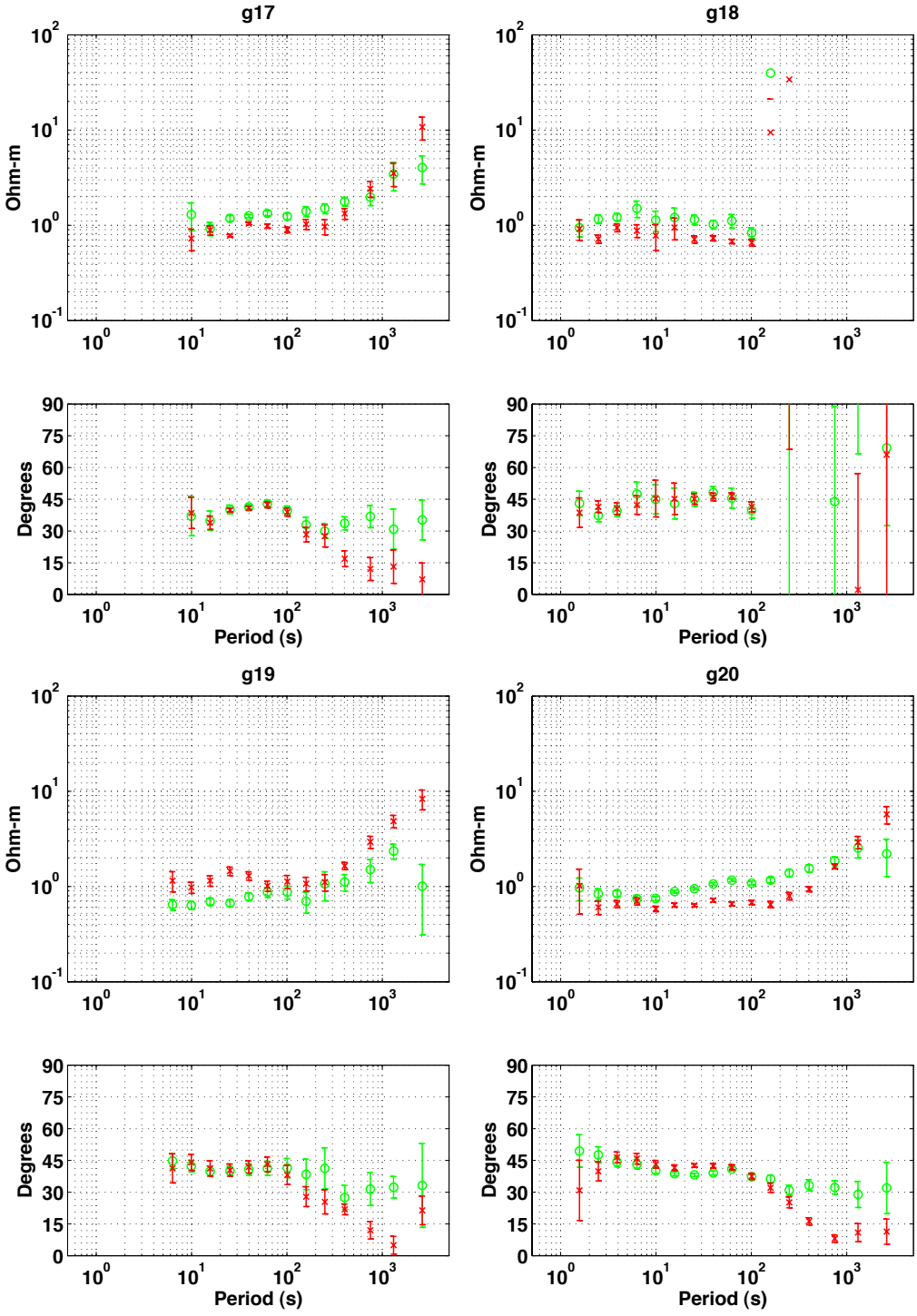

Figure 3.28: Gemini Prospect MT responses for sites g17, g18, g19, and g20. Green symbols correspond to Zxy, where x is oriented at 45° from North, and red symbols are for Zyx.

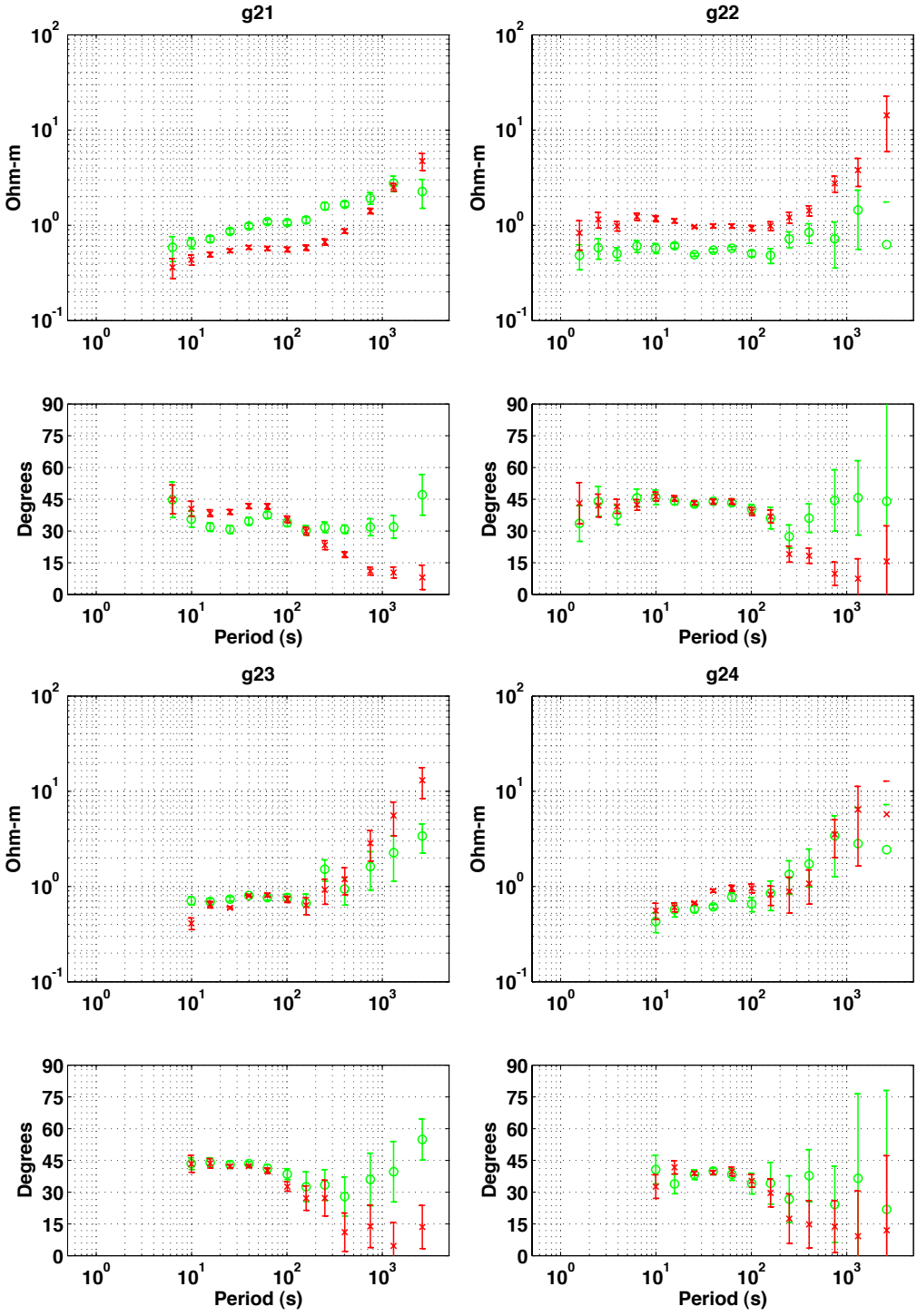

Figure 3.29: Gemini Prospect MT responses for sites g21, g22, g23, and g24. Green symbols correspond to Zxy, where x is oriented at 45° from North, and red symbols are for Zyx.

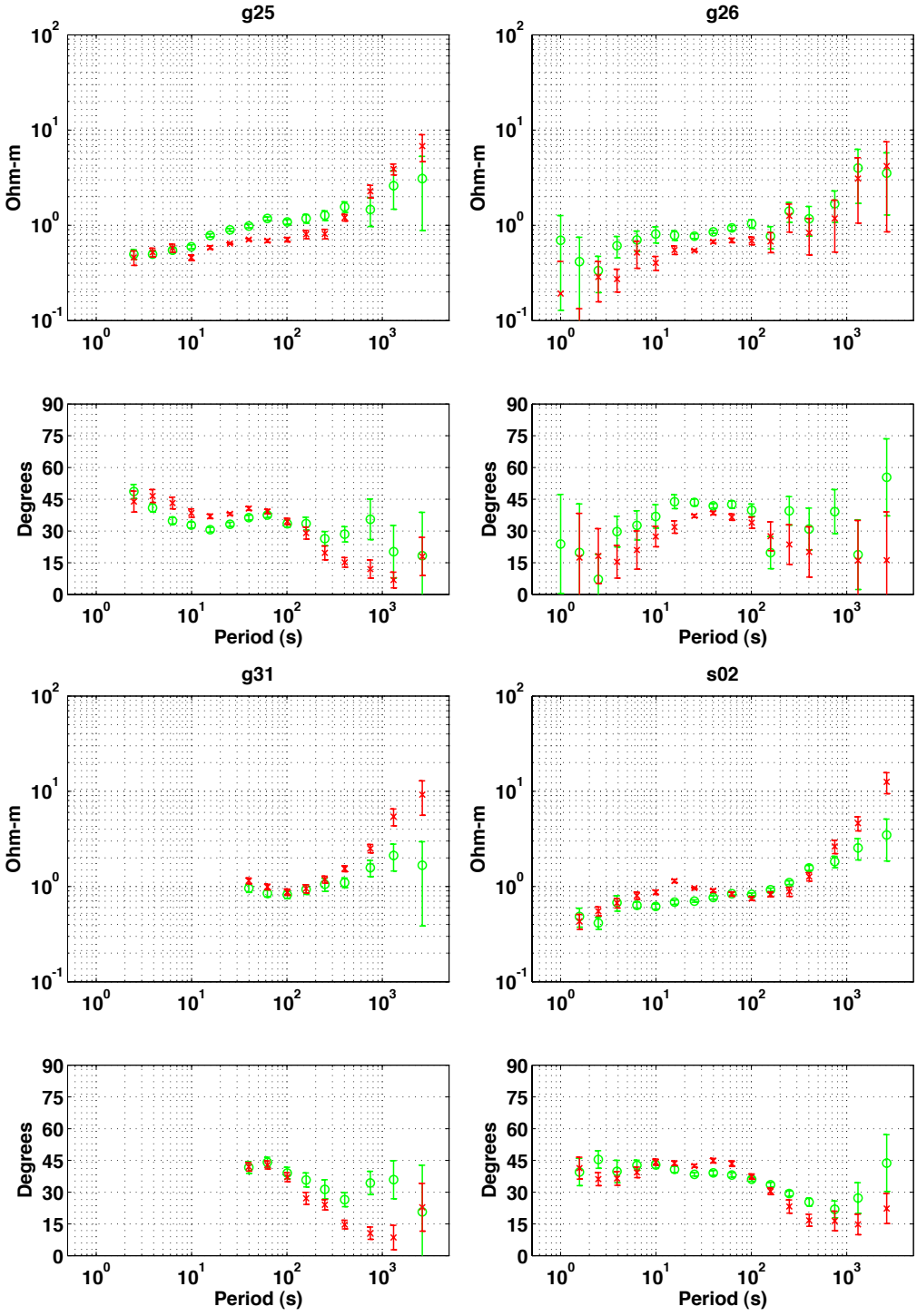

Figure 3.30: Gemini Prospect MT responses for sites g25, g26, g31 and s02. Green symbols correspond to Zxy, where x is oriented at 45° from North, and red symbols are for Zyx.

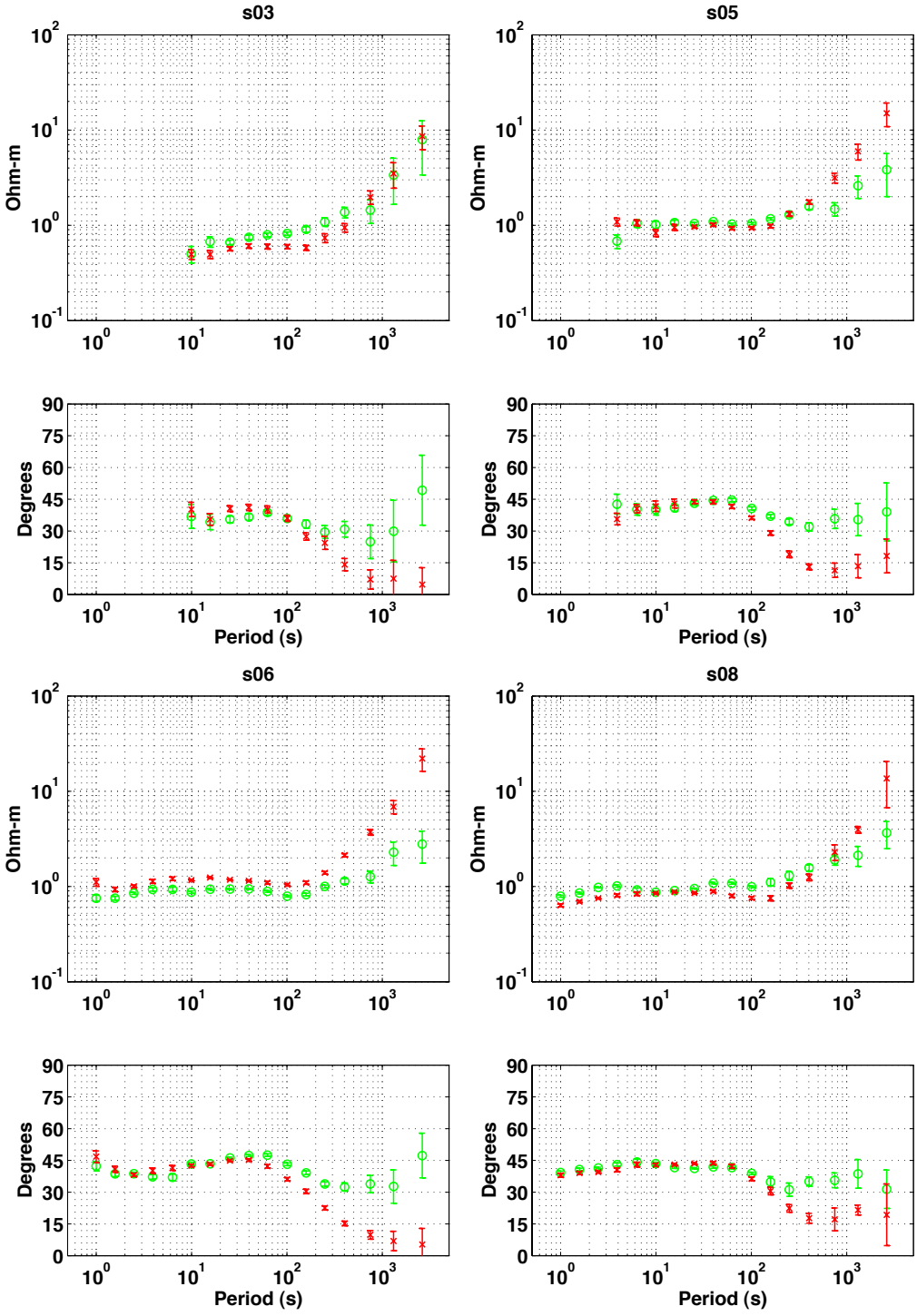

Figure 3.31: Gemini Prospect MT responses for sites s03, s05, s06, and s08. Green symbols correspond to Zxy, where x is oriented at 45° from North, and red symbols are for Zyx.

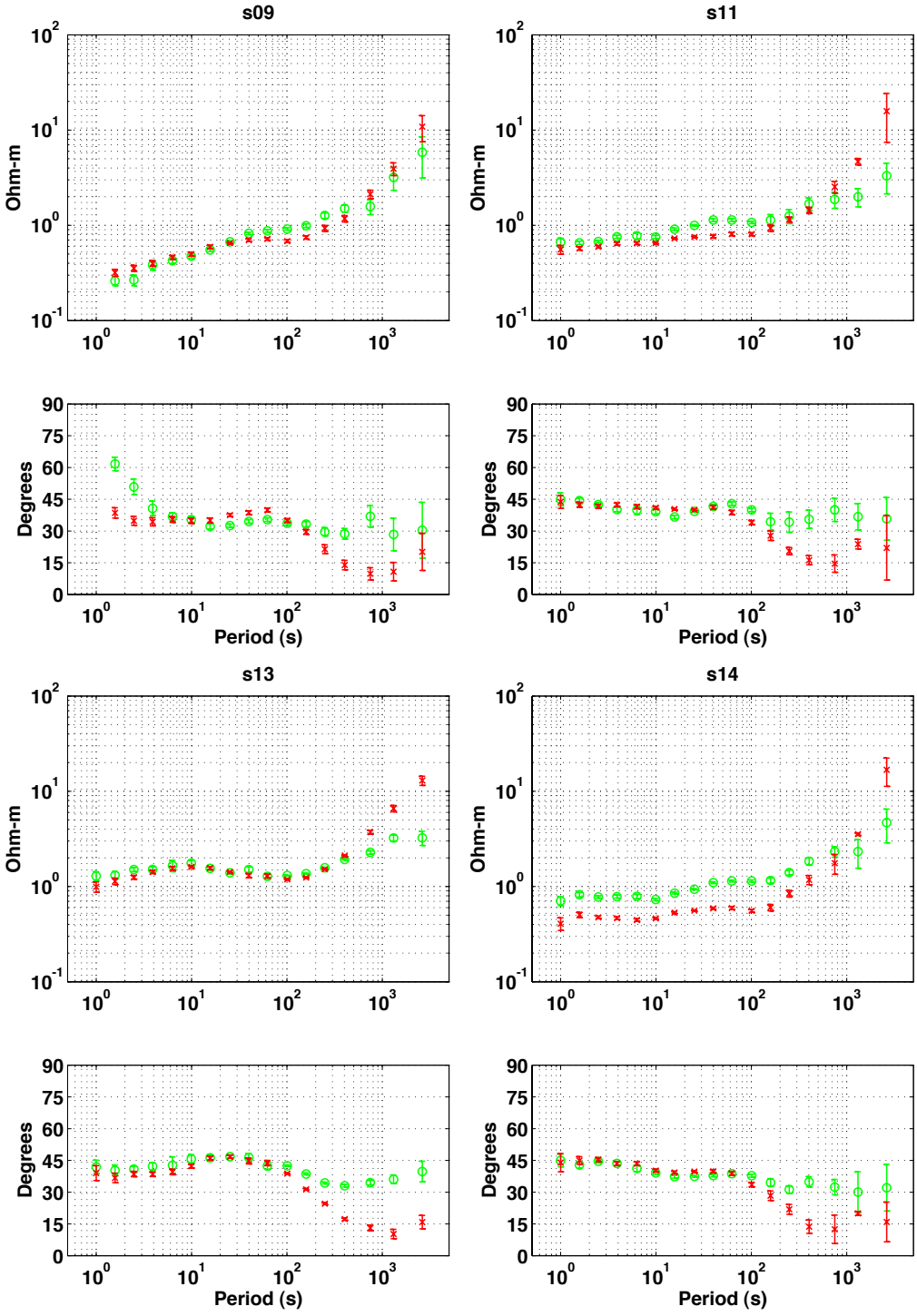

Figure 3.32: Gemini Prospect MT responses for sites s09, s11, s13, and s14. Green symbols correspond to Zxy, where x is oriented at 45° from North, and red symbols are for Zyx.

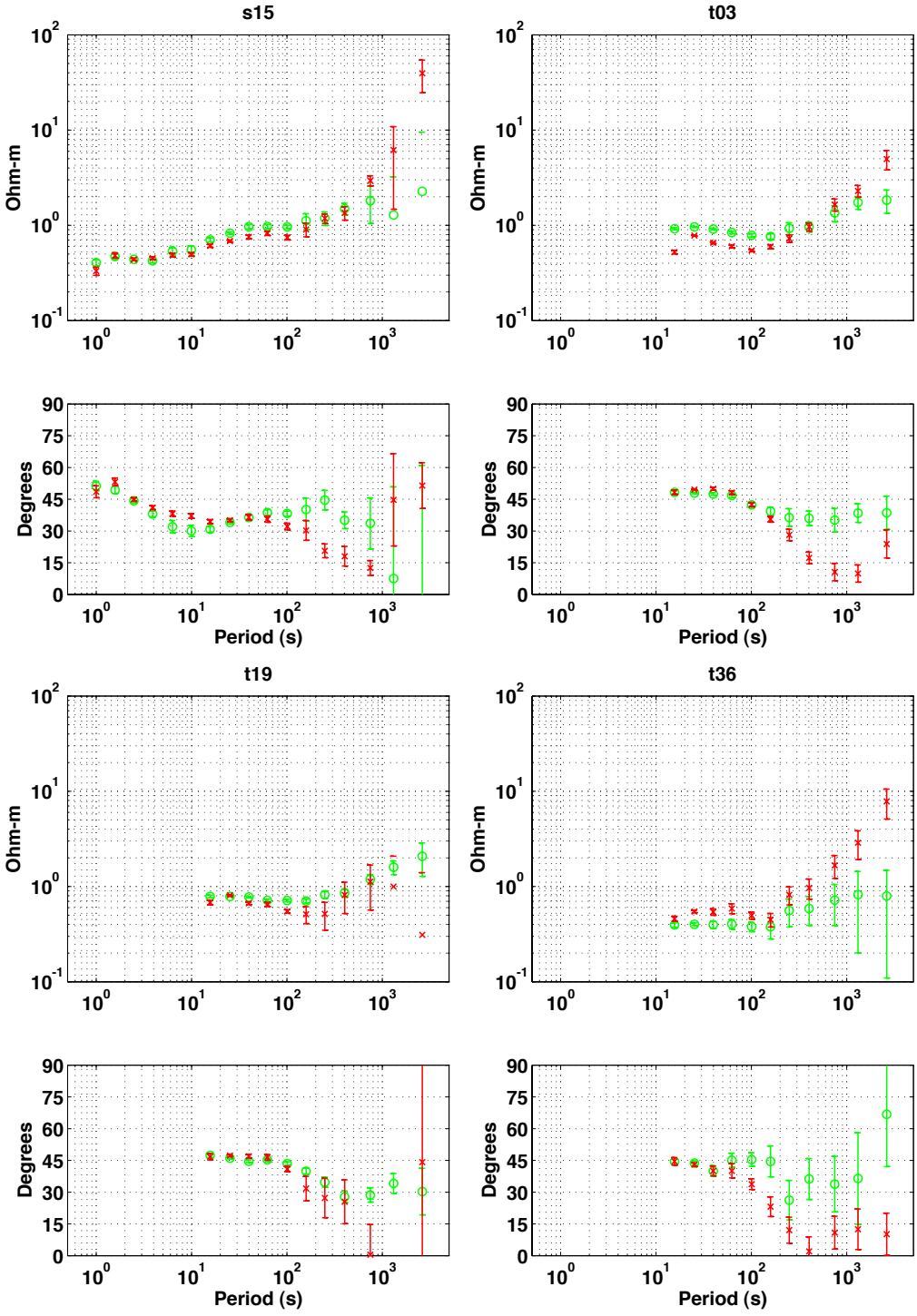

Figure 3.33: Gemini Prospect MT responses for sites s15, t03, t19, and t36. Green symbols correspond to Zxy, where x is oriented at 45° from North, and red symbols are for Zyx.

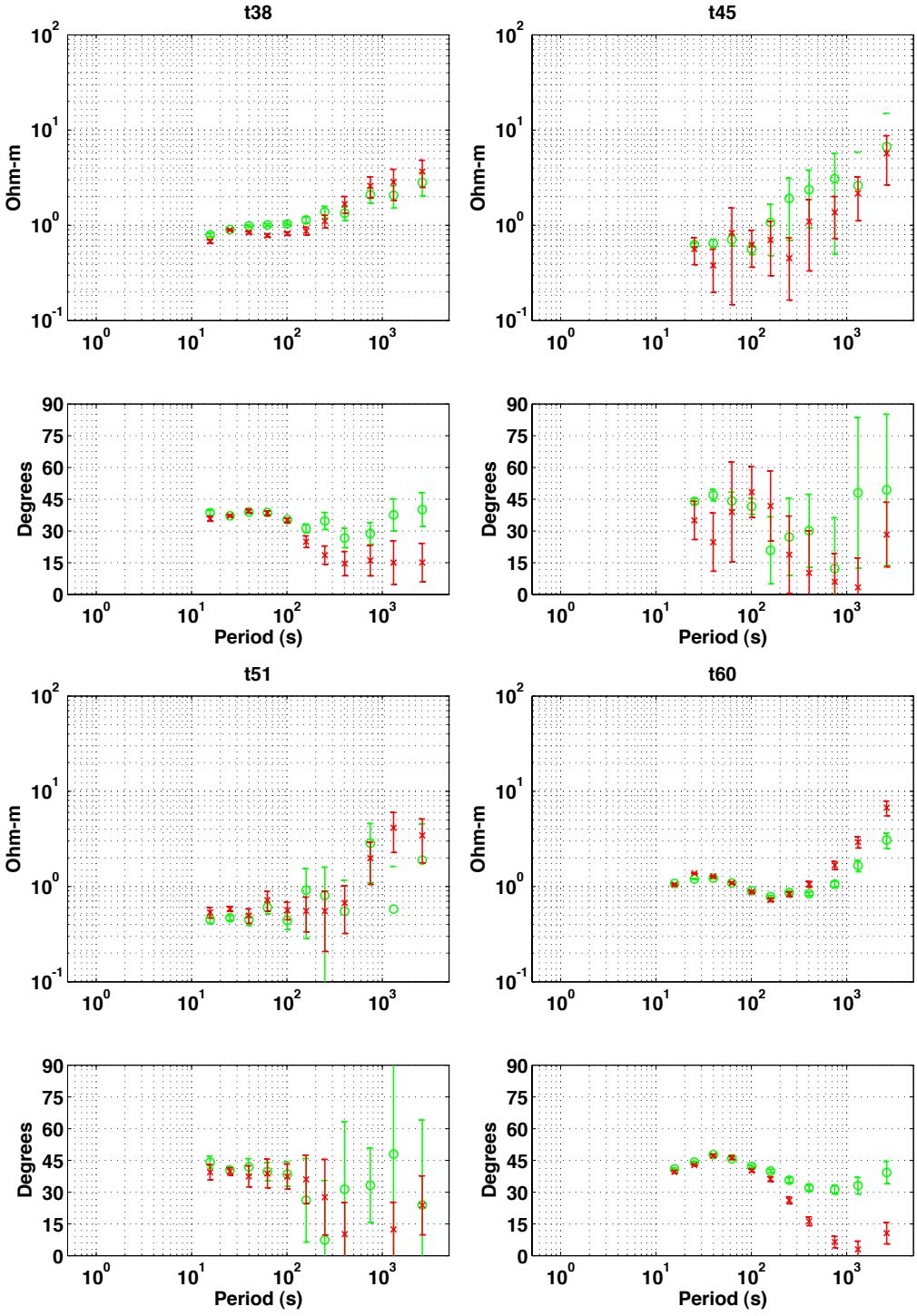

Figure 3.34: Gemini Prospect MT responses for sites t38, t45, t51, and t60. Green symbols correspond to Zxy, where x is oriented at 45° from North, and red symbols are for Zyx.

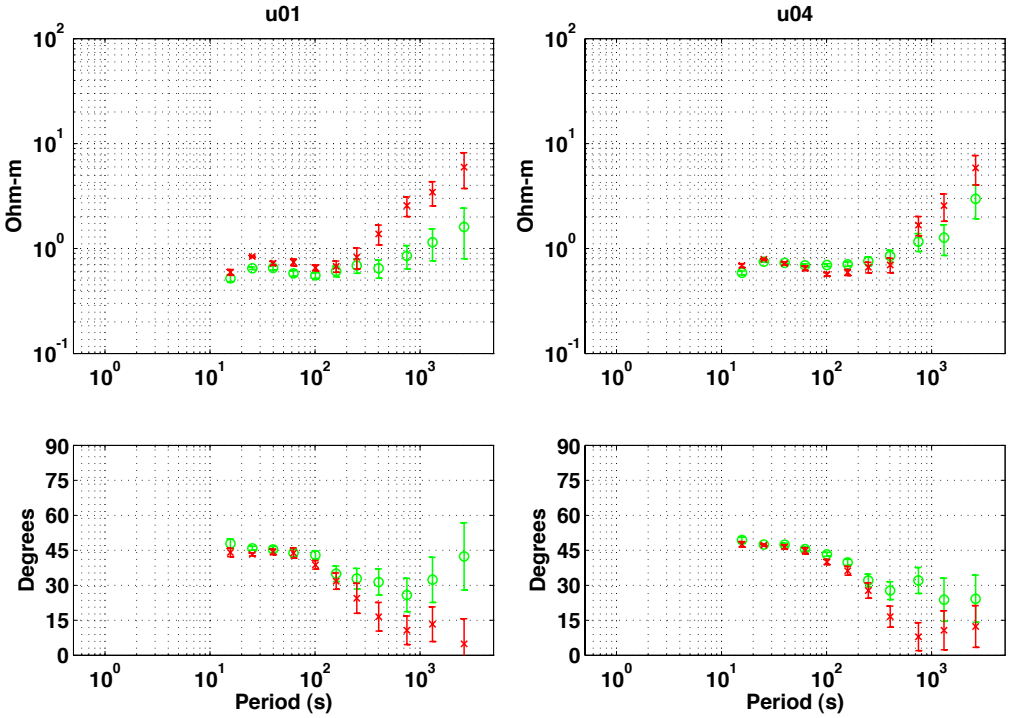

Figure 3.35: Gemini Prospect MT responses for sites u01 and u04. Green symbols correspond to Zxy, where x is oriented at 45° from North, and red symbols are for Zyx.

Chapter 4

Broadband Marine MT Exploration of the East Pacific Rise at 9°50′N

Abstract

We present the first use at a mid-ocean ridge of a recently developed broadband marine magnetotelluric (MT) instrument. The extended high frequency performance of the instrument allows resolution of electrical resistivity structure at shallower depths than traditional marine MT sensors. Our two-dimensional inversion model from data collected at four MT sites on the East Pacific Rise (EPR) at 9°50′N demonstrates the viability of the method to image electrical resistivity structure in both the crust and shallow mantle. While our pilot experiment falls far short of the coverage needed to provide rigorous constraints on structure, a low resistivity zone in the crustal portion of the inversion model agrees well with seismic tomography and seafloor compliance results. Resistivities beneath the ridge imply a crustal partial melt fraction of 1-20%. A total melt volume of about 0.75 km^3 per kilometer of ridge implies an average melt residence time of about 1000 years.

4.1 Introduction

The majority of Earth's crust is formed at mid-ocean ridges and so the mechanisms that generate, transport and emplace melt are important from a global tectonic perspective. Despite the vast number of previous ridge studies, many questions about the extent and distribution of melt in the crust and shallow mantle persist. Additionally, new questions have arisen about the role of hydrothermal circulation in the removal of heat from the crust and in determining the distribution of partial melt [*Dunn and Toomey*, 2001; *Crawford and Webb*, 2002]. While the seismic techniques that have dominated ridge research are well suited to identifying structural boundaries, they have a more difficult time quantifying physical properties; other complementary methods of ridge exploration are needed. One good example is the seafloor compliance method [*Crawford et al.*, 1999; *Crawford and Webb*, 2002] which is sensitive to the shear velocity of both the crust and shallow mantle.

Here we present results from another technique–the broadband marine magnetotelluric (MT) method–which is sensitive to the bulk electrical resistivity in both the crust and mantle. Oceanic lithosphere is typically very resistive. However, the inclusion of even a small amount of connected melt or sea water at spreading ridges can greatly decrease the bulk resistivity, making ridge structures a suitable target for electrical methods. Although MT studies of ridges are far from new [e.g., *Heinson et al.*, 1993], our experiment used instrumentation equipped with broadband sensors capable of measuring shorter period seafloor electric and magnetic fields than before, enabling resolution of structure at crustal depths. Previous ridge MT experiments [*Heinson et al.*, 1993; *Evans et al.*, 1999] were relatively insensitive to crustal resistivity, and thus focused on mapping mantle structure. An experiment that measured broadband magnetic fields at two sites on the Juan de Fuca ridge is presented by *Jegen and Edwards* [1998], but did not include measurement of broadband electric fields. The traditional technique to

image crustal resistivity at ridges has been the controlled-source electromagnetic method [*Evans et al.*, 1991; *MacGregor et al.*, 1998; 2001].

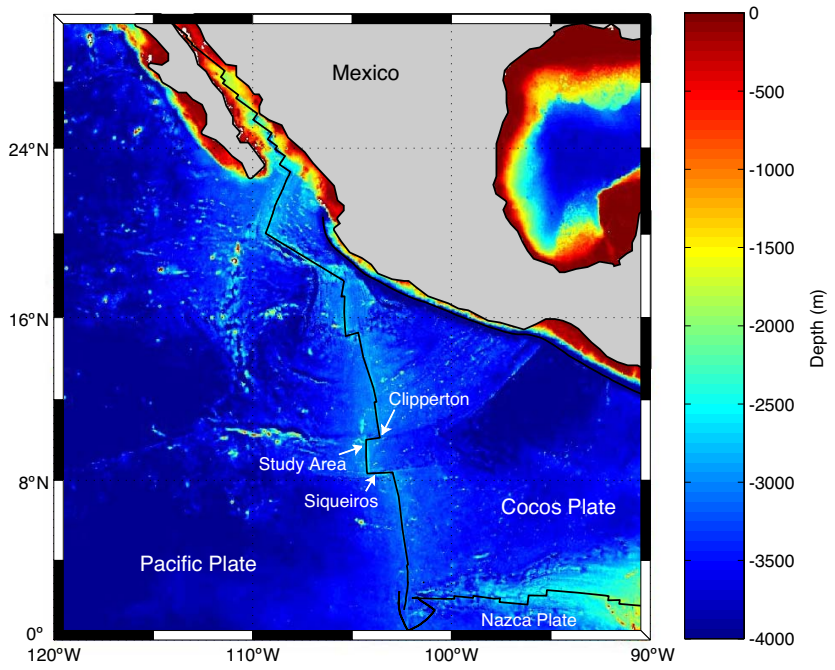

Figure 4.1: Regional map of showing location of the experiment on the East Pacific Rise near 9°50′N, between the Clipperton and Siqueiros transforms.

In February 2000, broadband marine MT instruments were deployed on the East Pacific Rise (EPR) near 9°50′N as part of a magnetometric resistivity (MMR) experiment designed to study the electrical resistivity of the shallow crust in the vicinity of the ridge [*Evans et al.*, 2002]. The MT instruments contained magnetometers suitable for recording the MMR transmissions, but also electric field dipoles, allowing us to carry out the first test of the instrument at a mid-ocean ridge. The instrument was developed for routine use for petroleum exploration on the continental shelves [*Constable et al.*, 1998], and uses AC coupled sensors designed to measure the small seafloor electric and magnetic field variations in the period range of 0.1 to 10,000 seconds. However, for this experiment the shortest measurable period is limited by attenuation in the conductive ocean and is about 18 seconds. Figure 4.1 shows the location of the experiment on the EPR between

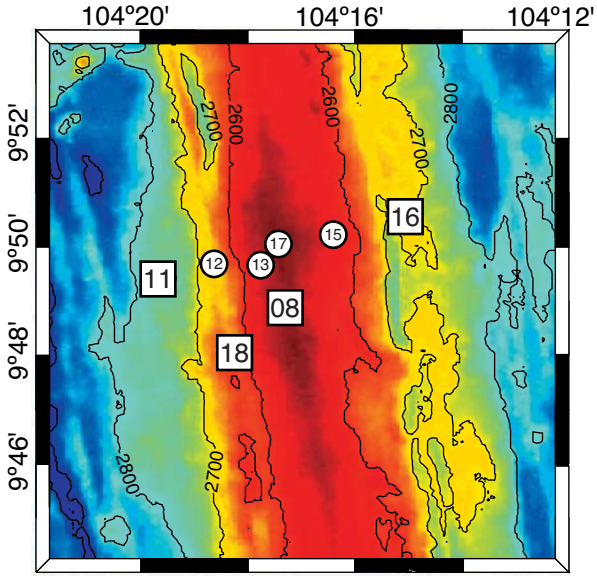

Figure 4.2: Bathymetry map of the experiment location. MT measurement sites are shown as numbered circles and squares. This study used only the sites shown as squares. Seafloor depths are in meters.

the Clipperton and Siqueiros transform faults, near 9°50′N. Figure 4.2 shows the the locations of the MT sites occupied near the ridge axis as well as the local ridge bathymetry.

4.2 Structure of the EPR Near 9°50′N

The fast spreading East Pacific Rise between 9° and 10°N has been one of the most heavily studied ridge sections in the world. Separating the Pacific and Cocos plates, this section of the ridge has a nearly constant strike of about 352° and is bound by the Clipperton transform to the north and the Siqueiros transform to the south (Figure 4.1). The full spreading rate has been nearly constant at about 110 mm/yr for the past 2 My [*Carbotte and Macdonald*, 1992]. A lens of nearly pure melt a few tens of meters thick and about 1 km wide is found continuously beneath the ridge axis at a depth of about 1.5 km beneath the seafloor [*Kent et al.*, 1993]. A low velocity zone in the sheeted-dike complex above the melt lens

is inferred to be a thermal boundary layer separating hydrothermal fluids from the melt lens [*Toomey et al.*, 1994]. Seismic velocity variations in the shallow crust along the ridge crest are inferred to match patterns of hydrothermal circulation [*Tian et al.*, 2000] because there is no significant change in layer 2A thickness [*Harding et al.*, 1993] and the slowest velocities coincide with the region of the 1991 axial summit eruption at 9°50′N [*Haymon et al.*, 1993].

A highly attenuating low velocity region resides beneath the melt lens [*Toomey et al.*, 1990; *Vera et al.*, 1990; *Wilcock et al.*, 1995; *Dunn et al.*, 2000; *Crawford and Webb*, 2002]. Seismic tomography [*Dunn et al.*, 2000] indicates that the low velocity zone is about 5 km wide in the lower crust and triples in width to about 15-20 km in the shallow mantle. Partial melt fractions of the low velocity zone are estimated to be quite low, with peak estimates of less than about 15-20% in the lower crust [*Dunn et al.*, 2000; *Crawford and Webb*, 2002] and less than 5% in the shallow mantle reservoir. Due to the increase in size of the reservoir, the sub-Moho reservoir may account for more than 40% of the magma budget [*Dunn et al.*, 2000].

To explain the increase in width of the low velocity region at the Moho, both the tomography and compliance experiments suggest that deep hydrothermal circulation in the crust acts to convectively cool the flanks of the crustal partial melt region [*Dunn et al.*, 2000; *Crawford and Webb*, 2002]. Seismic anisotropy estimates of up to 4% at 9°30′N are consistent with ridge parallel vertical cracks that extend no deeper than about 2 km depth, and account for less than <10% of the estimated 12% shallow crustal porosity [*Dunn and Toomey*, 2001]. While such cracks provide permeable pathways for hydrothermal circulation, they do not penetrate deep enough to provide the lower crustal circulation suggested by *Dunn et al.* [2000] and *Crawford and Webb* [2002].

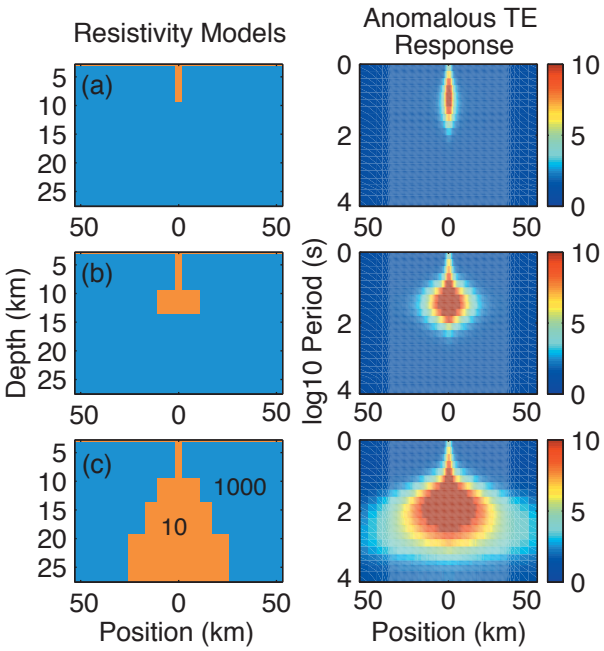

Figure 4.3: Simplistic 2D forward model study of the response generated by possible ridge resistivity structures. The left column shows the 2D resistivity forward models, and the right column shows the anomalous TE mode response generated for each model. See text for a description of the structures included in each model.

4.3 Sensitivity to Ridge Structures

The resolving power of MT is heavily dependent on the frequency band of measurements, the subsurface resistivity structure, and also the density and lateral extent of measurement sites. In Figure 4.3 we present a simplistic two-dimensional (2D) model study illustrating the magnitude, lateral extent and bandwidth of the MT response generated by three possible ridge resistivity structures, shown in the left column. In the right column we plot the ratio of the MT response from a 1D oceanic resistivity profile (from the model sides), and the response of the full 2D models that included the conductive (10 ohm-m) inhomogeneities that represent regions of partial melt.

The simplified crustal partial melt conductor included in model (a) is based on seismic tomography at the EPR 9°30′N [*Dunn et al.*, 2000] and seafloor

compliance at 9-10° N [*Crawford and Webb*, 2002], which both suggest the crust contains a 4-5 km wide region of partial melt extending from about 1.5 km depth to near the base of the crust. The anomalous response indicates that the signal from this structure manifests itself at periods of 1-100 seconds, is up to about a factor of 10 different from the 1D response, and extends to distances just beyond the width of the structure. Model (b) is an extension of model (a), to which has been added a 20 km wide conductive zone in the shallow mantle that represents partial melt accumulating at the base of the crust [*Dunn et al.*, 2000]. The response of this model indicates that a shallow mantle partial melt region will affect data at periods of about 10-300 seconds. Model (c) includes a deeper and broader region of partial melt in the mantle that extends down to 60 km depth and is sensed by data up to about 8000 seconds period. Although the shortest period measured for this experiment is about 18 seconds, this model study suggests that our MT responses should contain a significant amount of information about crustal and upper mantle structure.

4.4 Data and Modeling

This paper analyzes 4 of the 8 MT sites occupied for the experiment. Two of the sites (13 and 15) were tests of a new (then) 24-bit data logger and only recorded electric fields. Site 17 had one malfunctioning magnetometer and only recorded one magnetic field component. Site 12 has high quality data but also has an anomalous magnetic field "static shift" in which the the total measured magnetic field is about 75% smaller than nearby stations across all frequencies, which may be due to a tilt of the instrument on the seafloor. For simplification, only sites 08, 11, 16 and 18 are included in the analysis presented here.

The MT sites recorded data simultaneously during the experiment, which allowed us to form frequency dependent MT impedance estimates by using a robust multivariate approach [*Egbert*, 1997]. Our analysis yielded good MT impedances

at periods of 18 to 6000 seconds period, suitable for detecting both crustal and upper mantle structure. Impedance strike and skew estimates [*Swift*, 1986] show that the impedances are predominantly 2D with low skew values, but also show a frequency dependence in the strike direction. Two main groupings exist in the strike estimates. At periods less than about 100 seconds, the strike directions are nearly aligned with the ridge strike of about -8° from geographic North; this is as expected given bathymetry and ridge structure. At periods greater than about 100 seconds, strike directions cluster around 20° from North. The change in strike direction for the long period data may be caused by a shift in structural strike at depth, the distortion of the long period MT fields by the geomagnetic coast effect, or possibly by anisotropic resistivity of mantle olivine. We mention these possible causes for completeness, but a thorough discussion is beyond the scope of this paper. For the purpose of 2D modeling, we have chosen to maximize the off diagonal impedance components by rotating the data at 100 seconds period and less to the ridge strike of -8° and to 20° for data at periods greater than 100 seconds. 4.4 shows the MT apparent resistivity and phase for each site after rotation. The responses are fairly complicated and show a strong asymmetry between the TE (strike aligned electric field) and TM (strike aligned magnetic field) modes.

As demonstrated for previous ridge MT surveys [e.g., *Heinson et al.*, 1993], much of the structure in MT responses is due to the distortion of the incident MT fields by the rugged seafloor bathymetry. However, ridge bathymetry can be measured (if not already available in sufficient detail), is predominantly 2D on a regional scale (away from transforms and seamounts), and can be included as a priori information in MT modeling. We used a standard 2D MT inversion algorithm [*de Groot-Hedlin and Constable*, 1990] that incorporates a finite element forward modeling code [*Wannamaker et al.*, 1987] capable of using triangular elements to smoothly approximate the 2D seafloor bathymetry. This technique yields realistic MT responses to periods at least as short as 10 seconds.

An inversion fitting the data to an RMS misfit of 1.0 is shown in Fig-

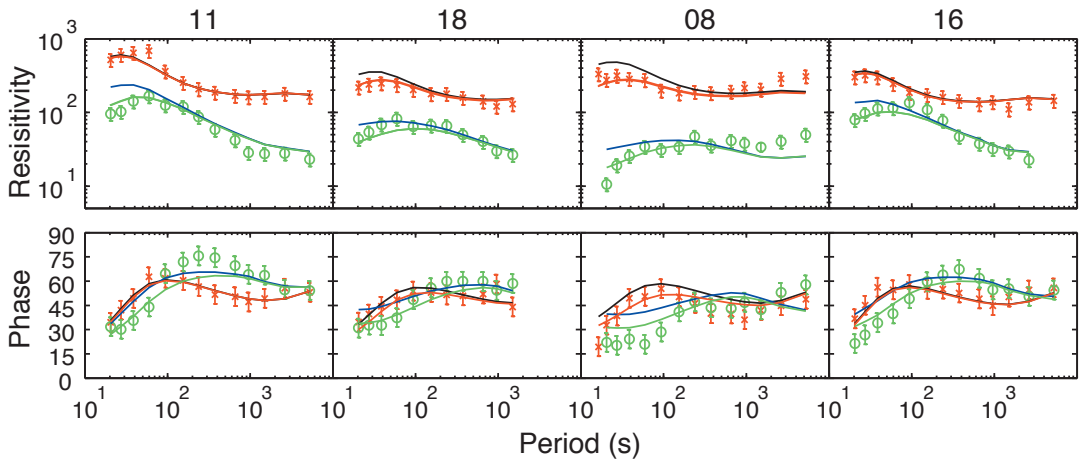

Figure 4.4: MT data and model responses. Apparent resistivity units are ohm-m and the phases are degrees. TE and TM mode data are shown as green and red symbols, respectively. Inversion model responses from Figure 4.5 are shown as green and red lines. Blue and black lines show the TE and TM mode responses for the same model, but with the mid-crustal conductive zone resistivities set to a floor of 100 ohm-m.

ure 4.5. Both TE and TM modes of data were inverted, with a minimum error floor of 20%. The forward response of the model is shown along with the data in Figure 4.4. Although the model was parameterized to estimate 2D resistivity structure as deep as 300 km, and features a highly conductive zone (about 1-10 ohm-m) at depths of 60-120 km beneath the ridge, the limited aperture of MT sites (4 sites all within 5 km of the ridge) does not constrain the position or extent of deep structure extending outside the width of the array. Therefore, we have chosen to focus our analysis on the crustal and shallow mantle portion of the model. Inversion using only the data at periods less than 200 seconds yields a model with similar crustal and shallow mantle structures to Figure 4.5.

4.5 Discussion and Conclusions

The inverted model shows a significant amount of structure in both the crust and shallow mantle. The left and right sides of the model show a predom-

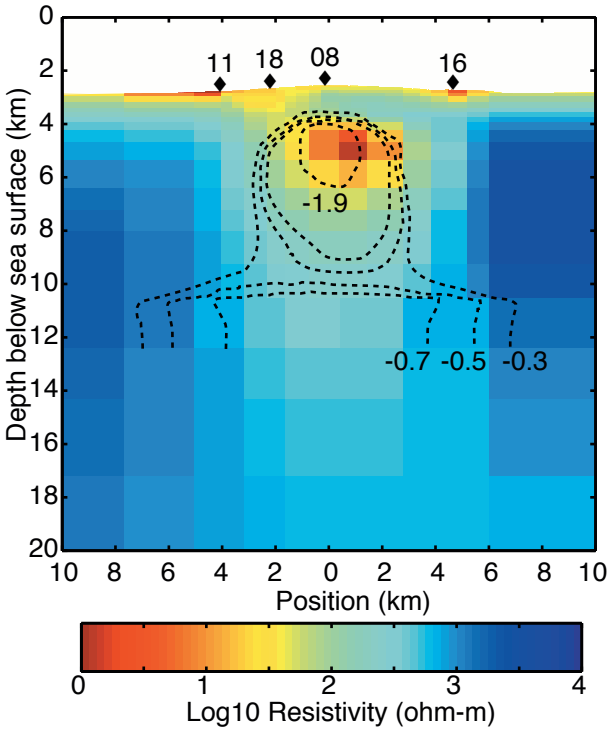

Figure 4.5: Inversion model fitting the data to an RMS misfit of 1.0. MT sites are shown as black diamonds. Seismic velocity perturbation contours for ΔV_p = -1.9, -0.7, -0.5 and -0.3 km/s from *Dunn et al.* [2000] are shown for comparison.

inantly 1D layered structure with resistivities of about 10-100 ohm-m to depths of about 1 km beneath the seafloor, increasing rapidly to about 10,000 ohm-m at greater depths. While this structure is outside the array of sites and is not well constrained, it does agree with controlled-source electromagnetic soundings on 40 Ma normal oceanic lithosphere in the north-east Pacific [*Constable and Cox*, 1996], and suggests that the transition from low resistivities dominated by the magmatic system at the ridge axis to the dry and cold resistive lithosphere away from the axis starts occurring within a distance of about 6-10 km.

Our shallow (<1 km) resistivities are generally consistent with controlled-source soundings at the EPR near 13°N [*Evans et al.*, 1991], where a steep resistivity gradient was shown to exist as resistivity increases from about 1 ohm-m to 100 ohm-m in the first kilometer, both at the ridge axis and on 100,000 year

old crust (about 5 km off axis). MMR results [*Evans et al.*, 2002] agree with our off-axis resistivities, but are more conductive on-axis. The on-axis disagreement is probably due to a lack of shallow resolution and the relatively wide MT site spacing.

The mid-crustal conductive zone, which extends to about 3 km on both sides of the ridge axis at depths of about 1.5 to 6 km below the seafloor, has resistivities of about 1-100 ohm-m and coincides with the low P wave velocity region detected at 9°30′N using seismic tomography [*Dunn et al.*, 2000] and the low shear velocity region detected at 9°48′N using seafloor compliance [*Crawford and Webb*, 2002]. To demonstrate that the MT responses are sensitive to this feature, we have computed the response of the inversion model with the mid-crustal conductive zone resistivities set to a floor of 100 ohm-m. The RMS misfit increases to 1.4 and the response, shown as blue and black lines in Figure 4.4, is significantly different at all sites for periods less than about 100 seconds, especially for the TE mode. The difference in misfit suggests that the conductive region is required by our data. For comparison, in Figure 4.5 we have included four seismic velocity perturbation contours from the tomography experiment, which show a relatively narrow low velocity region in the crust with the largest velocity perturbations residing at depths of about 1.5 to 3 km beneath the seafloor, in agreement with the lowest resistivities shown in our model. Assuming this region contains well connected partial melt in a thin film geometry, we can use standard mixing laws [*Schmeling*, 1986] to estimate about 1-20% partial melt, in agreement with both the compliance and tomography results. A 100 m thick melt lens that caps the partial melt region [e.g., *Kent et al.*, 1993] is too thin to be resolved by the MT data, but does contribute to the overall low bulk resistivity in this region. While the tomography and compliance results indicate that melt accumulates in a broader region at the base of the crust (below about 6-7 km beneath the seafloor), the resistivity model shows a zone of lower resistivities–about 100-500 ohm-m and 10 km wide–that extends from the crust to the shallow mantle with no significant

change in width. However, the limited number of sites and small aperture of our experiment do not allow sufficient lateral resolution to distinguish between such features at these depths.

To explain the change in width of the low velocity region, both the tomography and compliance experiments suggest that deep hydrothermal circulation in the crust acts to convectively cool the flanks of the crustal partial melt region. Such deep hydrothermal circulation would dominate the bulk resistivity of the crustal rocks and result in resistivities much lower than 1000-10,000 ohm-m on the flanks of the partial melt region. If this is indeed occurring, then our model suggests it is limited to the region about 3-6 km either side of the ridge axis, although the details of the transition zone shown in our model may well be influenced by the smoothness constraints in the inversion.

While the structural similarity of our inversion with that obtained using seismic tomography is exceptional, especially considering the small number of sites in the MT experiment, our results are obviously limited by the lateral coverage. However, the ability to estimate the electrical resistivity and partial melt fraction allows us to estimate about 0.75 km^3 of crustal melt per kilometer of ridge. Using the ridge spreading rate of 110 km per My and assuming the 7 km thick crust is formed by a steady state solidification of crustal melt, we can predict an average melt residence time of about 1000 years.

Acknowledgments

We are grateful to Rob Evans and Spahr Webb for the opportunity to test the new MT instrument during their MMR experiment. We also thank: Lisl Lewis for assisting during the instrument deployments and recoveries, Jacques Lemire for helping design and build the MT instruments, the captain and crew of the R/V Melville for their assistance during the cruise, and Gary Egbert and Phil Wannamaker for making their MT computer codes freely available.

The text of this chapter, in part or in full, is a reprint of the material as it appears in Key, K. and S. Constable, Broadband marine MT exploration of the East Pacific Rise at 9°50′N, *Geophys. Res. Letts., 29*, 2054, doi: 10.1029/2002GL016035, 2002. The dissertation author was the primary researcher and author of the published work. The co-author listed in the publication directed and supervised the research which forms the basis for this chapter.

References

Carbotte, S., and K. Macdonald, East Pacific Rise 8°-10°30′N: Evolution of ridge segments and discontinuities from SeaMARC II and three-dimensional magnetic studies, *J. Geophys. Res.*, *97*, 6959–6982, 1992.

Constable, S., and C. S. Cox, Marine controlled-source electromagnetic sounding, 2. The PEGASUS experiment, *J. Geophys. Res.*, *101*, 5519–5530, 1996.

Constable, S. C., A. S. Orange, G. M. Hoversten, and H. F. Morrison, Marine magnetotellurics for petroleum exploration Part I: A sea-floor equipment system, *Geophysics*, *63*, 816–825, 1998.

Crawford, W. C., and S. C. Webb, Variations in the distribution of magma in the lower crust and at the Moho beneath the East Pacific Rise at 9°-10°N, *Earth Planet. Sci. Lett.*, *203*, 117–130, 2002.

Crawford, W. C., S. C. Webb, and J. A. Hildebrand, Constraints on melt in the lower crustal and Moho at the East Pacific Rise, 9°48′N, using seafloor compliance measurements, *J. Geophys. Res.*, *104*, 2923–2939, 1999.

de Groot-Hedlin, C., and S. Constable, Occam's inversion to generate smooth two-dimensional models from magnetotelluric data, *Geophysics*, *55*, 1613–1624, 1990.

Dunn, R. A., and D. R. Toomey, Crack-induced seismic anisotropy in the oceanic crust across the East Pacific Rise (9°30′N), *Earth Planet. Sci. Lett.*, *189*, 9–17, 2001.

Dunn, R. A., D. R. Toomey, and S. C. Solomon, Three-dimensional seismic structure and physical properties of the crust and shallow mantle beneath the East Pacific Rise at 9°30′N, *J. Geophys. Res.*, *105*, 23,537–23,555, 2000.

Evans, R. L., S. C. Constable, M. C. Sinha, C. S. Cox, and M. J. Unsworth, Upper crustal resistivity structure of the East Pacific Rise near 13° N, *Geophys. Res. Lett.*, *18*, 1917–1920, 1991.

Evans, R. L., S. C. Webb, W. Crawford, C. Golden, K. Key, L. Lewis, H. Miyano, E. Roosen, and D. Doherty, Crustal resistivity structure at 9°50′N on the East Pacific Rise; results of an electromagnetic survey, *Geophys. Res. Lett.*, *29*, 6–1 to 6–4, 2002.

Evans, R. L., et al., Asymmetric electrical strucure in the mantle beneath the East Pacific Rise at 17°S, *Science*, *286*, 752–756, 1999.

Harding, A. J., G. M. Kent, and J. A. Orcutt, A multichannel seismic investigation of upper crustal structure at 9n on the east pacific rise: Implications for crustal accretion, *J. Geophys. Res.*, *98*, 13,925–13,944, 1993.

Haymon, R. M., et al., Volcanic eruption of the mid-ocean ridge along the East Pacific Rise crest at 9°45 − 52′N: direct submersible observations of seafloor phenomena associated with an eruption event in April 1991, *Earth Planet. Sci. Lett.*, *119*, 85–101, 1993.

Heinson, G. S., A. White, L. K. Law, Y. Hamano, H. Utada, T. Yukutake, J. Segawa, and H. Toh, EMRIDGE: The electromagnetic investigation of the Juan de Fuca Ridge, *Marine Geophys. Res.*, *15*, 77–100, 1993.

Jegen, M., and R. N. Edwards, The electrical properties of a 2D conductive zone under the Juan de Fuca ridge, *Geophys. Res. Lett.*, *25*, 3647–3650, 1998.

Kent, G. M., A. J. Harding, and J. A. Orcutt, Distribution of magma beneath the East Pacific Rise between the Clipperton Transform and the 9°17′N deval from forward modeling of common depth point data, *J. Geophys. Res.*, *98*, 13,945–13,969, 1993.

MacGregor, L. M., S. Constable, and M. C. Sinha, The RAMESSES experiment III: Controlled-source electromagnetic sounding of the Reykjanes Ridge at 57°45′N, *Geophys. J. Int.*, *135*, 773–789, 1998.

MacGregor, L. M., M. Sinha, and S. Constable, Electrical resistivity structure of the Valu Fa Ridge, Lau Basin, from marine controlled-source electromagnetic sounding, *Geophys. J. Int.*, *146*, 2001.

Schmeling, H., Numerical models on the influence of partial melt on elastic, anelastic and electrical properties of rocks. Part II: electrical conductivity, *Phys. Earth Planet. Inter.*, *43*, 123–136, 1986.

Swift, C. M. J., A magnetotelluric investigation of an electrical conductivity anomaly in the southwestern United States, in *Magnetotelluric methods*, edited by K. Vozoff, pp. 156–166, Soc. Expl. Geophys., 1986, not previously published.

Tian, T., W. S. D. Wilcock, D. R. Toomey, and R. S. Detrick, Seismic heterogeneity in the upper crust near the 1991 eruption site on the East Pacific Rise, 9°50′N, *Geophys. Res. Lett.*, *27*, 2369–2372, 2000.

Toomey, D. R., G. M. Purdy, S. C. Solomon, and W. S. D. Wilcock, The three-dimensional seismic velocity structure of the East Pacific Rise near latitude 9°30′N, *Nature*, *347*, 639–645, 1990.

Toomey, D. R., S. C. Solomon, and G. M. Purdy, Tomographic imaging of the shallow crustal structure of the East Pacific Rise at 9°30′N, *J. Geophys. Res.*, *99*, 24,135–24,157, 1994.

Vera, E. E., J. C. Mutter, P. Buhl, J. A. Orcutt, A. J. Harding, M. E. Kappus, R. S. Detrick, and T. Brocher, The structure of 0- to 0.2-m.y. old oceanic crust at 9°N on the East Pacific Rise from expanded spread profiles, *J. Geophys. Res.*, *95*, 15,529–15,556, 1990.

Wannamaker, P. E., J. A. Stodt, and L. Rijo, A stable finite-element solution for two-dimensional magnetotelluric modeling, *Geophys. J. R. astr. Soc.*, *88*, 277–296, 1987.

Wilcock, W. S. D., S. C. Solomon, and D. R. Toomey, Seismic attenuation structure of the East Pacific Rise near 9°30′N, *J. Geophys. Res.*, *100*, 24,147–24,165, 1995.